ABSTRACT


Title of Dissertation:     CONTROL AND TRANSPORT OF INTENSE
                           ELECTRON BEAMS

                           Hui Li, Doctor of Philosophy, 2004

Dissertation Directed By:  Professor, Patrick G. O'Shea
                           Department of Electrical and Computer
                           Engineering

The transport of intense beams for advanced accelerator applications with high-intensity beams such as heavy-ion inertial fusion, spallation neutron sources, and intense light sources requires tight control of beam characteristics over long distances. The University of Maryland Electron Ring (UMER), which uses low energy, high current electron beams to model the transport physics of intense space-charge-dominated beams, employs real-time beam characterization and control in order to optimize beam quality throughout the strong focusing lattice. We describe in this dissertation the main beam control techniques used in UMER, which include optimal beam steering by quadrupole scans, beam rotation correction using a skew corrector, rms envelope matching and optimization, empirical envelope matching, beam injection, and phase space reconstruction using a tomographic method. Using these control techniques, we achieved the design goals for UMER. The procedure is not only indispensable for optimum beam transport over long distances, but also provides important insights into the beam physics involved.

CONTROL AND TRANSPORT OF INTENSE ELECTRON BEAMS


By


Hui Li



Thesis or Dissertation submitted to the Faculty of the Graduate School of the
University of Maryland, College Park, in partial fulfillment
of the requirements for the degree of
Doctor of Philosophy
2004

Advisory Committee:
Professor Patrick G. O'Shea, Chair/Advisor
Professor Martin Reiser
Professor Richard F. Ellis
Professor Victor L. Granatstein
Professor William S. Levine
Dr. Rami A. Kishek

# Dedication

To Cindy Fang and my parents

# Acknowledgements

I am deeply indebted to many people who helped me during the years of study and research.

My advisor, Professor Patrick O'Shea, gave me invaluable instructions, continuous encouragements throughout the course of my research, and moreover, provided a positive environment, which allowed me to finish my work smoothly. Professor Martin Reiser is my respected authority in our field. I have always benefited from his professional guidance and motivations. Dr. R.A. Kishek and Dr. S. Bernal gave constructive criticism and suggestions to this dissertation. I benefited greatly from their support in my theoretical and experimental work. B. Quinn, Dr. I. Haber, Dr. Y. Zou, Dr. T. Godlove, Dr. M. Walter also contributed to this dissertation in different ways. Thanks to Y. Cui, M. Virgo, J. Neumann, J. Harris, Y. Huo.

Thanks to Prof. Ellis, Prof. Granatstein, and Prof. Levine for serving on my defense committee.

Thanks to my parents and my wife who are the source of my strength and happiness.

# Table of Contents

# List of Tables

# List of Figures

# Chapter 1 Introduction

Beam control is a key issue in achieving optimum beam transport and designing reproducible physics experiments for advanced accelerator research. We emphasize here the most important control techniques developed for the University of Maryland Electron Ring (UMER) project [1, 2]. They include diagnostics, characterization and manipulation of essential beam behaviors, especially the first and second order moments of particle spatial distributions such as beam centroid, rms radius, and rotation angle. Rigorous control of these parameters is necessary for facilitating the intense beam transport experiment in UMER. Other detailed information such as phase space distributions can also be determined by combining knowledge of beam diagnostics and control, tomographic imaging, and simulations. The main topics presented in this dissertation are: (1) beam steering; (2) beam rotation correction; (3) beam matching; (4) beam injection; (5) beam phase space reconstruction.

## 1.1 Beam Physics Background

The transport of intense charged-particle beams is of great interest to many applications such as heavy-ion fusion drivers [3], spallation neutron sources [4], and free electron lasers [5]. All these applications demand tight control of beam characteristics and require maintaining beam quality over long distances. In order to develop efficient and reliable control procedures, we must understand the basic physics issues arising from the interplay of self-fields (space-charge forces) and

external focusing, especially relevant for intense beams. The effects may have a significant impact on beam control, e.g. beam steering, skew correction, matching, and emittance measurement.

It is well known that the *X, Y* beam envelope evolution in the rms sense is governed by the coupled rms envelope equations [6], which have the same form as the Kapchinsky-Vladimirsky (K-V) envelope equations [7]. Though the differential equations can be easily solved numerically, the scaling with the physics parameters is usually obscured by the numerical procedures. To understand fundamental beam physics, we can use the "smooth approximation" [8] for the matched beam in a uniform focusing channel. The coupled rms envelope equations, therefore, can be reduced to a single equation with a constant beam radius $\overline{X} = \overline{Y} = a$, i.e.

$$k_0^2 a - \frac{K}{a} - \frac{\varepsilon^2}{a^3} = 0, \tag{1.1a}$$

or in another form,

$$k^2 a - \frac{\varepsilon^2}{a^3} = 0, \tag{1.1b}$$

where $k_0 = 2\pi / \lambda_0$ is the betatron wave-number without space charge and $\lambda_0$ is the betatron wavelength; $k = k_0 (1 - K / k_0^2 a^2)^{1/2} = 2\pi / \lambda$ is the betatron wave-number with space charge; $K = (I / I_0) \cdot (2 / \beta^3 \gamma^3)$ is the generalized dimensionless perveance with the characteristic current $I_0 = 4\pi\varepsilon_0 mc^3 / q \approx 17$ kA for electrons [9]; $\varepsilon$ is the effective (4×rms, unnormalized) emittance. The quantity $k_0^2 a$ represents the average external focusing force that balances the space-charge and the emittance forces

combined. The ratio of space-charge force to external focusing force can be expressed

by the dimensionless intensity parameter [10]

$$\chi = \frac{K}{k_0^2 a^2},$$
(1.2a)

or in an alternative form derived by substituting the analytic result [11] for $a$

$$\chi = \frac{2}{1 + \sqrt{1 + 4(k_0 \varepsilon / K)^2}}.$$
(1.2b)

The definition in Equation 1.2(b) clearly shows that the intensity parameter ranges

from 0 to 1, which depends only on the ratio $k_0 \varepsilon / K$. If $0.5 < \chi < 1$, the beam is

space-charge-dominated. If, on the other hand, $0 < \chi < 0.5$, the beam is in the

emittance-dominated regime. In terms of $\chi$, the betatron tune depression is given by

[10] $k / k_0 = \sigma / \sigma_0 = (1 - \chi)^{1/2}$.

With the use of the intensity parameter, therefore, existing machines with

different energies, configurations and applications can be compared on the same

scale: $0 < \chi < 1$. For instance, most existing high-energy rings normally operate with

$\chi < 0.3$; heavy-ion fusion drivers, on the other hand, require $0.89 < \chi < 0.98$. The

University Maryland Electron Ring (UMER) [1, 2], currently nearing completion,

however, can explore a much wider regime with $\chi$ ranging from 0.2 to 0.98 by

varying the electron beam energy and current. The motivation of this dissertation

hence is to use the flexible features of UMER to study and implement a number of

control techniques for the transport of intense beams. For example, we typically

choose two relatively low-intensity beams with the intensity parameters, 0.32 and

0.78, to establish a baseline for other high-intensity beams. For the correction of beam

rotations, however, we normally use very intense beams with $\chi$ equal to 0.90 and 0.98, since these beams are observed to be more sensitive to the quadrupole skew errors. To sum up, the UMER facility allow us to investigate, in a realistic setting, many beam control issues and related beam physics over a range of intensities never explored before. The general features, beam optics and diagnostics of UMER will be introduced in the next section.

## 1.2 UMER Parameters, Magnets and Diagnostics

UMER is designed as a tool to study the behavior of intense, space-charge-dominated beams on a scaled basis. By using a low-energy (10 keV), high-current (up to 100 mA) electron beam in a compact ring of circumference 11.52 m, UMER represents a low-cost laboratory facility for scaled experiments, computer-code development and validation, and testing of theoretical models. We summarize the normal lattice and main beam parameters of UMER in Table 1.1. For achieving beams with different intensity parameters, we can vary the beam current (and emittance) by using collimating apertures. Several typical beams with different currents and emittances are shown in Table 1.2, which covers a wide intensity range from $\chi = 0.32$ to $\chi = 0.98$ when UMER operates at 10 keV and $\sigma_0 = 76^\circ$. These beams have served as the main objects for experiments and simulations throughout this dissertation.

Table 1.1: UMER lattice and main beam parameters

| | |
|---|---|
| Electron beam energy | 10 keV |
| Main beam current | 100 mA |
| Main beam emittance (4×rms, unnormalized) | 60 mm·mrad |
| Pulse length | 100 ns |
| FODO period | 32 cm |
| Circumference | 11.52 m (36 FODOs) |
| Zero-current phase advance per FODO ($\sigma_0$) | 76$^o$ |
| Betatron tune depression | > 0.16 |

Table 1.2: UMER beam parameters at 10 keV and $\sigma_0 = 76^o$

| $I$ (mA) | $\varepsilon$ (mm·mr) | $a_0$ (mm) | $a$ (mm) | $\chi$ | $\sigma/\sigma_0$ |
|---|---|---|---|---|---|
| 100 | 60 | 3.2 | 9.5 | 0.98 | 0.16 |
| 24 | 30 | 1.5 | 4.8 | 0.90 | 0.31 |
| 7 | 15 | 0.875 | 2.8 | 0.78 | 0.47 |
| 0.6 | 5.5 | 0.25 | 1.3 | 0.32 | 0.82 |

($a_0$ : beam size at the aperture plate; $a$ : average matched beam size in the ring; $\varepsilon$ : 4×rms, unnormalized emittance;)

At present stage, UMER is still under construction (see Fig. 1.1), so our experiments are confined to a 10-meter transport distance that only includes the injector line and the first 24 FODO sections (240$^o$). Though it is a relatively short transport distance, a wealth of new phenomena [12, 13] has came into sight, which offers a unique opportunity for developing various beam control techniques for the transport of intense beams. For example, severe beam rotations for highly space-charge-dominated beams were observed in the UMER ring lattice. We therefore developed a controlled experiment [14] that not only can reduce the existing beam rotations, but also allow us to deliberately introduce rotation errors to study some

important physics issues, e.g. halo formation [13], *x-y* energy transfer, coupling, and emittance growth. The details of the rotation correction scheme will be covered in Chapter 2. In addition, the single-turn transport allows us to measure beam density distributions (by means of a phosphor screen) in every diagnostic chamber as functions of upstream quadrupole strengths, thus making viable the study of the phase space distribution evolution. The relevant topic will be discussed in Chapter 6.
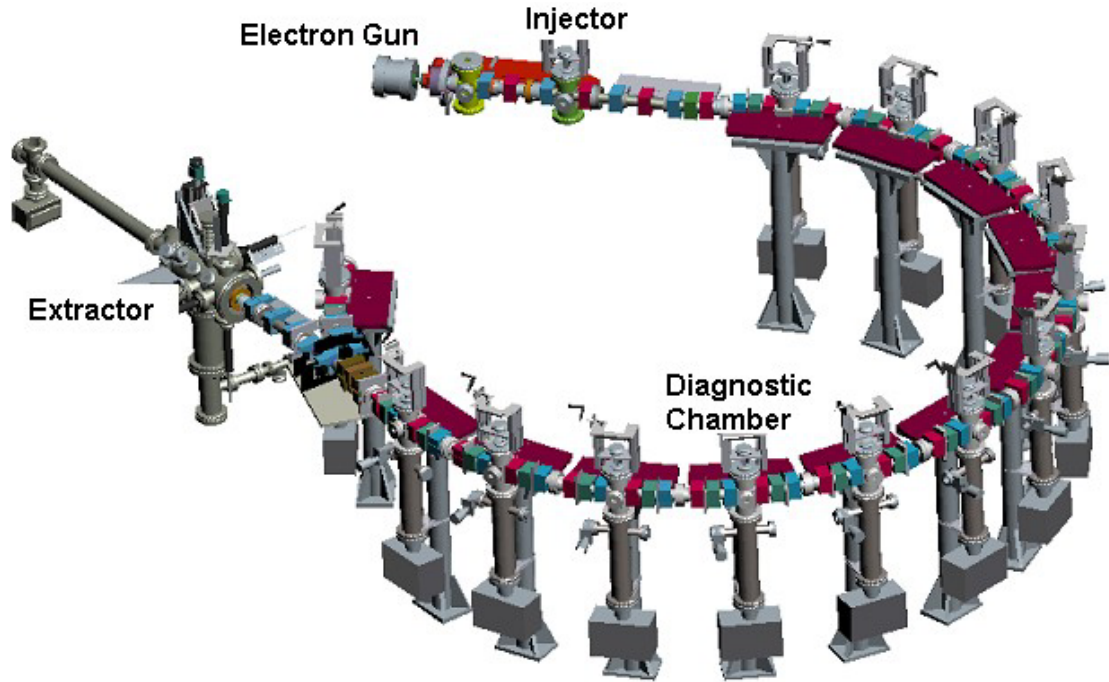


Figure 1.1: Current UMER layout: 2/3 ring + injector + temporary extractor.

The main focusing lattice of UMER is composed of 36 FODO periods, each of which consists of two printed-circuit (PC) quadrupoles for focusing and a PC dipole [15, 16] for 10 deg. bending, with a period length of only 32 cm. The stringent

space requirement dictates the need for short PC quadrupoles and dipoles that follow the design of Lambertson magnets [17, 18]. Figure 1.2 shows the layout of a ring FODO and the wire patterns of a PC quadrupole and a PC dipole. These PC magnets have been characterized with a Rawson-Lush rotating coil [19] of special design. We will give a brief introduction about the rotating coil measurements in Chapter 3. A complete description of PC magnets and the measurements is beyond the scope of this dissertation. One can refer to previous work [15, 16] for details. For control purposes, the PC magnets offer great flexibility in the field strength adjustment. The normal current and power consumption of a PC quadrupole is only about 1.88A and 12W, respectively, for $\sigma_0 = 76^{\circ}$. A standard power supply can therefore easily drive several PC quadrupoles in series. Also, using a specially designed switch, we can easily take any quadrupole off line, which is important for quad current scans. On the contrary, setting up quad-scans in big accelerators is usually a complicated process due to the large magnet power involved. In addition, independent quad control in big machines is normally accomplished by means of an electronic shunt, so the quad current can only be reduced. In our case, not only can the quadrupole current be varied up to 3.5A (focal length $\approx$ 6.4cm), but also the quadrupole polarity can be reversed. Therefore, quad-scan is a convenient and powerful tool in UMER for all types of beam control: steering (Chap. 2), skew correction (Chap. 3), empirical matching (Chap. 4), and phase space tomography (Chap. 6).
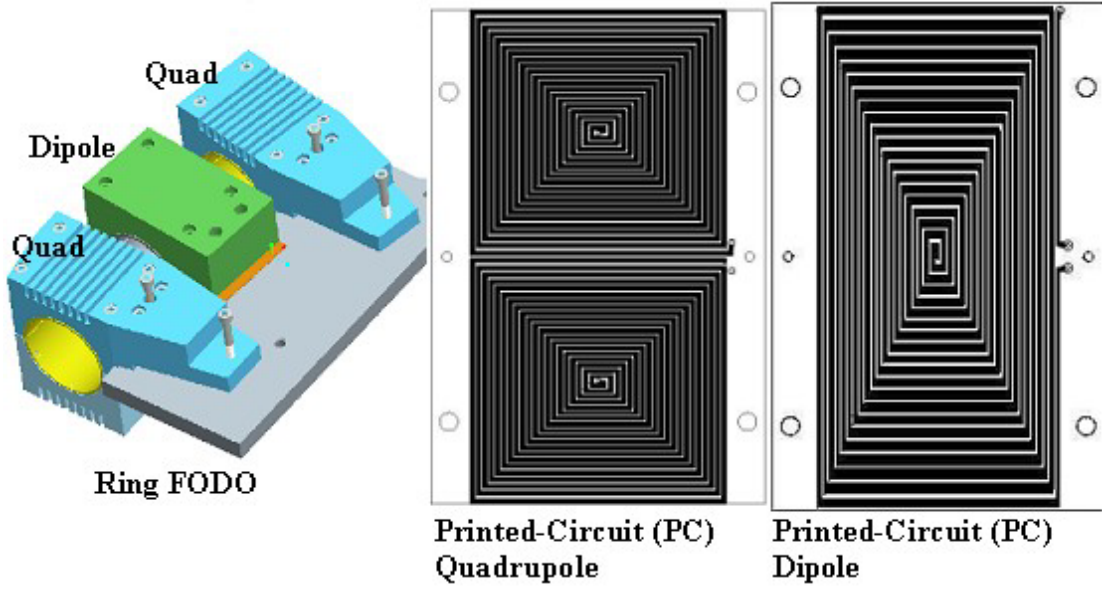
Figure 1.2: Ring FODO layout and wire patterns of a PC quadrupole and a PC dipole.

The dipole magnets in UMER are also based on printed-circuits, so they can be as easily adjusted as the PC quadrupoles. There are two major types of dipoles in UMER: main dipoles for 10 deg. bending and steering dipoles for small angle corrections. Ideally, a main dipole needs 2.95A (<20W) to bend the beam in the horizontal plane by 10 deg. However, the deflection from the Earth's magnetic field cannot be neglected for the low energy electron beams in UMER. UMER therefore is designed to circulate the beam in a "right" direction so the vertical component of the Earth's magnetic field can assist bending. This can introduce an additional 2 deg. deflection on average, so the main dipole currents are reduced to around 2.4A. In addition, since the actual Earth's field varies along the ring's reference trajectory, each ring dipole must be individually adjusted to compensate. We will describe the process to determine the optimal currents of ring dipoles in Chap. 2. Similar to the

8

ring dipoles, each steering dipole is powered with a different current source, and additionally, is configured with an "electronic" polarity switch for bi-polar control. The implementation of this hardware is crucial for real-time and optimal steering via automatic computer control.

The main beam diagnostics are phosphor screens and beam position monitors (BPMs) [20, 21], housed in all diagnostic chambers. Figure 1.3 illustrates the diagram of a diagnostic chamber, where a phosphor screen is placed under a BPM. While the BPMs are intended to obtain beam centroid position for multi-turn operation, phosphor screens at present stage provide more reliable and accurate information not only for steering but also for matching, skew correction, and phase space measurement. We therefore rely on phosphor screen diagnostics for almost all control issues in this dissertation. In the experiment, we can raise up a phosphor screen to the beam line by means of an actuator. The beam image is reflected via a mirror oriented at $45^{\circ}$ to the screen and can be captured through a window by a CCD camera outside the chamber. The camera is an analog black/white video camera. The analog/digital conversion is done with a grayscale video capture card (8-bit, 640×480, 30 frm/sec) plugged into a computer. Figure 1.4(a) shows a typical beam cross-section density picture obtained via the combination of phosphor screen and video capturing system. Though the density resolution is only from 0 to 255, it is sufficient for accurate determinations of various particle distribution moments, e.g. $<x>$, $<y>$, $<x^2>$, $<y^2>$, $<xy>$, which are the key parameters for steering, matching and skew corrections. The detailed $x$ or $y$ density profile can also be used to reconstruct $(x,x')$

9

or $(y, y')$ phase space distribution. Moreover, some interesting physics phenomena like halo formation can be seen clearly from false-color visualizations of the original grayscale image (see Fig. 1.4b). Additionally, we can accurately determine the phosphor screen edge from the false-color image and hence calibrate the relation between the screen pixels and the real distance. The false-color imaging plus real-time display (30 frm/sec) is an important feature in our computerized control system. The control system including both hardware and software will be introduced in the next section.
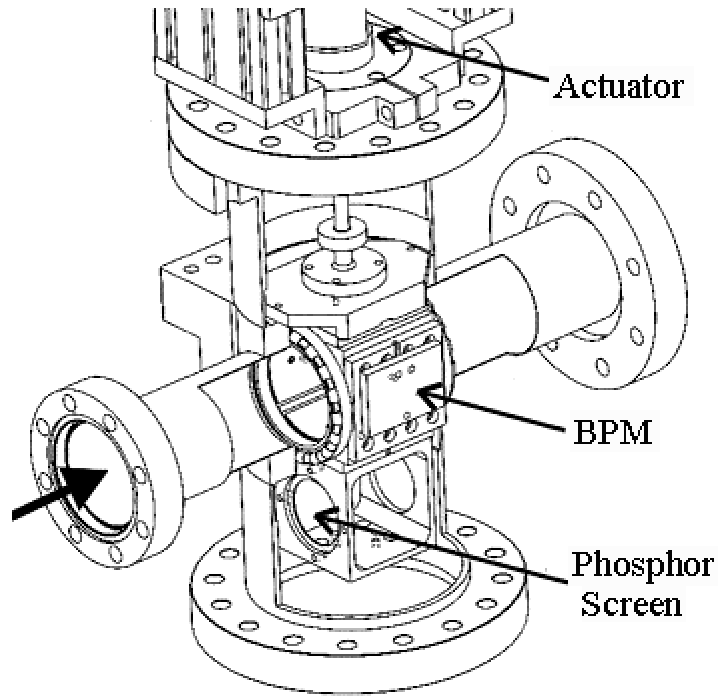


Figure 1.3: Diagram of diagnostic chamber.

<div align="center">(a)          (b)</div>
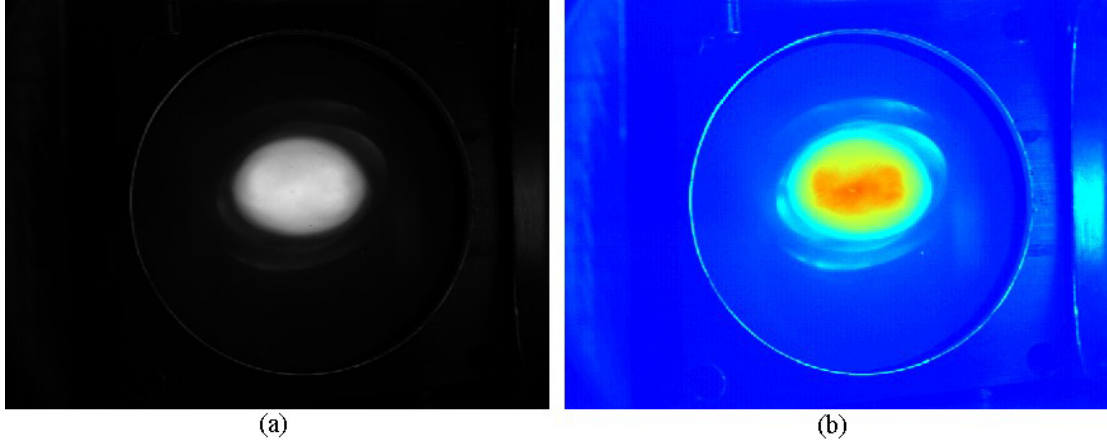
Figure 1.4: Typical beam cross-section density picture taken at the phosphor screen plane in a diagnostic chamber (256 colors, 640×480, phosphor screen diameter 1.25 inch). (a) grayscale; (b) false-color representation.

## 1.3 Beam Control System

The importance of beam control systems in advanced accelerators cannot be overemphasized. For instance, optimal steering in UMER can be done on a daily basis with the automatic control system, and the results are very reproducible. As another example, the on-site phase space mapping using a tomographic technique only takes about 10 minutes for a specific beam.

We introduce here the control system developed for UMER applications. It involves real-time control of quadrupoles, steering/bending dipoles and diagnostics. The latter consists of phosphor screens and beam position monitors placed in every diagnostic chamber. The diagram of the control system structure is illustrated in Figure 1.5. The system allows us to do systematic control of focusing/steering elements and image/signal processing from the diagnostics. The main functions of the

control system at present stage are: beam steering, skew corrections, empirical matching, emittance measurements and phase-space tomography. It not only allows us to operate the machine from the computer screen, but also provides function encapsulations to control and obtain the key beam parameters, i.e. centroid positions, rms transverse dimensions, cross-section rotation angle, etc. Moreover, a major feature of the system is its modularity: functional modules can be programmed and plugged into the system dynamically according to our needs. For example, one can write a halo-control program by iteratively changing currents of several injector quadrupoles and observing the halo changes in a diagnostic chamber.
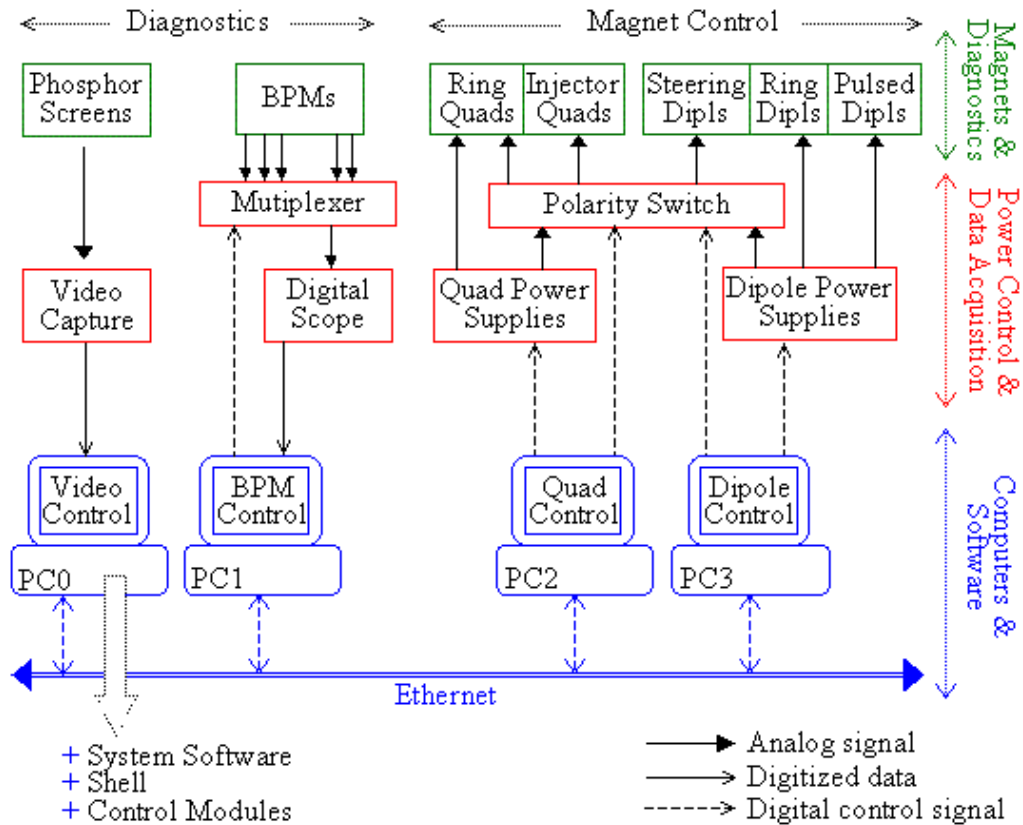


Figure 1.5: Diagram of UMER control system structure.

As shown in Fig. 1.5, the control system software is distributed over a number of computers. We could call it a distributed computer control system, but in the strict sense, it is a system that follows the client/server model. From a computer science point of view, the control system core and all the control application programs (steering, matching, etc.) are clients; the hardware control and data collection programs, on the other hand, are servers or service providers. The servers are responsible for driving power supplies, collecting data from oscilloscopes or cameras, and furthermore, processing the collected data or images to retrieve the key parameters for beam control, e.g. centroid, rotation angle and rms radius. The clients and servers communicate mostly through local Ethernet via predefined *protocols*, except for the "video control" server, which resides in the same computer with the system core for easier image data communication. Also, all the servers can be installed in the same computer if it can handle the loads. As a specification of the system, we have only defined the communication *protocols* between different servers and the system core. The servers can be implemented by any means as long as the *protocols* are followed. A direct advantage of this implementation is its transformability. It implies that the system core and the application programs can be used in other beam system (having similar control requirements) with little changes. The necessary work therefore may only involve re-programming the hardware control and data acquisition servers while maintaining the communication *protocols*.

The layered structure of the control system software is illustrated in Figure 1.6. At the bottom part is the operating system (OS). The targeted OS for the system

core and the control application programs is Microsoft Windows (9X, NT, 2000 or XP). The OS for the hardware control servers, however, could be a Linux or a Mac OS depending on the their implementations. In our case, all the servers are implemented in Microsoft Windows. In the figure, API stands for "application programming interface". It is a series of "C-program" functions that bridge the control applications and the system core. A programmer can easily implement a control application by linking it to the APIs without knowing the hardware details. For example, *SetQuadCurrent("QR3", 2.88)* is a call to set the current of a quadrupole named QR3 to 2.88 A; *SetDipoleCurrent("D1", 2.5)* is a call to set the current of a dipole named D1 to 2.5 A; *StartCapture( )* is a command to request the video system to start capturing beam images; *CalcCentroid(&x, &y)* asks for the present beam centroid position; *Calc2RmsRadius(&xrad, &yrad)* asks for the present beam radii; *SwitchBpm("BPM1")* is a command asking the multiplexer to switch to BPM1. One can refer to the manual of control system SDK [22] for a detailed description of the prototypes. The importance of the APIs resides in that they make the system expandable. This is the modularity we mentioned before. We currently have four main control applications: steering, skew corrections, empirical matching, and phase-space tomography. In the future, multi-turn operation requires better optimization routines added to the control system. With the help of APIs, a good mathematics background plus simple programming skills is all that is needed for the expansion of the control system. Finally, let us look at Figure 1.7 that shows a screen shot of the graphical user interface (GUI) of the control system. The black window at the bottom is the input/output *console* for the control applications (see the notation in Fig. 1.6). It

shows a running tomographic program to reconstruct the phase space distribution of the 0.6 mA beam in the sixth ring chamber (RC6). The false-color picture on the left represents a captured beam cross-section image, and the black/white one on the right the reconstructed phase space distribution. Readers can refer to Chap. 6 for a detailed description of the reconstruction process.
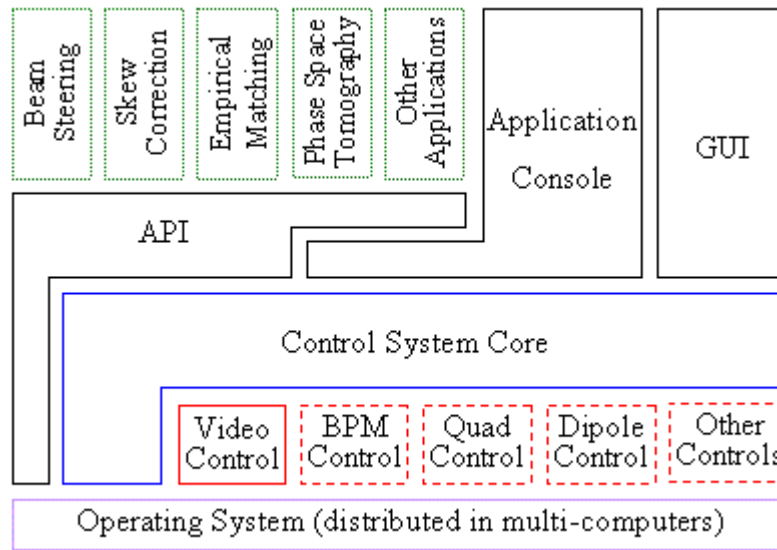
Figure 1.6: Layered structure of control system software.
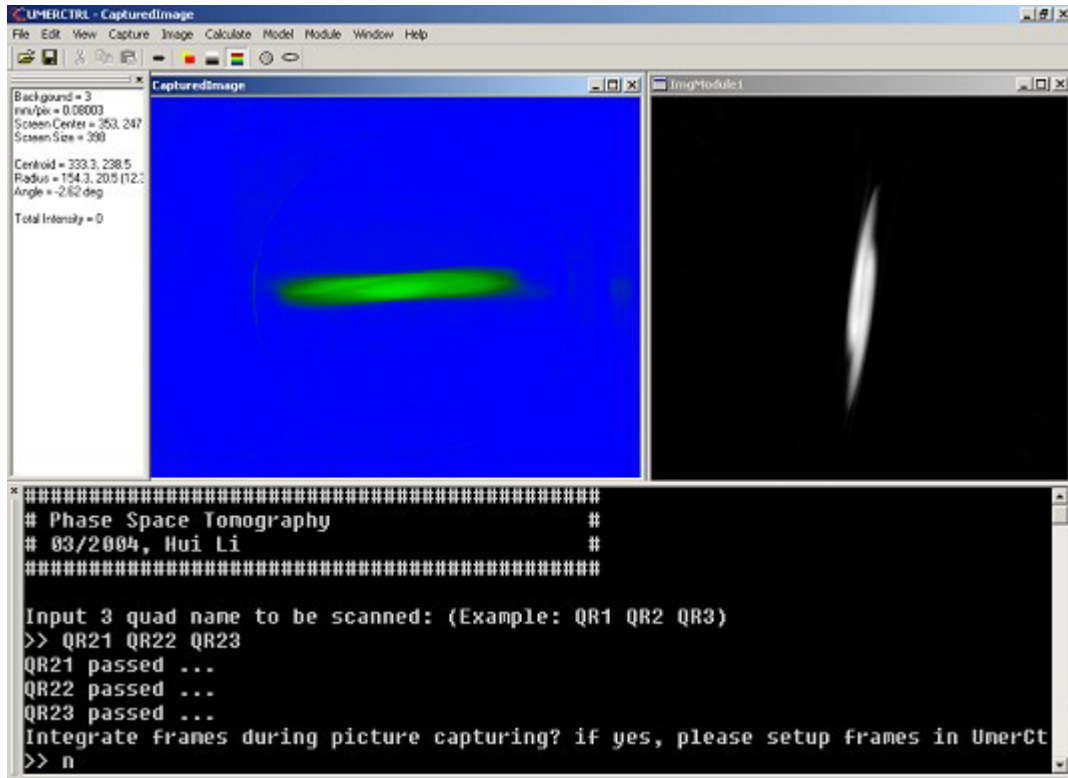
Figure 1.7: Screen shot of the GUI of the control system core.

## 1.4 Outline of this Dissertation

We organize the dissertation as follows. In Chap. 2, we present a scheme for optimal beam steering based on quadrupole scans. The idea is to use quadrupoles as beam position monitors. We developed a very sophisticated algorithm that involves two dipoles as the steering elements and two quadrupoles defining the target axes. The algorithm is very suitable for computer control. We also discuss certain experimental constraints related to the algorithm, in particular, the optics setup for avoiding singularity. The experimental results via the automatic steering program as mentioned earlier are reported for two low-intensity beams (0.6 mA and 7 mA). The

steering obtained here establishes baseline for the transport of other high-intensity beams (24mA an 100 mA).

In Chap. 3, we describe the development of a PC skew quadrupole for compensating beam rotation errors. Beam rotation errors are usually caused by the skewness of quadrupoles resulting from assembly and mounting errors. They can be detrimental to the beam quality, lead to beam distortions, mismatch, and a net increase in beam emittance. The skew quadrupole we developed can electronically rotate the quadrupole field with high accuracy, thus making skew correction possible. In order to gain a better understanding of the effects of rotated quadrupoles and to explore beam transport dynamics with rotation errors, we have designed a controlled experiment by deliberately introducing quadrupole rotation errors with our new quadrupole. The experimental observations agree very well with the simulated predictions. We hence employ the skew quadrupole in UMER for actual corrections.

In Chap. 4, we present matching studies for intense space-charge-dominated beams, such as in UMER. We employ both simple rms envelope codes and complex particle-in-cell (PIC) simulations to aid us in designing the beam optics. These studies have verified a dipole model that can be included into envelope codes. The advantage of envelope codes resides in their simplicity and their use for optimization of the matching section. The central issue here is matching of the beam from the electron gun through the injector into the ring lattice. The UMER injector has seven adjustable parameters (the strengths of one solenoid and six quadrupoles). Ideally, we only need four parameters to achieve rms matching, since there are four constraints ($x$, $y$ beam radii and slopes) for the problem as dictated by the results of periodic FODO

17

matching. An infinite number of solutions therefore exist for the matching section design. Our solution based on a brute-force method is presented. However, it is normal that the implementation of the calculated magnet strengths in a real experiment does not yield true matching conditions. We report at the end of chapter 4 an empirical matching technique to solve this problem.

In Chap. 5, a new optics design for beam injection in UMER is proposed for multi-turn operation. We first review a previous method that involves two pulsed and physically overlapping quadrupoles. The design and construction of these pulsed quadrupoles are difficult because of the requirements for fast switching and small mutual inductance. In addition, more complicated glass gap geometry with the overlapping magnets is required, which makes the design difficult to implement. In order to overcome these disadvantages, we have chosen a simpler scheme, which reduces both the mechanical and electrical complexities, but also makes the beam optics more complicated than in the former case. We present here calculation of the beam centroid motion as well as intense beam matching to evaluate the new design. The stability of the design is also discussed for multi-turn operation.

In Chap. 6, we report the implementation of beam phase space tomography in UMER. Tomographic imaging was originally developed in the medical community to process x-ray images. It reconstructs the two-dimensional image of a human object from information obtained at different angles. Phase space mapping can be done in a similar way by means of quadrupole scans. In this chapter, we present the general reconstruction theory, the implementation in UMER, and the experimental results for

the 0.6 mA and the 7 mA beam. For the latter beam, we also describe the method used to include the space-charge effects.

Finally, we summarize the dissertation in Chap. 7.

# Chapter 2 Beam Steering

The transport of intense beams over long distances requires that the beam centroid trajectory deviate as little as possible from the design orbit. In the ideal case, the axes of the magnets define the orbit. In practice, however, there are imperfections associated with the placement of magnets and beam position monitors (BPMs) and other diagnostics during the installation phase. Since these mechanical misalignments cannot be completely corrected by conventional optical surveying techniques, an alternative approach, beam-based alignment (BBA) [23], has become the tool of choice to compensate for the unavoidable mechanical problems. The idea behind conventional BBA is quite simple: a beam that is offset relative to a quadrupole axis will be deflected with an angle proportional to the quadrupole strength. The offset can therefore be corrected by iteratively making mechanical adjustments to the quadrupole and checking with changes in the quadrupole strength.

In UMER, we can achieve sub-millimeter mechanical accuracy for magnet positioning with the conventional optical surveying method [24]. However, the lack of room for magnet movers in small machines such as UMER makes the conventional BBA technique infeasible. In addition, the action of the Earth's field on the low energy electron beam orbit has to be taken into account. Under these circumstances, steering dipoles become very important in compensating for residual alignment errors and the influence from the Earth's field, as well as correcting other beam centroid errors. In this chapter, we will describe the steering algorithm based on the BBA method: the beam centroid errors are obtained by quadrupole scans, and corrections

implemented through steering dipoles. It is tested in UMER, but does not lose the generality to be used in other machines having similar problems.

## 2.1 Optimal Beam Steering

We assume that the horizontal ($x$) and vertical ($y$) beam steering are decoupled, which is usually the case. The steering algorithm works for both the planes. In figure 2.1, we illustrate a simple optics system that consists of two steering dipoles ($S_1$, $S_2$), a quadrupole ($Q_1$) and a beam detector. In order to steer the beam towards the axis of $Q_1$, $S_1$ is used to correct the position error, and $S_2$ to correct the angle error. Hence, the problem of beam steering becomes finding the right deflection angles $\Delta\theta_1$ and $\Delta\theta_2$ induced by the dipoles, where $\Delta\theta_1 = \alpha_s \cdot I_{S1}$, $\Delta\theta_2 = \alpha_s \cdot I_{S2}$, $I_{S1}$ and $I_{S2}$ are the currents to the dipoles, and $\alpha_s$ is a constant coefficient meaning the deflection angle resulting from a unit current. The detector downstream of $Q_1$ can be either a BPM or a phosphor screen. By varying the strength of $Q_1$, we can find a group of combinations ($I_{S1}$, $I_{S2}$) which all steer the beam through $Q_1$'s center. Among these pairs of dipole settings, only one solution ($I_{S1}$, $I_{S2}$) will steer the beam through $Q_1$'s axis. This can be determined only if the detector is calibrated with respect to the axis of $Q_1$, which is normally not guaranteed, especially for the phosphor screens in our case.
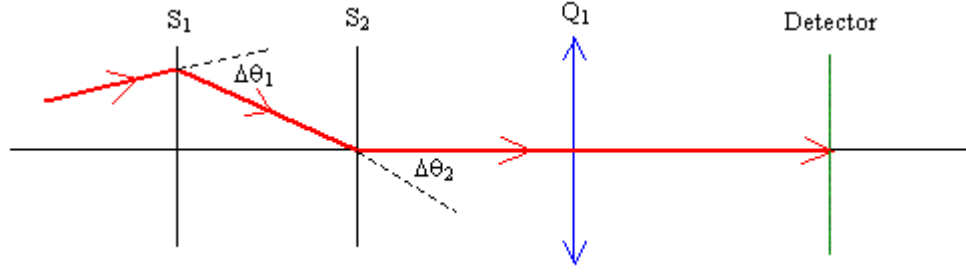
Figure 2.1: Steering optics: two steering dipoles ($S_1$, $S_2$), a quadrupole ($Q_1$) and a beam detector (phosphor screen or capacitive BPM).

For steering purposes, we prefer smaller beams so as to avoid the image-charge effects of large beams. We therefore choose two low-current beams to establish a baseline for steering in UMER: 0.6 mA and 7 mA (see Table 1.2). Since the signal-to-noise ratio of our BPMs is lowest with the smallest beam currents, we use a phosphor screen to more accurately determine the beam positions. The phosphor screens are placed under the BPMs inside each diagnostic chamber (see Fig. 1.3), which can be raised up to the beam-line by means of an actuator. The geometric centers of the screens are therefore not normally aligned with adjacent quadrupoles. To avoid the problem of finding the location of the phosphor screen center relative to the adjacent quadrupole center, we need to implement a steering algorithm that is independent of the absolute center of the screen. This requires scanning two quadrupoles located upstream from the detector. We illustrate the algorithm in Figure 2.2, where the detector center is not aligned with the reference orbit defined by the centers of $Q_1$ and $Q_2$ (the polarities of $Q_1$ and $Q_2$ are reversed because it is a FODO system). The steering procedure, which uses two quadrupoles, can be summarized in two steps: (1) look for several points in the two-dimensional space ($I_{S1}$, $I_{S2}$)

22

corresponding to beams going through the center of $Q_1$ (this is done by scanning $Q_1$'s current and observing the beam position change on the screen); (2) scan $Q_2$ to determine which point ($I_{S1}$, $I_{S2}$) is the optimal.
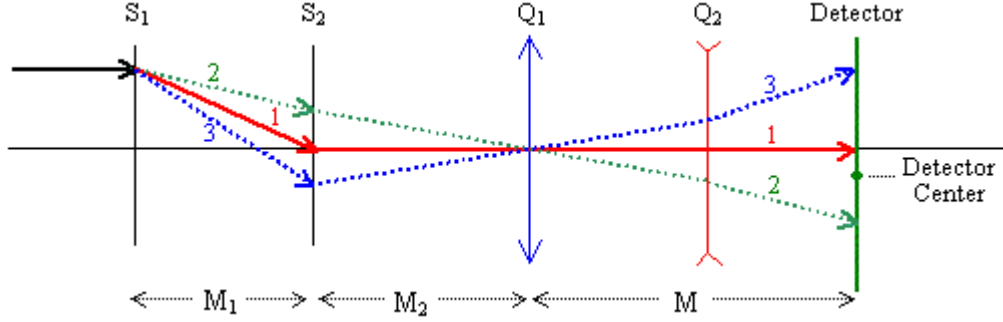


Figure 2.2: Schematics of basic steering unit: two steering dipoles ($S_1$, $S_2$), two quadrupoles ($Q_1$, $Q_2$), and a beam detector (phosphor screen or capacitive BPM). The beam centroid trajectory "1" corresponds to the optimal steering. $M_1$, $M_2$, M are transfer matrices from $S_1$ to $S_2$, $S_2$ to $Q_1$, and $Q_1$ to the detector, respectively.

As for the first step, the question is how to find the right current combinations ($I_{S1}$, $I_{S2}$) that will bend the beam towards $Q_1$'s center. Intuitively, $I_{S1}$ and $I_{S2}$ will lie on a straight line because linear optics dominates the beam centroid motion when misalignments are relatively small. This is apparent if we assume that the steering dipoles $S_1$, $S_2$ and the quadrupole $Q_1$ are thin lenses. The beam's position $x_{q1}$ and slope $x'_{q1}$ just before $Q_1$ can be represented by

$$\begin{pmatrix} x_{q1} \\ x'_{q1} \end{pmatrix} = M_2 \cdot M_1 \cdot \begin{pmatrix} x_0 \\ x'_0 \end{pmatrix} + M_2 \cdot M_1 \cdot \begin{pmatrix} 0 \\ \Delta\theta_1 \end{pmatrix} + M_2 \cdot \begin{pmatrix} 0 \\ \Delta\theta_2 \end{pmatrix}, \tag{2.1}$$

where $x_0$ and $x'_0$ are the initial beam's position and slope just before $S_1$; $M_1$ and $M_2$

are the transfer matrices from $S_1$ to $S_2$, and $S_2$ to $Q_1$, respectively; $\Delta\theta_1 = \alpha_s \cdot I_{S1}$ and

$\Delta\theta_2 = \alpha_s \cdot I_{S2}$ are the deflection angles induced by $S_1$ and $S_2$. Equation 2.1 can be

further simplified in terms of $I_{S1}$ and $I_{S2}$, i.e.

$$\begin{pmatrix} x_{q1} \\ x'_{q1} \end{pmatrix} = \begin{pmatrix} a_0 + a_1 I_{S1} + a_2 I_{S2} \\ b_0 + b_1 I_{S1} + b_2 I_{S2} \end{pmatrix}, \tag{2.2}$$

where $a_0$, $a_1$, $a_2$, $b_0$, $b_1$ and $b_2$ are a number of parameters related to Eq. 2.1, the

transfer matrices, the initial beam position, and slope. Steering beams to the center of

$Q_1$ implies $x_{q1} = 0$, thus requiring the current relation: $a_0 + a_1 I_{S1} + a_2 I_{S2} = 0$.

Unfortunately, we are unable to calculate $a_0$, $a_1$, $a_2$, since the initial beam position $x_0$

and the angle $x'_0$ are unknown to us. In practice, the determinations of $a_0$, $a_1$, $a_2$ must

come from the actual measurements relying on scanning $Q_1$ and observing the effects

from the detector.

At the detector's location, the beam's position $x$ and slope $x'$ can be written as

$$\begin{pmatrix} x \\ x' \end{pmatrix} = M \cdot M_{q1} \cdot \begin{pmatrix} x_{q1} \\ x'_{q1} \end{pmatrix}, \tag{2.3}$$

where $M_{q1} = \begin{pmatrix} 1 & 0 \\ 1/f_1 & 1 \end{pmatrix}$, $M = \begin{pmatrix} m_{11} & m_{12} \\ m_{21} & m_{22} \end{pmatrix}$ are the transfer matrix of $Q_1$ and the

transfer matrix from $Q_1$ to the detector, respectively; $f_1$ is the focal length of the

quadrupole. Using the fact that $1/f_1 = \alpha_{q1} \cdot I_{q1}$ where $\alpha_{q1}$ is a constant coefficient

and $I_{q1}$ is the current to the quadrupole, we obtain

$$x = (m_{11} + m_{12}\alpha_{q1} I_{q1})(a_0 + a_1 I_{S1} + a_2 I_{S2}) + m_{12}(b_0 + b_1 I_{S1} + b_2 I_{S2}). \tag{2.4}$$

The change of $x$ with respect to the change of $I_{q1}$ can be derived from Equation 2.4. That is

$$\Delta x = m_{12}\alpha_{q1}\Delta I_{q1} \cdot (a_0 + a_1 I_{S1} + a_2 I_{S2}). \qquad (2.5)$$

This equation shows the relative beam position change in the detector in terms of $I_{S1}$, $I_{S2}$ and $\Delta I_{q1}$, provided $a_1 \neq 0$, $a_2 \neq 0$ and $m_{12} \neq 0$ (see the discussion in this section end). If $\Delta I_{q1}$ is kept the same during the steering, $\Delta x$ will be a linear function of $I_{S1}$ and $I_{S2}$, i.e.

$$\Delta x = \Delta x(I_{S1}, I_{S2}) = A_0 + A_1 \cdot I_{S1} + A_2 \cdot I_{S2}, \qquad (2.6)$$

where $(A_0, A_1, A_2) = m_{12}a_{q1}\Delta I_{q1} \cdot (a_0, a_1, a_2)$.

Steering beams to the center of $Q_1$ requires $x_{q1} = (a_0 + a_1 I_{S1} + a_2 I_{S2}) = 0$ from the previous analysis. It is equivalent to $A_0 + A_1 \cdot I_{S1} + A_2 \cdot I_{S2} = 0$. Noticing $\Delta x$ is a linear plane function in terms of $I_{S1}$ and $I_{S2}$, we can obtain the unknown parameters $A_0$, $A_1$, $A_2$ by a linear regression of $\Delta x$ with respect to the variables $I_{S1}$, $I_{S2}$.

To make the above process clear, let us look at Figure 2.3, which demonstrates a steering experiment with a 0.6 mA electron beam in the second chamber (IC2) of the UMER injector. In Fig. 2.3, $\Delta x$ represents the relative beam position motion in the phosphor screen when the strength of its upstream quadrupole (IQ3) is changed; $I_{S1}$ and $I_{S2}$ indicate the currents of the two steering dipoles upstream of IQ3. There are 45 (5 × 9) grid points measured in this experiment. For each pair $(I_{S1}, I_{S2})$, $\Delta x$ was measured by calculating the difference between two beam positions corresponding to $\Delta I_{Q3} = 2A$, i.e. $\Delta x = x(I_{IQ3} + 1A) - x(I_{IQ3} - 1A)$, where the unit for $x$

is pixel as shown in the figure. Using the 45 grid points ($I_{S1}$, $I_{S2}$, $\Delta x$), we obtained the plane parameters $A_0$, $A_1$, $A_2$ by the two-dimensional linear regression. The results are, $A_0 = -13.095$, $A_1 = 23.903$, $A_2 = 3.358$. Therefore, the required dipoles' current setting for steering beams to $Q_1$'s center is $I_{S2} = -(A_0 + A_1 I_{S1})/A_2 = 3.900 - 7.118 \cdot I_{S1}$. The goodness-of-fit for this regression is 0.99998, which is calculated by

$$1 - \frac{\sum_i (z_i - \hat{z}_i)^2}{\sum_i (z_i - \bar{z})^2},$$ (2.7)

where $z = \Delta x$, $\hat{z} = A_0 + A_1 I_{S1} + A_2 I_{S2}$, and $\bar{z}$ is the average of $\Delta x$.
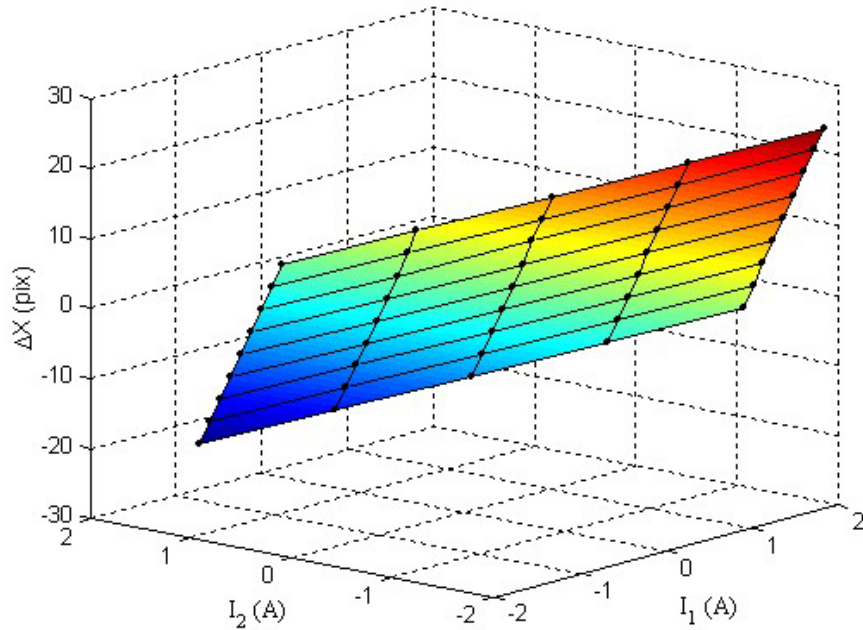


Figure 2.3: Parameter fitting for $A_0$, $A_1$, $A_2$ in the injector diagnostics chamber IC2. $\Delta x$ was measured by changing the quadrupole (QR3) current $\Delta I_{Q3} = 2A$. The goodness-of-fit equals 0.99998, $A_0 = -13.095$, $A_1 = 23.903$, $A_2 = 3.358$.

Let us look at another steering experiment that was carried out at the seventh ring chamber (RC7) in UMER. There are 50 (5 × 10) grid points measured in the experiment. They are plotted in Figure 2.4. The two-dimensional linear regression yields $A_0 = -350.278$, $A_1 = 119.617$, $A_2 = 23.117$. The data looks a little noisy, but the fitting is still very good (the goodness-of-fit equals 0.99903).
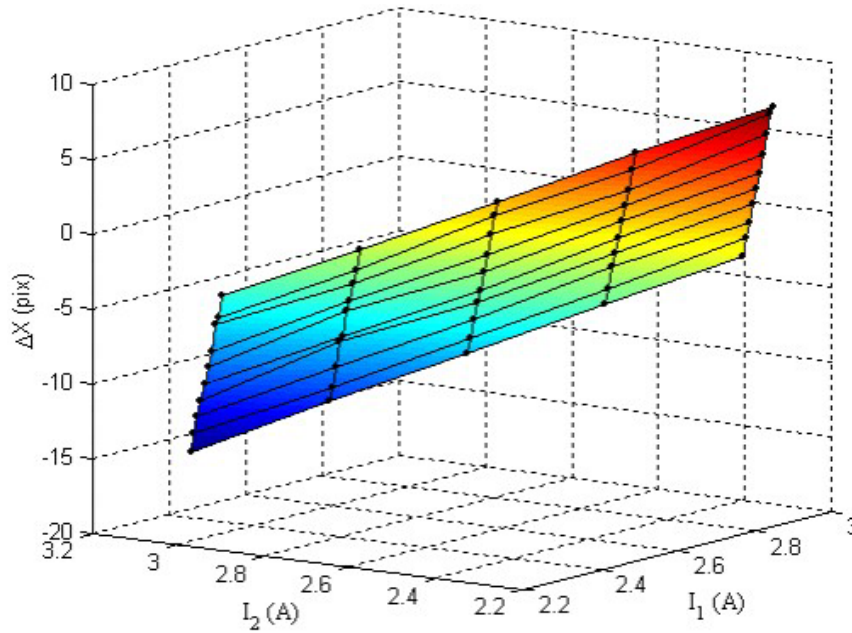


Figure 2.4: Parameter fitting for A0, A1, A2 in the ring diagnostics chamber RC7. Δx was measured by changing the quadrupole (QR27) current $\Delta I_{QR27}$ = 2A. The goodness-of-fit equals 0.99903, $A_0 = -350.278$, $A_1 = 119.617$, $A_2 = 23.117$.

The next question is how to find the optimal point ($I_{S1}$, $I_{S2}$) from the straight line $I_{S2} = -(A_0 + A_1 I_{S1})/A_2$. If we apply this relation on the steering dipoles ($S_1$, $S_2$), the beam position and slope at $Q_1$ have the form:

$$\begin{pmatrix} x_{q1} \\ x'_{q1} \end{pmatrix} = \begin{pmatrix} 0 \\ c_0 + c_1 I_{S1} \end{pmatrix},$$  (2.8)

where $c_0 = b_0 - a_0/a_2$, $c_1 = b_1 - b_2 \cdot a_1/a_2$ according to Eq. 2.2, provided $a_2 \neq 0$. If

we assume that it is a drift space from $Q_1$ to $Q_2$ (see Fig. 2.2), the beam's position $x$

and slope $x'$ at the detector location can be represented by

$$\begin{pmatrix} x \\ x' \end{pmatrix} = \begin{pmatrix} t_{11} & t_{12} \\ t_{21} & t_{22} \end{pmatrix} \cdot \begin{pmatrix} 1 & 0 \\ \alpha_{q2}I_{q2} & 1 \end{pmatrix} \cdot \begin{pmatrix} 1 & d \\ 0 & 1 \end{pmatrix} \cdot \begin{pmatrix} x_{q1} \\ x'_{q1} \end{pmatrix},$$  (2.9)

where $I_{q2}$ is the current of $Q_2$; where $\alpha_{q2}$ is a constant coefficient relating to $Q2$'s

focal length ($1/f_2 = \alpha_{q2} \cdot I_{q2}$); $d$ is the distance from $Q_1$ to $Q_2$; [$t_{11}$, $t_{12}$; $t_{21}$, $t_{22}$] is the

transfer matrix from $Q_2$ to the detector. Here, we make use of the fact that $Q_1$ does not

affect the beam centroid when the beam is centered in $Q_1$. We therefore derive $x$ from

Equation 2.9, i.e.

$$x = (d \cdot t_{11} + d \cdot \alpha_{q2}I_{q2} \cdot t_{12} + t_{12}) \cdot (c_0 + c_1 I_{S1}).$$  (2.10)

The relative beam position changes caused by the quad current change of $Q_2$ equals

$$\Delta x = d \cdot t_{12} \alpha_{q2} \Delta I_{q2} \cdot (c_0 + c_1 I_{S1}).$$  (2.11)

Given a constant $\Delta I_{q2}$ during the steering, $\Delta x$ is linearly dependent on $I_{S1}$, provided

$c_1 \neq 0$, $t_{12} \neq 0$ (see the discussion in this section end), i.e.

$$\Delta x = \Delta x(I_{S1}) = C_0 + C_1 \cdot I_{S1},$$  (2.12)

where $(C_0, C_1) = d \cdot t_{12} \alpha_{q2} \Delta I_{q2} \cdot (c_0, c_1)$.

In the experiment, we can measure the beam position change $\Delta x$ (by varying

the current of $Q_2$) corresponding to a point ($I_{S1}$, $I_{S2}$) lying on the line

$I_{S2} = -(A_0 + A_1 I_{S1})/A_2$. Thus, choosing a number of points along the line, we will

obtain a group of ($I_{S1}$, $\Delta x$) pairs. These data can be further used to calculate the unknown parameters $C_0$ and $C_1$ via a linear regression. Therefore, the optimal currents ($\hat{I}_{S1}$, $\hat{I}_{S2}$) for the two steering dipoles can be given in terms of $C_0$, $C_1$, $A_0$, $A_1$ and $A_2$ (provided $C_1 \neq 0$ and $A_2 \neq 0$), i.e.

$$\hat{I}_{S1} = -C_0 / C_1, \tag{2.13a}$$

$$\hat{I}_{S2} = -(A_0 + A_1 \hat{I}_{S1})/A_2. \tag{2.13b}$$

From a previous example shown in Fig. 2.3, we already obtained the linear current relation between $I_{S1}$ and $I_{S2}$, i.e. $I_{S2} = 3.900 - 7.118 \cdot I_{S1}$, which will steer beams through $Q_1$'s center. To obtain $C_0$ and $C_1$, we chose nine points from the fitted line, and applied these currents ($I_{S1}$, $I_{S2}$) to the steering dipoles $S_1$ and $S_2$. For each ($I_{S1}$, $I_{S2}$), we measured the relative beam position motion on the screen while varying $Q_2$ by 2A. Figure 2.5 shows the beam position change $\Delta x$ with respect to $I_{S1}$. The linear regression yielded $C_0$ = 88.944 and $C_1$ = 154.93. The goodness-of-fit is 0.9996. We therefore obtained the optimal currents ($\hat{I}_{S1}$, $\hat{I}_{S2}$) from Eqs. 2.13(a), 2.13(b). The results are $\hat{I}_{S1}$ = 0.574A and $\hat{I}_{S1}$ = −0.187A.
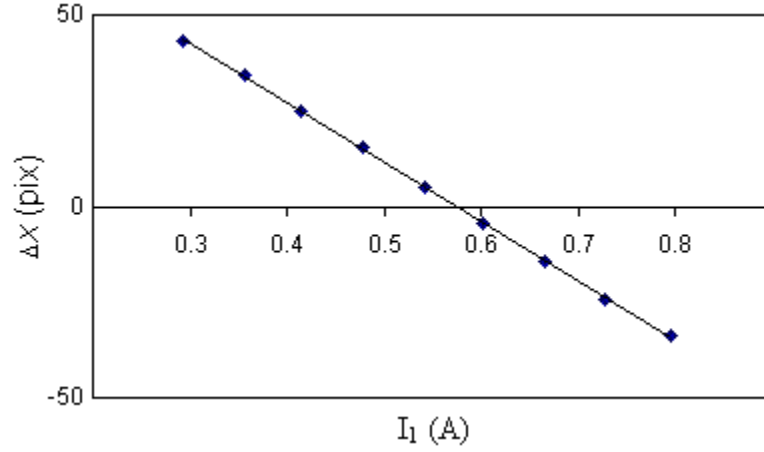
Figure 2.5: Parameter fitting for $C_0$ and $C_1$ in the injector diagnostics chamber IC2. $\Delta x$ was measured by changing the quadrupole (QR4) current $\Delta I_{Q4} = 2A$. The goodness-of-fit equals 0.9996, $C_0 = 88.944$, $C_1 = 154.93$.

We have derived a nice procedure for optimal steering based on the optics setup shown in Fig. 2.2, but we still made some assumptions about a number of optics parameters, i.e. $a_1 \neq 0$, $a_2 \neq 0$, $m_{12} \neq 0$, $c_1 \neq 0$, $t_{12} \neq 0$. If any of them equals or approaches zero, the steering experiment will fail, which can be seen from Eq. 2.5, $\Delta x = m_{12}\alpha_{q1}\Delta I_{q1} \cdot (a_0 + a_1 I_{S1} + a_2 I_{S2})$ and Eq. 2.11, $\Delta x = d \cdot t_{12}\alpha_{q2}\Delta I_{q2} \cdot (c_0 + c_1 I_{S1})$. Therefore, we need to know under what conditions potential singularities about these parameters ($a_1$, $a_2$, $c_1$, $m_{12}$, and $t_{12}$) may occur. Examining Eqs. 2.1 and 2.2, we found.

$$a_2 = \alpha_s \cdot m2_{12}, \tag{2.14a}$$

$$a_1 = \alpha_s \cdot m3_{12}, \tag{2.14b}$$

where we define $m2_{12}$, $m3_{12}$ according to the transfer matrices,

$$M_1 = \begin{pmatrix} m1_{11} & m1_{12} \\ m1_{21} & m1_{22} \end{pmatrix}, \; M_2 = \begin{pmatrix} m2_{11} & m2_{12} \\ m2_{21} & m2_{22} \end{pmatrix}, \; \text{and} \; M_3 = M_2 \cdot M_1 = \begin{pmatrix} m3_{11} & m3_{12} \\ m3_{21} & m3_{22} \end{pmatrix}. \text{ We}$$

can therefore avoid the singular cases for $a_1$, $a_2$, by carefully choosing the optics setup

for $M_1$ and $M_2$ such that $m2_{12} \neq 0$ and $m3_{12} \neq 0$. Also for the parameter

$c_1 = b_1 - b_2 \cdot a_1 / a_2$ (see Eq. 2.8), explicitly expressing it in terms of the matrix

elements of $M_1$ and $M_2$, we found

$$c_1 = -\alpha_s \cdot m1_{12} / m2_{12}, \tag{2.14c}$$

which requires $m1_{12} \neq 0$.

We therefore have five constraints for the steering: (1) $m1_{12} \neq 0$; (2)

$m2_{12} \neq 0$; (3) $m3_{12} \neq 0$; (4) $m_{12} \neq 0$; (5) $t_{12} \neq 0$. Here, $m1_{12}$, $m2_{12}$, $m3_{12}$, $m_{12}$, and

$t_{12}$ share a common property, i.e. having the same location in their transfer matrices.

Reviewing the general form of a transfer matrix from *general theory of Courant and*

*Snyder* [25, 26], we know that a "*0*" element in the first row and second column of a

transfer matrix indicates that the betatron phase-advance equals n·π (n = integer). For

that reason, we must avoid a betatron phase-advance of n·π occurring for the regions

corresponding to the matrix $M_1$, $M_2$, $M_3$, M and T. Explicitly, they are the regions

from $S_1$ to $S_2$, $S_2$ to $Q_1$, $S_1$ to $Q_1$, $Q_1$ to the detector, and $Q_2$ to the detector,

respectively. In designing a steering experiment, we must pay attention to those

restrictions. Otherwise, the experiment would fail.

## 2.2 Beam Steering Experiments

As discussed in Chapter I, the lattice in UMER consists of 36 FODO periods, distributed in 18 twenty-degree bending sections. Each FODO period includes two quadrupoles in a straight section, with one bending dipole between FODO cells. Ideally, a dipole bends the beam in the horizontal plane by 8 deg., approximately, while the vertical component of the Earth's magnetic field introduces an additional 2 deg. deflection. However, the Earth's field varies (0.2 to 0.5 Gauss) around the lattice. The actual deflection angles resulting from the Earth's field for different places are difficult to measure in practice. Under these circumstances, the ring dipoles need to be adjusted individually so they can compensate for the changing Earth fields and the other mechanical errors.

In the steering experiment for first-turn operation, we treat the ring dipoles as horizontal steering elements. The goal is to find the "right" current for each dipole, which will reflect a local optimum based on the local Earth's field and other mechanical errors. This will establish a baseline for multi-turn operation. In the future, the global optimization of the multi-turn steering must lie in the vicinity of the dipole setting found here.

Figure 2.6 illustrates three ring sections of the UMER lattice, each of which consists of one diagnostic chamber and two FODO cells. In the figure, D1 to D6 are ring dipoles; QR2 to QR13 are quadrupoles; RC1 to RC3 are diagnostic chambers where the phosphor screens and BPMs are located inside. If we aim to find the optimal currents of D2 and D3, the two quadrupoles to be scanned are QR7 and QR8. The diagnostic chamber involved is not only RC2, but also RC3. These six elements

32

(two dipoles, two quadrupoles, two chambers) define a basic steering unit, which satisfies all the requirements we discussed in the last section. For example, the betatron phase-advance from D2 to D3 is $76^o$ for this case, which avoids $c_1 = 0$.
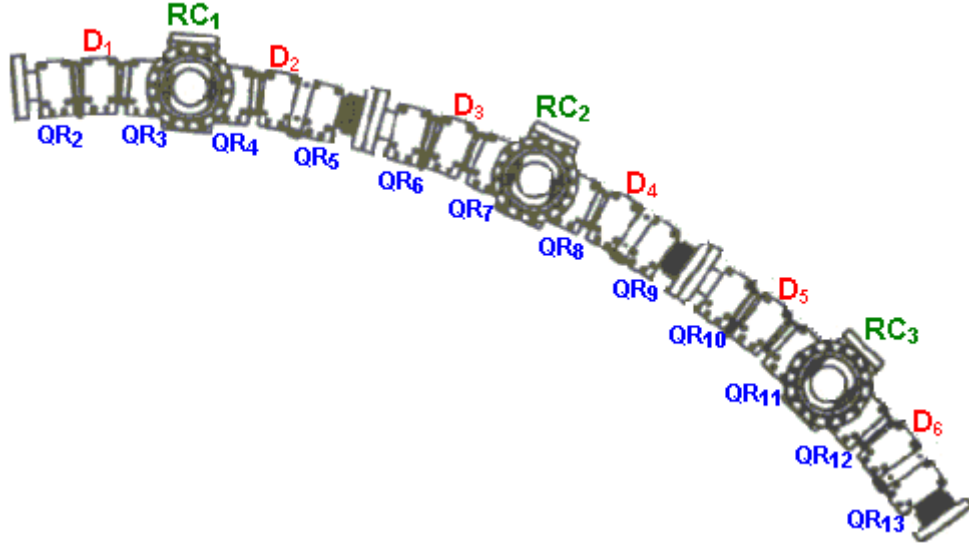


Figure 2.6: Layout of three ring sections: $D_1$ to $D_6$ are ring dipoles; $QR_2$ to $QR_{13}$ are ring quadrupoles; $RC_1$ to $RC_3$ are diagnostics chambers.

The steering procedure is almost the same as that discussed in the previous section. There are two steps: (1) Scan QR7 and use the screen/BPM inside RC2 to find the linear dipole current relation between D2 and D3. This will steer beams through QR7's center. (2) Apply these dipole currents, scan QR8, and observe in RC3 to find the optimal currents from Eqs. 2.13(a) and 2.13(b). The only difference between this implementation and the previous algorithm is that we use two diagnostic

chambers instead of one. Similarly, if we want to find the dipole currents of D4 and D5, the involved quadrupoles and chambers are QR11, QR12, RC3 and RC4.

There are several points worth noting. (1) We must do the steering sequentially. That is, we need to first find the dipole currents of D0 and D1 by scanning QR3 and QR4; then find the currents of D2 and D3 by scanning QR7 and QR8, and so on. (2) The two scanned quadrupoles for each steering unit, e.g. QR7 and QR8, need to reside in a straight section. Though the algorithm still works when a bend is between the two quadrupoles, the optimal steering may lead to a solution that only steers the beam through the centers of both quadrupoles, but not their axis. It is because there is a bending dipole between them and the optimal setting of that dipole is still unknown in this case. (3) In reality, we can steer the beam through the centers of only half the ring quadrupoles, because the number of dipoles is one half the number of quadrupoles, e.g. (QR3, QR4), (QR7, QR8), (QR11, QR12), etc. These centers actually define the reference orbit for the ring. (4) The translation error of the quadrupole mounting in the $x$ and $y$ directions is only about 0.05 mm [24]. The beam, therefore, in general would not deviate much from the centers of the other half quadrupoles.

As mentioned before, we choose two low-current beams (0.6 mA and 7 mA) for steering in UMER to avoid the image-charge effects of large beams. 0.6 mA is the lowest current we have in UMER. We call it the pencil beam. It has the smallest beam radius and induces the weakest image charge effect among all beams. In order to detect its position, we must employ the phosphor screens and the video capturing system. Computer control of both dipole and quadrupole currents, combined with

real-time image processing, has made this a very powerful tool for optimal beam steering in UMER. The results are highly reproducible, with an uncertainty in dipole currents corresponding to beam position changes on the screen of only one pixel, or 0.08 mm, approximately.

Let us look at the experimental results for the pencil beam. The dipole currents of D0 to D21 (from ring chamber RC1 to RC11) are plotted in Figure 2.7. Since the vertical component of the Earth's fields are cancelled for the first three dipoles by a Helmholtz coil, the average current of $D_0$, $D_1$, and $D_2$ is 2.95 A, which is approximately the dipole current to bend the beams by 10 degrees. The average current of the other downstream dipoles is 2.43 A. It indicates the average vertical Earth field of about 350 mG. The variations of dipole currents reflect the non-uniformity of the Earth's fields and mechanical mounting errors associated with the magnets.
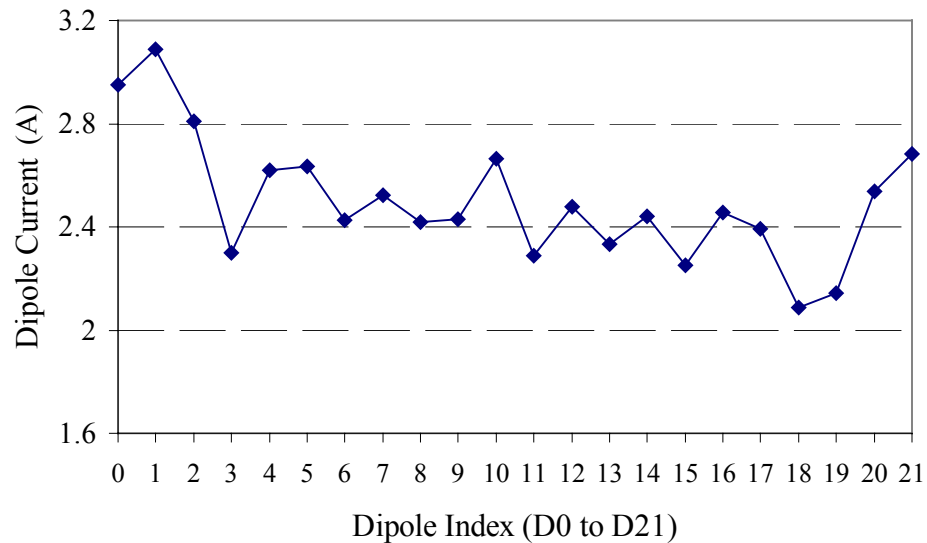


Figure 2.7: Dipole currents from the steering experiment for a pencil beam (0.6 mA).

We also carried out the steering experiment using the 7 mA beam. The optimal dipole currents are plotted in Figure 2.8 in comparison to the pencil beam. The advantage of using this beam lies in the possibility of employing BPMs to measure the beam position change. The measurement process with BPMs is much faster than with the phosphor screens, but the resolution of BPMs is still not high for this beam. Although the steering process with the video system involves repeatedly moving the screens and re-focusing the cameras, it gives more reliable and accurate results. Therefore, we still chose the video system for the 7 mA beam's steering. From Fig. 2.8, the results for the two beams agree very well. It demonstrates the high accuracy of this steering method.
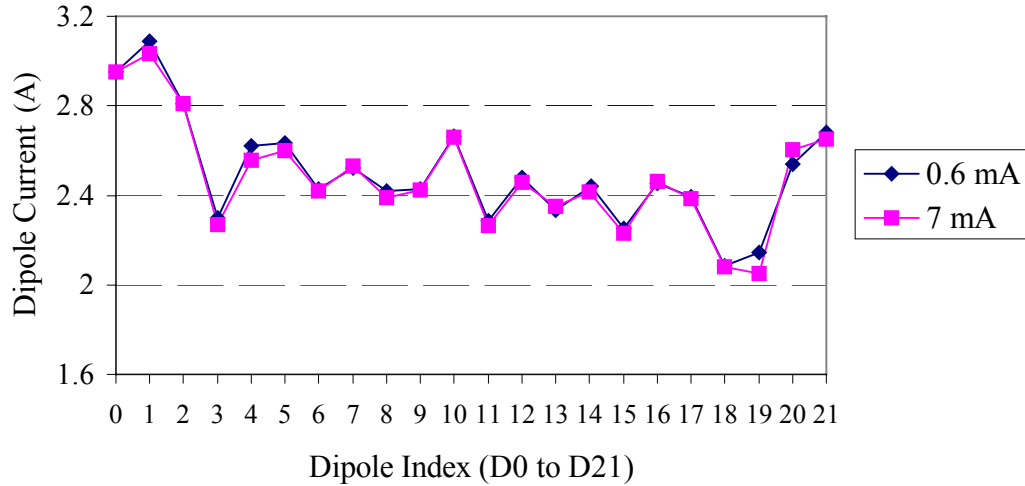


Figure 2.8: Dipole currents from the steering experiment for a 7 mA beam.

## Chapter 3 Beam Rotation Correction

Beam rotation (skew) errors about the magnet axis, resulting from assembly and mounting errors, can be detrimental to the beam quality. A rotated quadrupole imparts an angular momentum to the beam, which will then rotate back and forth. This rotation manifests itself as an rms envelope mismatch, and the extra degrees of freedom lead to additional envelope modes not present in the normal case [27, 28]. These additional mismatch modes can result in faster emittance growth and accelerated halo formation [29]. In UMER, the mechanical skew errors of quadrupole mounts can be controlled to within 1 mrad. However, the errors from the assembly of the printed circuits on the aluminum mounts and the accumulated skew errors from multi-quadrupoles may be more problematic. Thus, we have developed a new type of magnet, called printed-circuit (PC) skew quadrupole [14] to compensate for the beam rotation errors.

The skew corrector is very easy to implement using PC magnet, but also can be implemented with other magnets. We developed a general correction scheme and demonstrated that it can reduce beam rotations and improve beam quality in UMER. The way used to build the corrector and the method used in the correction can be applied to other applications having similar rotation problems. We organize this chapter as follows: the design of the new magnet, field measurements using a rotating coil magnetometer, beam test in the injector line and finally, an actual correction experiment in the ring lattice.

## 3.1 Skew Quadrupole Design

As is well known, the cylindrical components of the magnetic field of an ideal quadrupole are given by

$$B_r = g_0 r \sin 2\theta, \tag{3.1a}$$

$$B_\theta = g_0 r \cos 2\theta, \tag{3.1b}$$

where $g_0$ is the field gradient; $B_r$ and $B_\theta$ are the so-called normal components. The corresponding skew components are introduced by a quadrupole rotation in the $\theta$ direction. Below, we concentrate on $B_\theta$, but similar expressions apply to $B_r$. If $\alpha$ is the quadrupole rotation angle, the rotated field $B_\theta$ is given by

$$B_\theta = g_0 r \cos 2(\theta - \alpha) = B_n + B_s, \tag{3.2a}$$

$$B_n = \cos(2\alpha) g_0 r \cos(2\theta), \tag{3.2b}$$

$$B_s = \sin(2\alpha) g_0 r \sin(2\theta), \tag{3.2c}$$

where $B_n$ and $B_s$ are the normal and skew quadrupole components, respectively. Usually, the rotation angle $\alpha$ is small so that $B_s$ is very small compared with $B_n$, which further simplifies the formulas to

$$B_n = g_0 r \cos(2\theta), \tag{3.3a}$$

$$B_s = 2\alpha g_0 r \sin(2\theta). \tag{3.3b}$$

In designing a PC skew quadrupole, we use two pairs of printed circuits, one of which is the normal PC, and the other one is the skew PC. The latter is mounted over the main PC with a $45^\circ$ rotation. As described, both PCs are regular magnets. The only difference is the way they are mounted. Figure 3.1(a) illustrates the relative

placement of the skew and normal quadrupoles, while Figure 3.1(b) shows a photo of a disassembled main PC quadrupole together with the added skew quadrupole. The two PCs are attached closely together and to an aluminum mandrel.



(a)

(b)
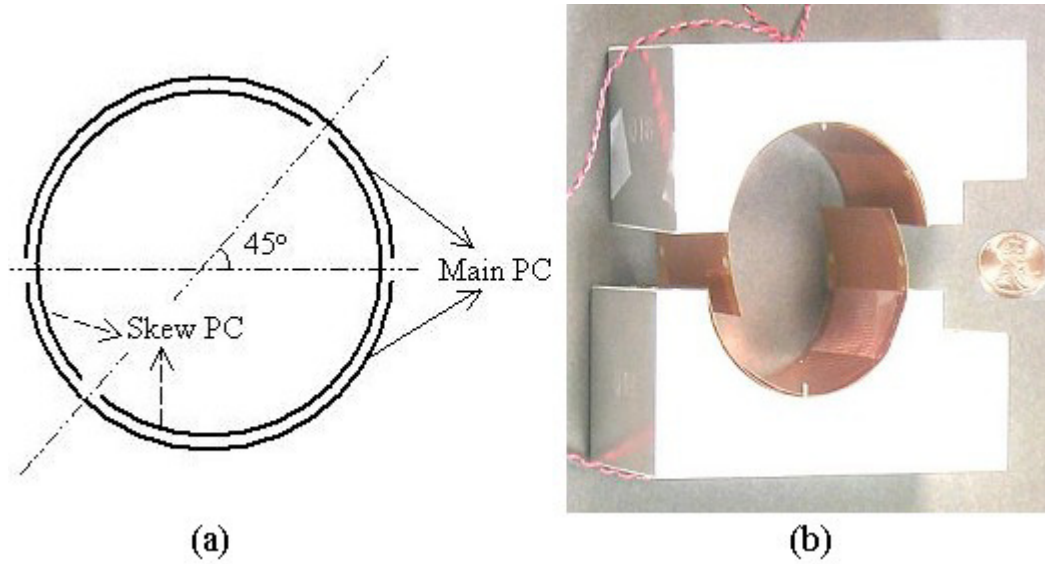
Figure 3.1: Layout of a PC skew quadrupole and a normal (main) quadrupole. (a) schematic layout; (b) photo of main and skew quadrupole assembly.

The main and skew quadrupoles are powered by different current supplies, so that the normal and skew components can be independently adjusted. The theoretical rotation angle is calculated according to

$$\alpha = 0.5\tan^{-1}(I_s / I_n),$$
(3.4)

where $I_s$ and $I_n$ are the skew current and main current, respectively. For example, if we set $I_s = 1$ mA and $I_n = 2.00$ A, the equivalent quadrupole rotation angle is 0.25 mrad. It is a very convenient design, since we only need to set up a small current to the skew PC in order to compensate for a possible mechanical rotation error of the

main quadrupole. This avoids the need for direct mechanical corrections, which would be very difficult in practice.

## 3.2 Skew Quadrupole Field Measurements

In order to characterize the field quality of UMER PC magnets, especially the integrated multipole harmonic components, an accurate rotating coil [15, 16] with a special design has been built and used in the measurement. Compared to many other rotating coils [30] with larger sizes used widely in accelerators, this coil has very small dimensions of only 2.22 cm in width and 12.70 cm in length, as shown in Figure 3.2.
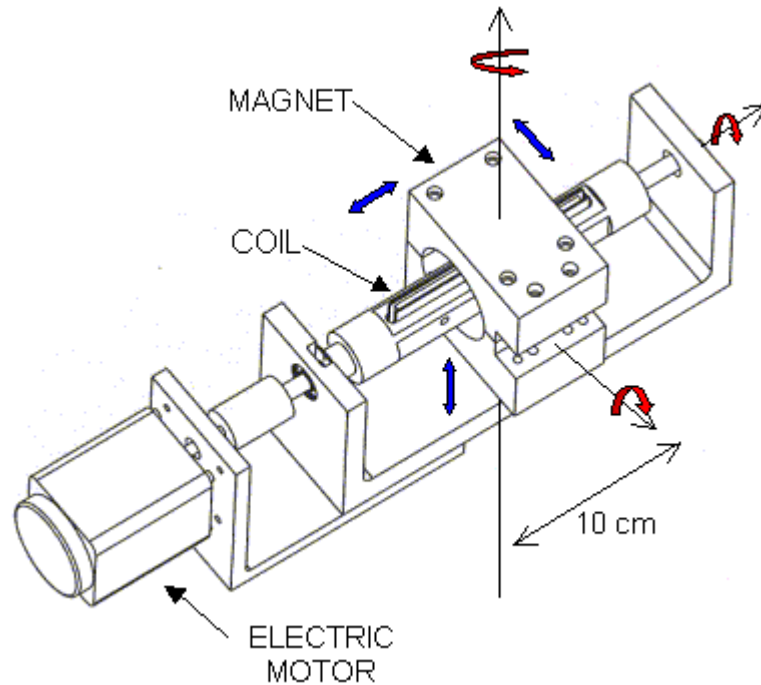


Figure 3.2: Schematic of rotating coil magnetometer.

The rotating coil is arranged in such a way that one side of the coil is positioned along the magnet axis $z$ and driven by an electric motor spinning at $6 \pm 0.001$ Hz along the azimuthal direction $\theta$. Thus, $B_\theta$ is the only relevant field component to be seen by the coil, which contributes to the induced electromotive force (e.m.f) according to Faraday's Law. We use a digital oscilloscope to obtain the voltage waveform and its multipole spectrum. The waveform can also be saved and sent to a computer for more detailed analysis. The oscilloscope is triggered by a synchronous signal produced by a photo chopper. Put in another way, a light from an infrared photo-diode will emerge through a slot along the coil when the coil has a rotation angle of 90 degrees relative to the horizontal plane. The light will trigger a photo-circuit to generate the desired synchronous signal. The field phase or angle information can be determined by the synchronous signal. Figure 3.3 shows a typical quadrupole field signal from the rotating coil.
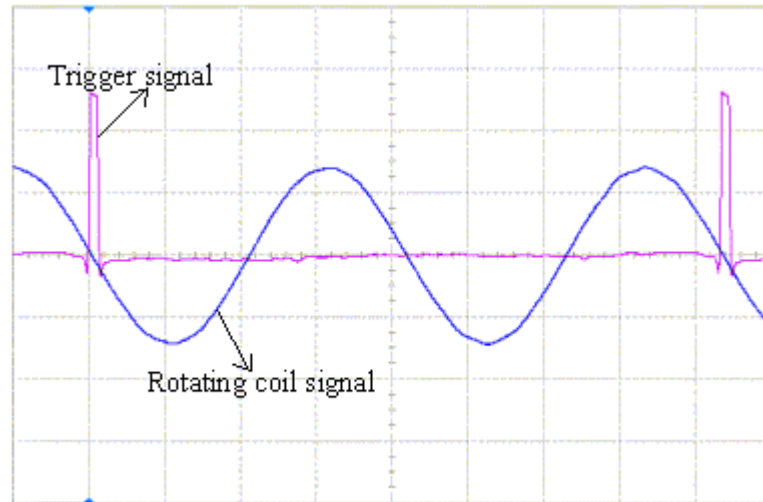


Figure 3.3: Typical quadrupole field signal from the rotating coil.

We have accurately measured the field quality of the main PC quadrupoles with the rotating coil magnetometer. Using the rotating coil apparatus and similar techniques, we have characterized the fields of the new (*main + skew*) quadrupole assembly. We usually supply a large current to the main PC, and very small current to the skew PC in the experiment. The skew quadrupole introduces a phase shift in the observed quasi-sinusoidal induced voltage, which can be measured with high accuracy. Figure 3.4 shows the phase-shift measurements of three skew quadrupole fields with the same normal current ($I_n$ = 2A) but different skew components ($I_s$ = 0, 40, 80 mA). The figure is a blow-up of the measured rotating coil signals around the trigger area. We can observe that the phase shifts increase linearly with the skew currents. It is reasonable for the relatively small skew currents.
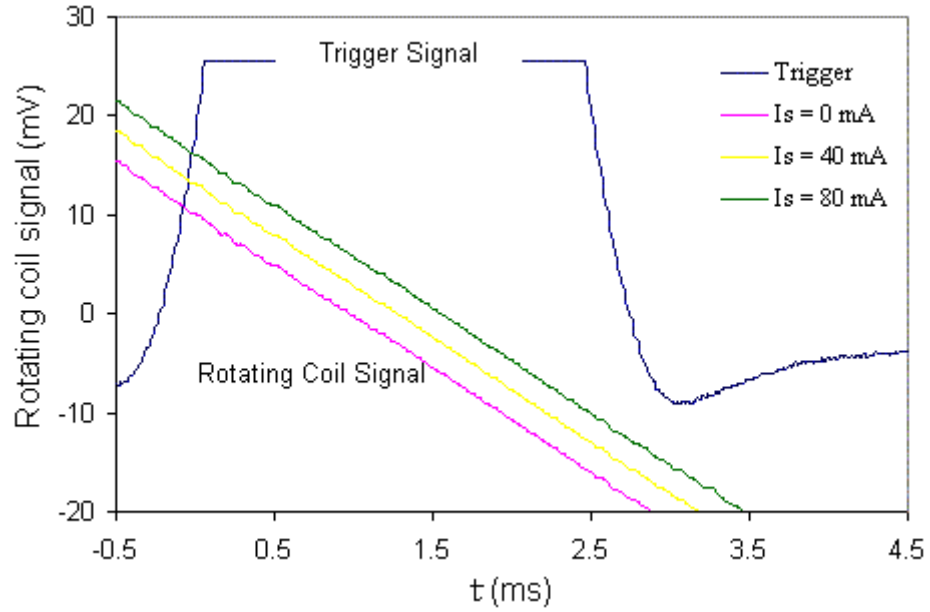


Figure 3.4: Phase-shift measurement of a PC skew quadrupole

Table 3.1 shows the rotation angle (phase-shift) introduced by the skew PCs with currents ranging from 20 mA to 100 mA, corresponding to 1% - 5% of the normal current (2A). The theoretical values for the phase angle are in good agreement with the measurement, except small errors about $0.08^{\circ}$ for some of the measurements, which corresponds to a 5 mA skew current. We believe that this error results from the resolution (~10 mA) of the current supply used in the actual measurement. This also suggests that a current supply of high resolution is required for accurate skew correction.

Table 3.1: Theoretical vs. measured rotation angle of a PC skew quadrupole

| Skew current (mA) | 20 | 40 | 60 | 80 | 100 |
|---|---|---|---|---|---|
| Theoretical rotation angle (deg) | 0.29 | 0.57 | 0.86 | 1.15 | 1.43 |
| Measured rotation angle (deg) | 0.29 | 0.65 | 0.93 | 1.24 | 1.52 |

Table 3.2 shows the measured multipole field amplitudes relative to the main quadrupole components. Measurements of the multipole contents show that the amplitudes of all higher order multipoles (sextupole, octupole, decapole, duodecapole) are smaller than one percent of the main quadrupole component. This is similar to our previous results reported in Ref. [15, 16] for the standard PC quadrupoles. It demonstrates that the new skew quadrupole has a similar field quality as the normal PC quad, and thus can be used in practice.

Table 3.2: Measured multipole field amplitudes (normalized to the main quadrupole component).

| Skew current (mA) | 0 | 20 | 40 | 60 | 80 | 100 |
|---|---|---|---|---|---|---|
| Measured rotation angle (deg) | 0 | 0.29 | 0.65 | 0.93 | 1.24 | 1.52 |
| Dipole | 0.0083 | 0.0076 | 0.0079 | 0.0077 | 0.0078 | 0.0077 |
| Quadruple | 1 | 1 | 1 | 1 | 1 | 1 |
| Sextupole | 0.0049 | 0.0073 | 0.0069 | 0.0072 | 0.0071 | 0.0067 |
| Octupole | 0.0042 | 0.0032 | 0.0035 | 0.0029 | 0.0029 | 0.0026 |
| Decapole | 0.0017 | 0.0019 | 0.0022 | 0.0021 | 0.0022 | 0.0019 |
| Duodecapole | 0.0018 | 0.0023 | 0.0022 | 0.0025 | 0.0026 | 0.0024 |

## 3.3 Skew Quadrupole Testing in the Injector Line

We performed preliminary tests [14] of the skew quadrupole in the UMER injector line. Figure 3.5 is a photo of the real injector line where the experiments were conducted. The straight part of the injector line has four quadrupoles that we label as "Q1" through "Q4". The quadrupole halves are clamped to a common plate (flat to within 0.01 mm), so the rotation errors from mounting are minimized. In fact, the beam rotations that are observed in the matching experiments are small, and may be the result of residual errors from assembly of the printed circuits on the aluminum mounts. In UMER, however, the relative rotations of groups of quadrupoles, each group (2 FODO periods each) sharing a support plate, may be more problematic.
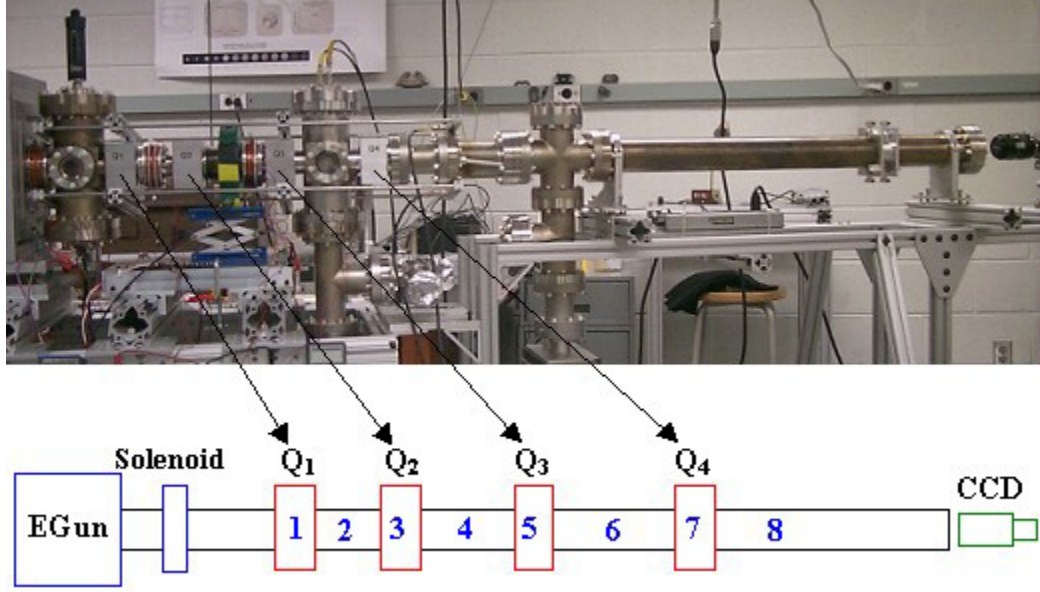
Figure 3.5: Injector line layout: $Q_1$ to $Q_4$ are quadrupoles; the long tube after location "8" contains a movable phosphor screen for taking beam pictures.

Therefore, in order to gain a better understanding of the effects of rotated quadrupoles in UMER, and to explore general issues of beam transport dynamics with rotation errors, we designed a controlled experiment. The first quadrupole, Q1, is fitted with a skew quadrupole as in Fig. 3.1. The normal current of the main quadrupole is 1.545A. The skew quadrupole current is varied from 0.1A to 0.4A, corresponding to rotation errors from $1.86^{o}$ to $7.50^{o}$. Simultaneously, the main currents are also reduced from 1.545A to 1.492A to keep the amplitude of the net quadrupole field constant. These experimental current setups are illustrated in table 3.3.

Table 3.3: Equivalent quadrupole rotation angles.

| Skew Current $I_s$ (A) | Normal Current $I_n$ (A) | Rotation Angle $\alpha$ |
|---|---|---|
| 0.1 | 1.542 | $1.86^o$ |
| 0.2 | 1.532 | $3.72^o$ |
| 0.3 | 1.516 | $5.60^o$ |
| 0.4 | 1.492 | $7.50^o$ |

The beam we used in this experiment was an electron beam of I = 100 mA, E = 10 keV and $\varepsilon \approx 60$ mm·mrad. It is the most intense beam in UMER. Figure 3.6(a) shows fluorescent screen pictures taken along the injector line, corresponding to the locations from 1 to 8 in Fig. 3.5. The skew and main currents are 0.2A and 1.532A, respectively. This current setup yields a $3.72^o$ rotation angle of the quadrupole field in Q1. In Fig. 3.6(a) some of the beams appear truncated because of a limited phosphor screen size.

For comparison, simulated beam pictures, based on the particle-in-cell (PIC) code WARP [31], are shown in Fig. 3.6(b). We used 320k macro-particles and 256×256 grids for the Poisson solver. The initial particle distribution is assumed to be Semi-Gaussian (S.G.), i.e. a distribution with uniform particle density in space but a Gaussian profile in the transverse velocity. As seen in the figure, the pictures show good agreement regarding beam rotations and shapes, despite some differences between the particle distributions.

(a)

1cm

(b)

Q1(z=38cm)     Q2(z=52cm)     Q3(z=71cm)     Q4 (z=91cm)
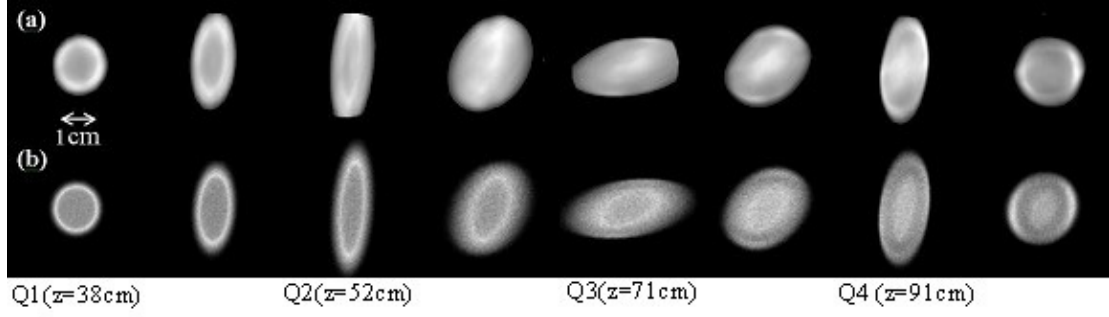
Figure 3.6: Effects of rotated first quadrupole Q1 in UMER injector: (a) Phosphor screen pictures, and (b) WARP simulations. The quadrupole field of Q1 is rotated $3.72^{\circ}$ by using a skew current of 0.2A.

The rotation angles of the beam cross sections along the injector line can be expressed in terms of second order moments of the electron distributions. For the simulation and experimental photos, we use the following formula [27]:

$$\tan 2\alpha = \frac{2\Delta xy}{\Delta x^2 - \Delta y^2},$$
(3.5)

where $\Delta xy = <xy> - <x><y>$ and $<>$ indicates average over particles.

Figures 3.7 show results of experiments vs. simulations for the same locations as Fig 3.6. Good agreement between simulations and experiment is seen. At Q2, the beam has rotated by $3.8^{\circ}$ (Fig. 3.6 and solid curve in Fig.3.7b), almost the same as the rotation error in Q1. At Q3, the beam rotation angle is about $9.7^{\circ}$ relative to the horizontal (un-rotated) orientation, while at Q4 almost the same angle is measured relative to the vertical. Similar considerations apply for the other skew currents. We also notice a few discrepancies existing between the experiments and simulations (e.g. Fig. 3.7a, 0.1A), which mostly occur for small rotation angles. This may come from the difficulties in measuring small angles when the beam density pictures have

noises. Also, the discrepancies may actually result from the different density distributions between experiments and simulations, which would have a bigger impact on the calculations using Eq. 3.5 when the angles are small. This effect can be seen clearly from the beam density pictures in the location between Q2 and Q3 as shown in Fig. 3.6 (or location "4" in Fig. 3.5).
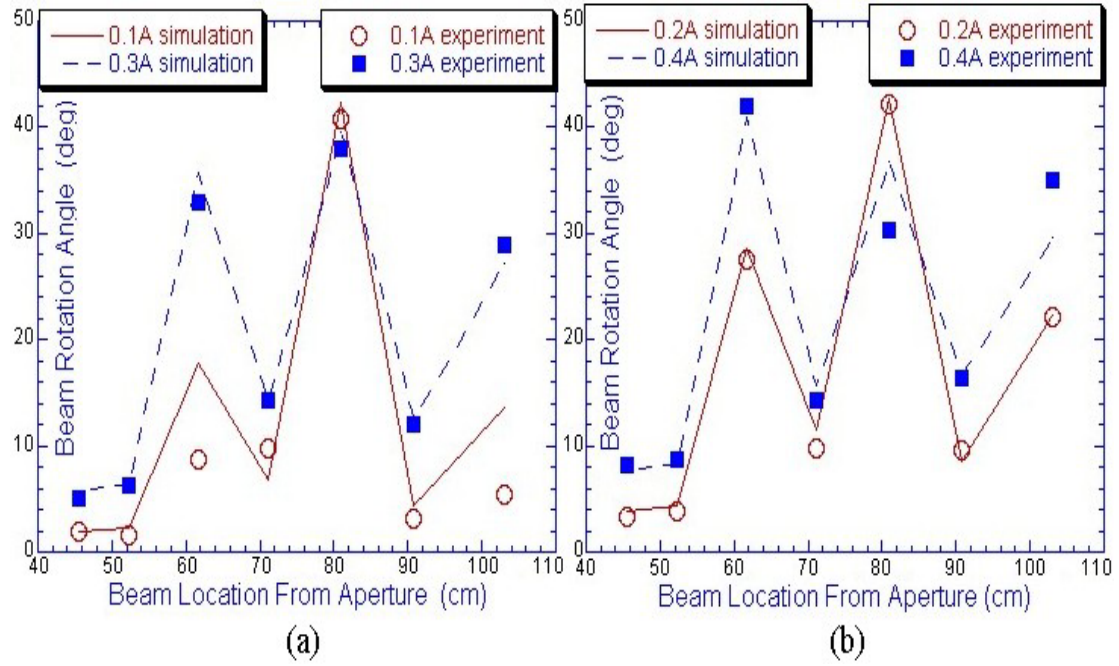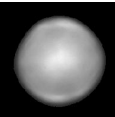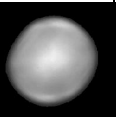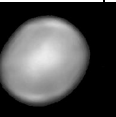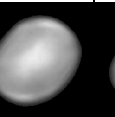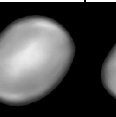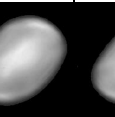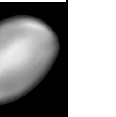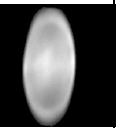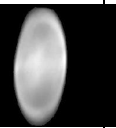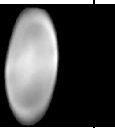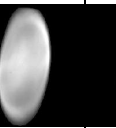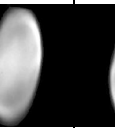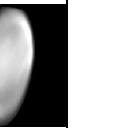


Figure 3.7: Beam rotation angle along injector: experiment vs. simulation. (a) Skew Currents = 0.1 and 0.3 A; (b) Skew Currents = 0.2 and 0.4 A.

Table 3.4 shows fluorescent screen pictures taken at two locations ("6" and "7" in Fig. 3.5) of the injector line as a function of skew angle in Q1. The beam rotation can be seen clearly, which gives us an impression of how the beam quality deteriorates due to the quadrupole rotation.

Table 3.4: beam rotations caused by rotating Q1

| $Q_1$Rotation angle | 0° | 0.93° | 1.86° | 2.79° | 3.72° | 4.66° | 5.60° |
|---|---|---|---|---|---|---|---|
| Beam pictures are taken at the location between $Q_3$ & $Q_4$ | | | | | | | |
| Beam pictures are taken at the location of $Q_4$ | | | | | | | |

## 3.4 Beam Rotation Correction in the Ring Lattice

We have observed severe beam rotations in the beam transport experiment in the UMER ring lattice. Figure 3.8 plots the measured beam rotation angles for a 24 mA, 10 keV electron beam in the first twelve ring chambers of UMER, without any skew correction. The beam density picture used for the calculation was taken at the phosphor screen location for each chamber, which is placed 2.7 cm away from the chamber center, so the cross-section of a matched beam would be elliptical, and suitable for the angle calculations.
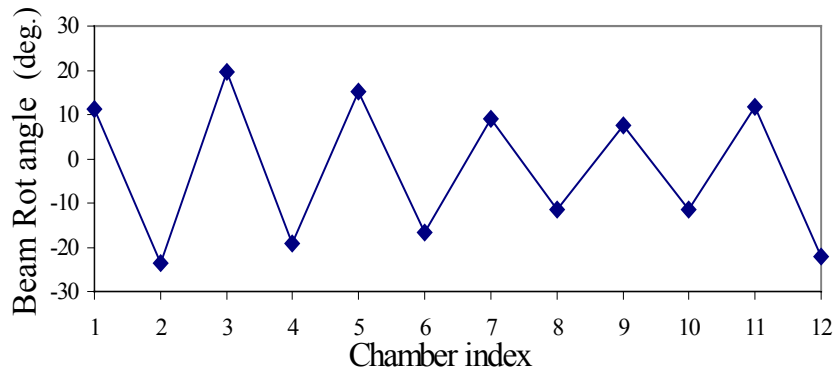


Figure 3.8: Beam (24mA, 10 keV) rotation angles with no skew correction

49

Since there is no obvious beam rotation observed in the diagnostic chamber (IC2) in the middle of the injector, we believe that the initial beam rotation (at the first ring chamber RC1) must result from either quadrupole rotations or field distortions in the latter part of the injector. Therefore, we decided to add a skew corrector to the quadrupole upstream of the injection dipole. In order to determine the optimal current $I_s$ for the skew corrector, we measured the changes of beam rotation angles corresponding to small skew currents varying from 0 to 0.2A in all the 12 ring chambers. Figure 3.9 demonstrates two of such examples at chamber RC1 and RC2. For each measurement, a linear regression yielded the best estimates of both $\Delta\alpha/\Delta I_s$ and $\alpha_0$ by the fitted slope and the interception, where $\Delta\alpha/\Delta I_s$ is the change of rotation angle corresponding to the skew current change, and $\alpha_0$ the rotation angle at $I_s = 0A$. Table 3.5 illustrates the measurement results from RC1 to RC12. $\alpha_m$ is the beam rotation angle from the direct measurement (see Fig. 3.8), which is very close to $\alpha_0$ from the linear regression.
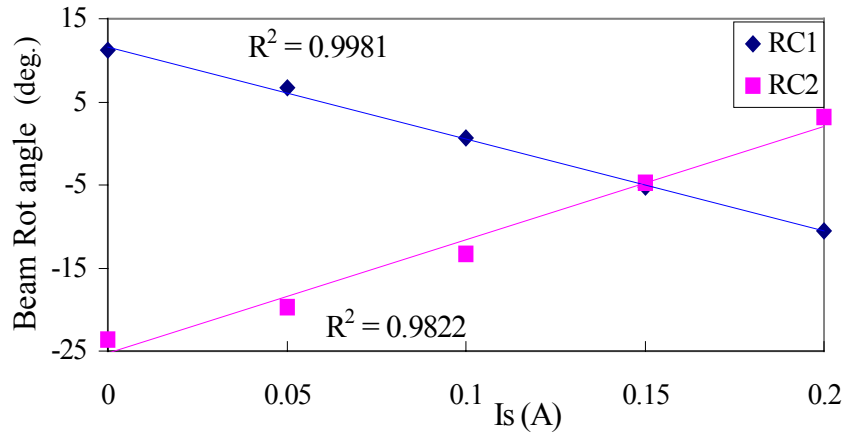


Figure 3.9: Beam rotation angle changes corresponding to the skew currents for a 24 mA, 10 keV electron beam in ring chambers RC1 and RC2.

Table 3.5: Beam rotation measurement at RC1 to RC12

| | $\alpha_m$ (deg.) | $\alpha_0$ (deg.) | $\Delta\alpha/\Delta I_s$ (deg./A) | $R^2$ |
|------|--------|--------|---------|--------|
| RC1 | 11.18 | 11.62 | -110.67 | 0.9981 |
| RC2 | -23.58 | -25.31 | 136.74 | 0.9822 |
| RC3 | 19.60 | 20.45 | -181.28 | 0.9961 |
| RC4 | -19.23 | -20.08 | 118.28 | 0.9942 |
| RC5 | 15.07 | 15.57 | -148.54 | 0.9981 |
| RC6 | -16.79 | -17.59 | 119.84 | 0.9951 |
| RC7 | 9.02 | 9.03 | -119.76 | 0.9983 |
| RC8 | -11.52 | -11.60 | 92.06 | 0.9985 |
| RC9 | 7.57 | 7.58 | -93.91 | 0.9998 |
| RC10 | -11.50 | -12.22 | 80.36 | 0.9885 |
| RC11 | 11.77 | 12.09 | -68.91 | 0.9937 |
| RC12 | -22.04 | -24.06 | 127.28 | 0.9489 |

From the above table, we found that the beam rotation angle $\alpha$ has a linear relation with the skew current $I_s$ in all the chambers i.e. $\alpha = \alpha_0 + (\Delta\alpha/\Delta I_s) \cdot I_s$. We therefore can minimize $\alpha$ for all the chambers in the least square sense, which yields the optimal skew current $I_s \approx 0.13$A (normal current $I_n = 1.88$A). Figure 3.10(a) and 3.10(b) show the fluorescent screen pictures before the skew correction and after the correction, respectively. A significant improvement can be seen in this case: the standard deviation of the rotation angles is reduced from $16.2^o$ to $3.8^o$ after the correction. The corresponding beam rotation angles before and after the correction are also plotted together in Figure 3.11.
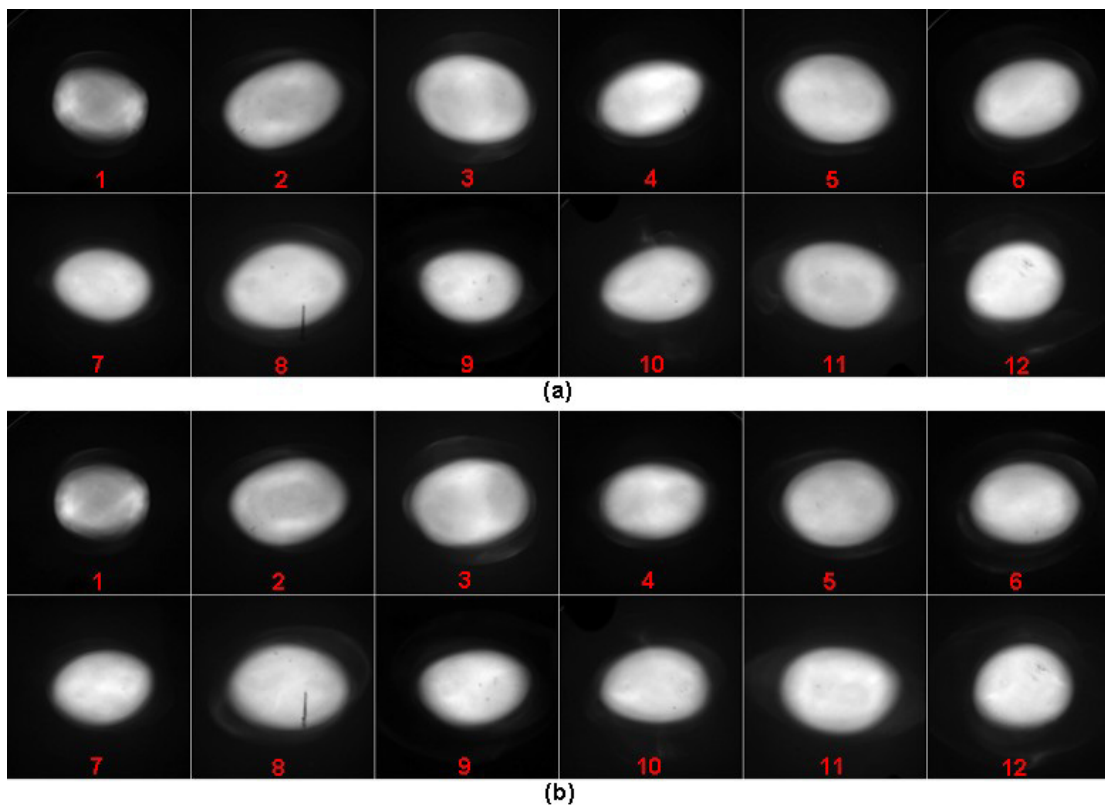
Figure 3.10: Beam cross-section pictures for a 24 mA, 10 keV electron beam at ring chambers RC1 to RC12 before skew correction (a) and after correction (b).
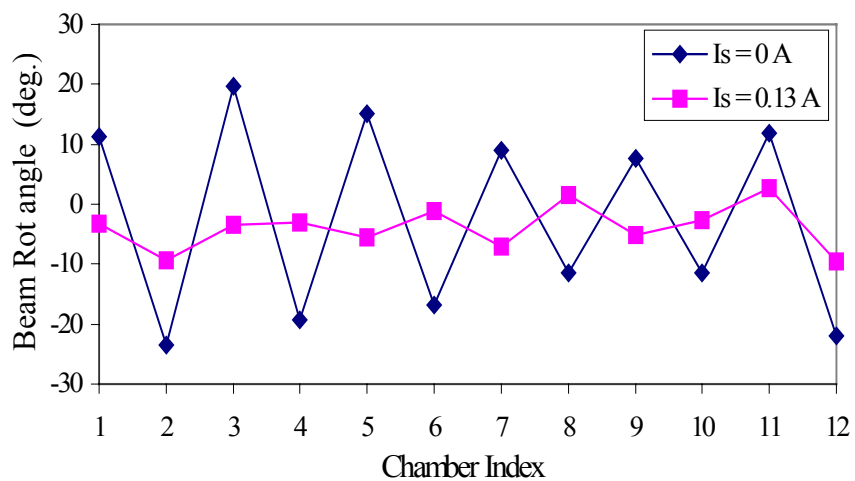


Figure 3.11: Beam rotation angles for a 24 mA, 10 keV electron beam at ring chambers RC1 to RC12 before skew correction and after correction.

The mechanical skew errors of the UMER quadrupoles can be controlled within $0.06^{\circ}$ (about 1 mrad). However, the induced quadrupole rotation angle $\alpha$, for $I_s$ = 0.13A and $I_n$ = 1.880A, is $1.98^{\circ}$ from Eq. 3.4. Thus, the initial beam rotation at RC1 must result from accumulated effects of several (up to seven) quadrupoles' rotation errors, and from field distortions caused by slightly magnetized pipe sections around welds. The latter effect refers to the introduction of skewness to the main quadrupole field, especially at large radii near welds. This is made evident by the fact that the beam rotations of our lowest current beams, 0.6 mA and 7 mA (beam radii 5% and 12% of the vacuum pipe radius, respectively) are not so severe when compared to the 24 mA case (beam radius 20% of pipe radius).

# Chapter 4 Beam Matching

Maintaining a matched beam (e.g. keeping constant beam size through a uniform focusing channel) is a fundamental requirement for the transport of intense beams over long distances. Both theoretical and simulation studies [32, 33] have identified that beam mismatch is a major source for emittance growth and halo formation. A mismatched beam is one that lacks the average force balance between the external focusing force and the internal forces from the space charge and the emittance due, for example, to the injection of a beam with the "wrong" size. This situation results in periodic oscillations in beam size, the frequency of which has been derived [34]. Resonance between a particle's betatron oscillation and these envelope oscillations will drive some particles to larger radii and finally lead to particle losses. This has been verified by computer simulation [33] and the "particle-core" model [35]. In UMER, the extreme high intensities and compact features require us to design the beam optics carefully. The major topic of this chapter is the important challenge of matching the intense electron beam from the electron gun through the injector into the ring lattice. Although in the past we have relied on calculations using the envelope equations to determine magnet settings for matching, this method has not been reliable and produced errors in beam size of about 10%. The problem is that lack of knowledge about accurate ring-lattice modeling and optimum matching-section setting may result in a discrepancy between experiment and theory. In addition, on-line adjustment of magnet strengths around the design values is especially important from an experimental point of view, which is another topic in the

chapter. We organize our studies in the following order: beam physics background, ring lattice design, matching section design, and empirical beam matching.

## 4.1 Beam Physics Background

UMER consists of a series of magnetic quadrupoles, with strength $\kappa_x = -\kappa_y = qG/m\gamma\beta c$, where $G = G(s)$ is the quadrupole field gradient; $q$, $m$ and $c$ are the particle charge, mass and light speed, respectively. In practice, it is common to model the quadrupole by a "hard-edge" element with an effective length defined by $l_{eff} = 1/\kappa_{peak} \cdot \int_{-\infty}^{+\infty} \kappa(z, r = 0)dz$. Typical smooth and "hard-edge" gradient profiles of a unit FODO cell are shown in Figure 4.1. We normally use "hard-edge" magnets in envelope and matrix codes to do first-order calculations. The advantage of "hard-edge" magnets resides in their easier implementation in the codes and theoretical analysis.
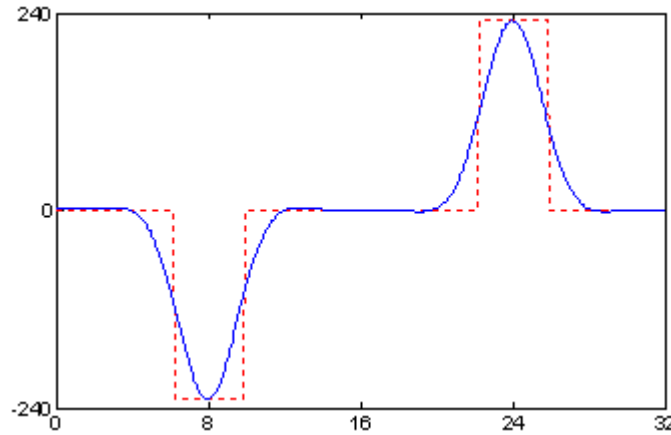


Figure 4.1: Real quadrupole profile vs. "hard-edge"

Based on the "hard-edge" quadrupole model and the standard transfer matrices for quadrupoles and drifts, the peak focusing strength of quadrupoles in a FODO cell for a given zero-current phase advance per period ($\sigma_0$) can be calculated from [36]

$$\cos \sigma_0 = \cos \theta \cosh \theta + \frac{L}{l} \theta (\cos \theta \sinh \theta - \sin \theta \cosh \theta) - \frac{1}{2} (\frac{L}{l})^2 \theta^2 \sin \theta \sinh \theta$$

(4.1)

where $\theta = \kappa^{1/2} l$; $l$ is the effective length of the quadrupole; $L$ is the drift space between adjacent quadrupoles. In UMER, we normally have $\sigma_0 = 76^o$ and $l = 3.64$ cm; $L$ is equal to the half FODO length minus $l$, i.e. 12.36 cm. Thus, the calculated quadrupole strength $\kappa$ is 229.6 m$^{-2}$, which corresponds to 7.78 G/cm or 1.88 A for the quadrupole current (4.14G/cm·A).

In the ring lattice of UMER, we essentially apply $\kappa = \pm 229.6$ m$^{-2}$ ($\sigma_0 = 76^o$) with alternating gradients for all the beam currents (see Table 1.2). With the presence of the space-charge forces, the depressed phase advances ($\sigma$) per period from the smooth approximation [8] are 12.3$^o$, 23.8$^o$, 35.4$^o$, 62.5$^o$ for beam currents of 100mA, 24mA, 7mA, 0.6mA, respectively, and hence the tune depressions ($\sigma/\sigma_0$) are 0.162, 0.313, 0.466, and 0.823. By varying the electron beam current (and emittance), UMER can operate in a very wide physics regime.

In order to understand the physics characteristics of space-charge-dominated beams, the 2-D rms envelope equations [6] are important, which have identical form as the K-V envelope equations [7]. In UMER, the beam bunch (10keV, 100ns) has a radius in the range of 10 mm or less depending on the beam current and focusing

strength. Since the bunch length is about 6 m, the beam can be considered as a 2-D beam, except for the edge effects. Thus, the beam transport is governed by the 2-D rms envelope equations [6]:

$$X'' + \kappa_x X - \frac{2K}{X+Y} - \frac{\varepsilon_x^2}{X^3} = 0 , \tag{4.2a}$$

$$Y'' + \kappa_y Y - \frac{2K}{X+Y} - \frac{\varepsilon_y^2}{Y^3} = 0 . \tag{4.2b}$$

Here $X$ and $Y$ are the 2×rms beam radii in the two planes perpendicular to the propagation direction, and $X''$ and $Y''$ represent the second derivatives of $X$ and $Y$ along the focusing channel. Further, $K = (I/I_0) \cdot (2/\beta^3\gamma^3)$ is the generalized dimensionless perveance with the characteristic current $I_0 = 4\pi\varepsilon_0 mc^3 / q \approx 17 kA$ for electrons, and $\kappa_x(s)$ and $\kappa_y(s)$ are the external focusing functions. The last terms in Eqs. (4.2a) and (4.2b) contain the effective (4×rms, unnormalized) emittances $\varepsilon_x$ and $\varepsilon_y$. Correspondingly, the equations of motion including the linear space-charge forces for a single particle are

$$x'' + \left( \kappa_x - \frac{2K}{X(X+Y)} \right) \cdot x = 0 , \tag{4.3a}$$

$$y'' + \left( \kappa_y - \frac{2K}{Y(X+Y)} \right) \cdot y = 0 . \tag{4.3b}$$

The 2D rms envelope equations are very important in the optics design and matching of intense space-charge-dominated beams. They describe the evolution of beam envelopes, and usually agree quite well with the experimental observations. The inaccuracy mostly comes from the uncertainties associated with the values of initial

beam sizes, slopes, perveance and emittances, which are the key parameters for the integration of Eqs. (4.2a) and (4.2b). The boundary conditions (or image charge effects) and the changes of emittances are not included here either. Regardless of these insufficiencies, the rms envelope equations generally yield a good starting point.

A more realistic calculation can be done with accurate 3D fields for the magnets in a PIC code. To generate these fields along the beam line, we developed a new air-core magnetic field solver, MAGLI [37]. The code can model the printed-circuit magnets by up to 18 million conductor segments in a one-gigabyte memory space. The typical PIC code that we are using is WARP [31]. It can track multi-million particles self-consistently with realistic distributions in a reasonable amount of time.

## 4.2 Ring Lattice Design

There are two key issues important to the ring lattice design in UMER. The first one is how to calculate the peak focusing strengths of quadrupoles in a unit FODO cell for the required operation point at $\sigma_{0x} = \sigma_{0y} = 76^{\circ}$. We have illustrated a simple model of two "hard-edge" quadrupoles in a straight line (see Fig. 4.1) in the previous discussion. In this case, a simple matrix calculation yields $\kappa_{x1} = -\kappa_{x2} = -229.6$ m$^{-2}$ (7.78 G/cm) for the two quadrupoles. If smooth gradient profiles in a straight section are employed, the matrix approach is still possible if the profiles are modeled by the superposition of many "hard-edge" sub-elements. The second issue is how to achieve periodic envelope matching in a FODO cell for the quadrupole

strengths as stated above. Figure 4.2 shows periodic matched solutions for two typical UMER beams (100mA, 60mm·mrad and 24mA, 30mm·mrad) with "hard-edge" quadrupoles ($\kappa_{x1} = -\kappa_{x2} = -229.6$ m$^{-2}$) in a straight section. We obtain the solutions by iteratively integrating the rms envelope equations from $z = 0$ to $z = 32$cm in a FODO cell. The convergence is achieved once the beam radii and slopes at the two boundaries are equal.
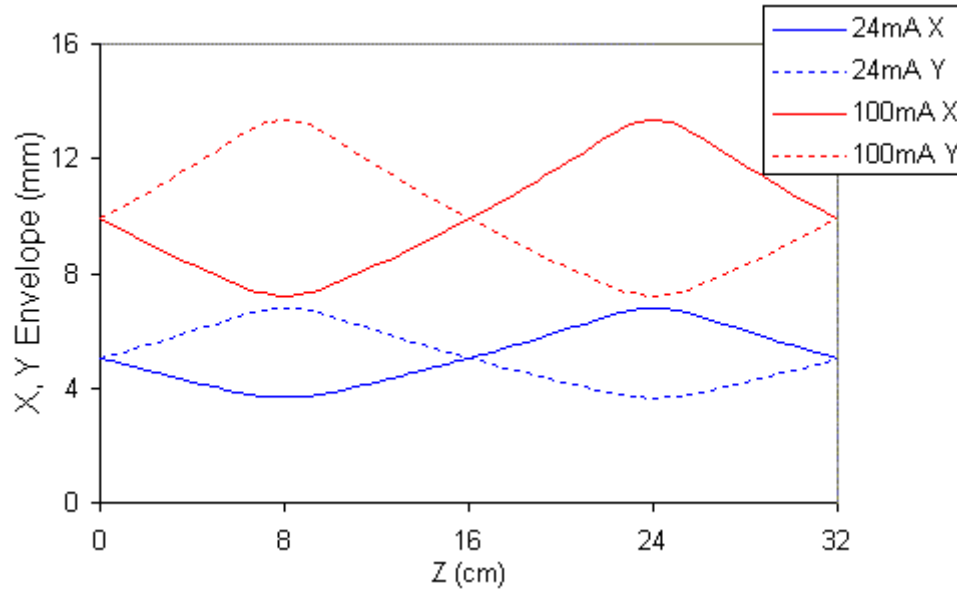


Figure 4.2: Matched beam envelopes in a FODO cell from rms envelope equations.

In obtaining the solutions of Fig. 4.2, we have made two assumptions: (1) quadrupoles are "hard-edged"; (2) The FODO period is in a straight section and the effect of a bending dipole is ignored. However, it is instructive to compare the results of using a PIC code with the full 3D fields for both quadrupoles and dipoles with the quadrupole peak strengths at $\kappa_{x1} = -\kappa_{x2} = -229.6$ m$^{-2}$. Figures 4.3 shows the matched

results of such a simulation. It was done by the WARP-PIC slice code with an initial

KV distribution, 20k macro particles, and 1mm×1mm grid-size for the pre-calculated

3D magnetic fields along the path. The figure illustrates two periodic solutions for

two UMER beams (100mA and 24mA), but also reveals a 6% difference between $X$

and $Y$ envelope peaks. This is clearly due to the unequal $\sigma_{0x}$ and $\sigma_{0y}$ in the two

transverse directions. This asymmetry must result from the effect of dipoles, which

has been taken into account by the above PIC simulation, but not by the envelope

equations.
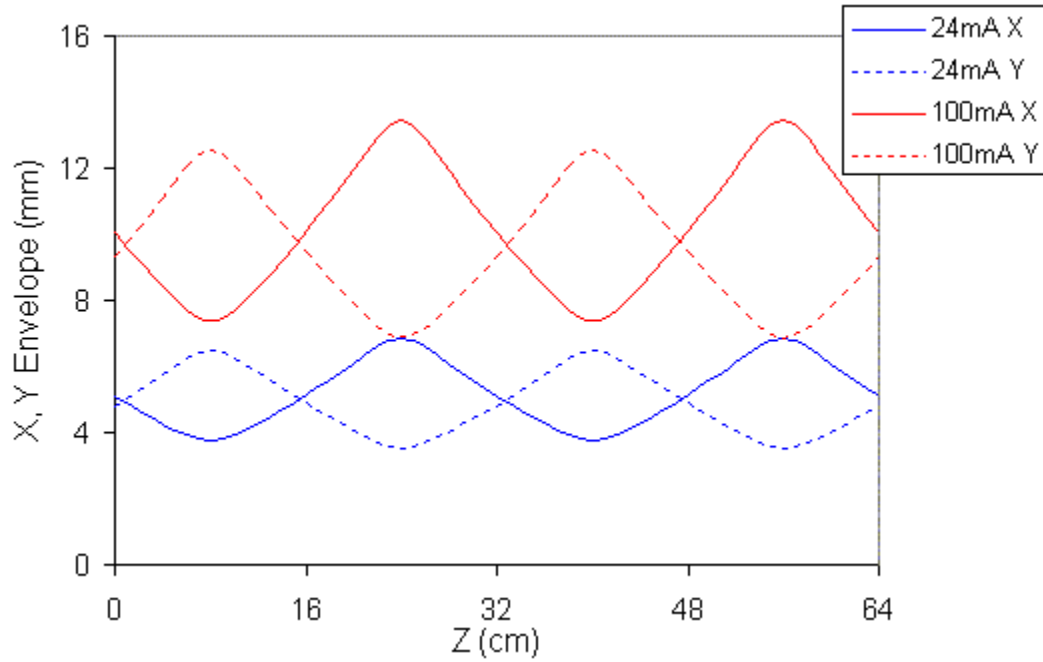


Figure 4.3: Matched beam envelopes in a FODO cell from WARP-PIC code

In order to calculate the actual $\sigma_{0x}$ and $\sigma_{0y}$ for the above ring lattice, we

employ the WARP code to track the centroid of thousands of particles (without space

charge) for several turns through the 3D fields. During the process of particle tracking, we need to either turn off the Poisson solver to exclude the space-charge fields or reduce the beam current to near zero, since we aim to calculate the particle oscillation frequencies for the zero-current. The phase advance $\sigma_0$ is identified as the main peak frequency of the Fourier spectrum of the centroid data. The main frequency can be accurately determined with an interpolated-FFT technique [38] by interpolating the shape of the Fourier spectrum around the main peak. This avoids tracking particles for a large number of turns to achieve a high resolution of the main frequency.

For the ring lattice (including the dipoles) with the peak focusing strengths $\kappa_{x1}$ $= -\kappa_{x2} = -229.6$ m$^{-2}$, the zero-current phase advances per cell are $\sigma_{0x} \approx 76.4^{\circ}$ and $\sigma_{0y} \approx$ 79.3$^{\circ}$ from the above simulation. Since the focusing and defocusing strengths of quadrupoles are equal for this case, the slight asymmetry must result from the small focusing effect of the bending dipoles. Although the UMER dipole has a non-uniform distribution along the bending path ($z$) and the radial direction ($x$), it can be treated as a "hard-edged" sector dipole with a field index $n \approx 0.72$ [39] and an effective length $l_d$ $\approx 3.85$ cm. The field index $n$ is calculated by [40]

$$ n = -\frac{r_0}{B_{y-\text{int}}(x=0)} \cdot \frac{\partial B_{y-\text{int}}(x)}{\partial x}. \tag{4.4} $$

Here $B_{y-int}$ is the integrated dipole field $B_y$ along the orbit $z$ defined by the actual bending pipe; $r_0 = s/\alpha \approx 25.24$ cm is the equilibrium radius; $s \approx 4.406$ cm is the length of the mechanical bend; $\alpha = 10^{\circ}$ is the bending angle. The dipole focusing functions can be expressed in terms of $n$ and $r_0$ as [40]

$$\kappa_{dx} = (1-n)/r_0^2, \qquad\qquad\qquad (4.5a)$$

and

$$\kappa_{dy} = n/r_0^2. \qquad\qquad\qquad (4.5b)$$

Since $0<n<1$, the dipole induces focusing in both the horizontal and the vertical planes, i.e. $\kappa_{dx} \approx 4.4$ m$^{-2}$ for $x$ and $\kappa_{dy} \approx 11.3$ m$^{-2}$ for $y$ over an effective distance of 3.85 cm. These strengths are asymmetric in the two directions. That is why the peaks in the $X, Y$ envelope in Fig. 4.3 are different.

With this dipole model, the FODO cell can be represented by two "hard-edge" quadrupoles plus a small "hard-edge" element with focusing functions $\kappa_{dx}$ and $\kappa_{dy}$ in the middle. Figure 4.4 illustrates this model in detail. In order to test its accuracy, we first use the transfer matrices to calculate the zero-current phase advances per cell. For $\kappa_{x1} = -\kappa_{x2} = -229.6$ m$^{-2}$, it yields $\sigma_{0x} \approx 77.3^\circ$ and $\sigma_{0y} \approx 79.4^\circ$, which is very close to the previous results ($\sigma_{0x} \approx 76.4^\circ$ and $\sigma_{0y} \approx 79.3^\circ$) obtained from the interpolated FFT of the particle centroid tracking. Second, we can calculate the periodic matched solutions via rms envelope equations including the dipole model. The results are plotted in Figure 4.5, where the solid and dashed curves are the $X$ and $Y$ envelopes, respectively, for a 100mA beam from the rms envelope equations with the dipole focusing; the dots are the previous results (see Fig. 4.3) from the WARP-PIC simulations with realistic 3D magnetic fields. The new FODO model agrees very well with the PIC simulations.
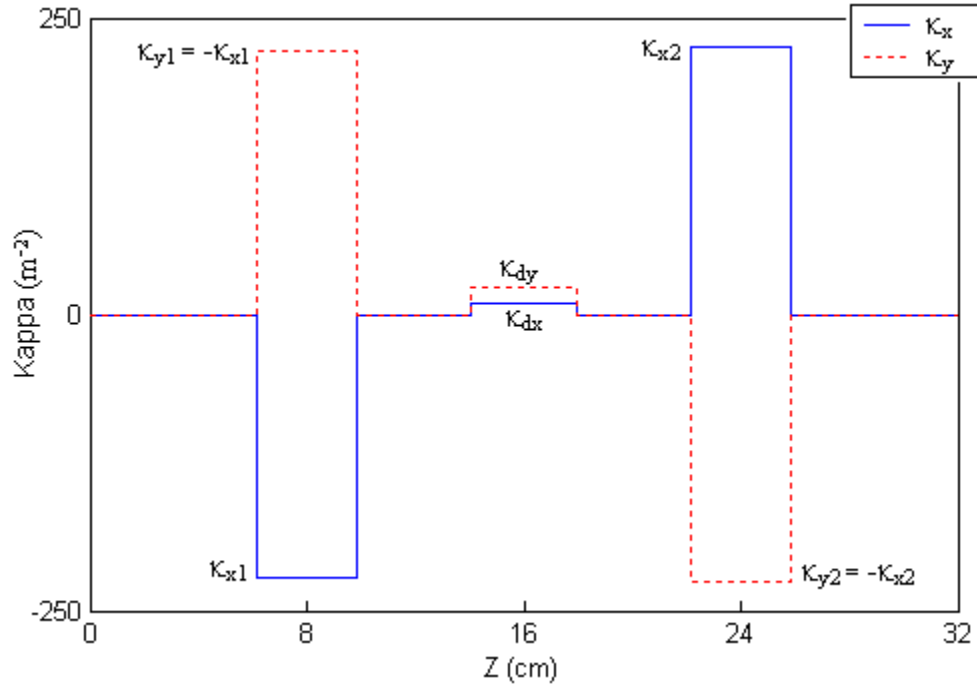
Figure 4.4: FODO model including a dipole: $\kappa_{dx}$ and $\kappa_{dy}$ are the focusing strengths of the dipole in the *x* and *y* directions, respectively.
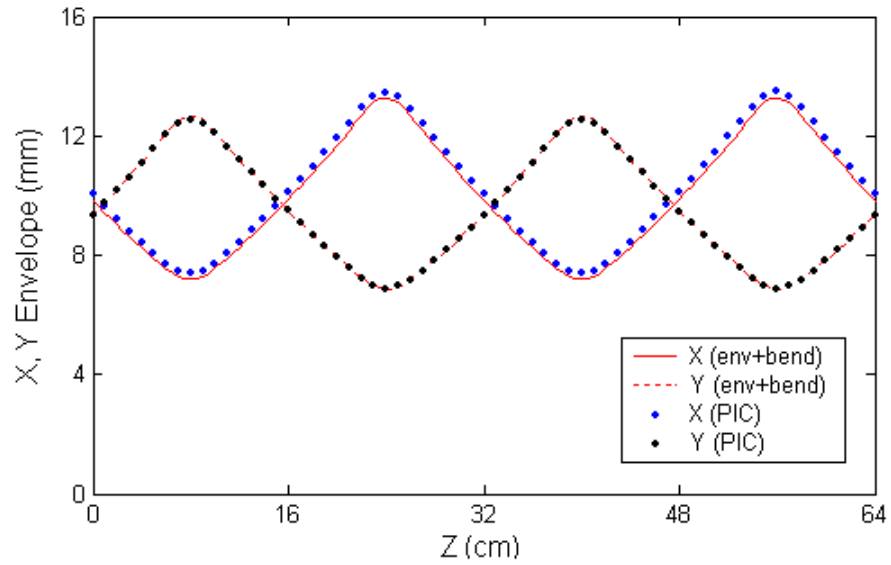


Figure 4.5: *X, Y* envelopes from the envelope equation (new FODO model with dipoles) compared to the WARP PIC simulation (full 3-D fields) for a 100 mA beam. The peak focusing strengths for both cases are $\kappa_{x1} = -\kappa_{x2} = -229.6$ m$^{-2}$.

To have a symmetric focusing channel, we need to make $\kappa_{x1}$ and $\kappa_{x2}$ slightly different to compensate for the dipole's focusing. Using the new model, we can very easily obtain them via the transfer matrices of a FODO cell. We found that $\kappa_{x1}$ = –221.8 m$^{-2}$ and $\kappa_{x2}$ = 225.0 m$^{-2}$ gave us the desired phase advances at $\sigma_{0x} = \sigma_{0y} = 76^o$. With these $\kappa_{x1}$ and $\kappa_{x2}$, we can solve the periodic matched solutions either by the rms envelope equations or the PIC code. The results from the two methods are plotted in Figure 4.6. A direct observation from the figure is that the $X$ and $Y$ envelope peak are about the same in contrast with Fig. 4.5 where $\sigma_{0x}$ and $\sigma_{0y}$ are unequal. Besides, the good agreement between the two methods demonstrates that the envelope code with the dipole model can be used in practice. In fact, for matching purposes, we always prefer the envelope equations to the PIC method, because the latter would take several magnitudes of computing power over the former. The PIC code, e.g. WARP, is usually used to confirm or refine the results after the initial matching is done by the envelope code.
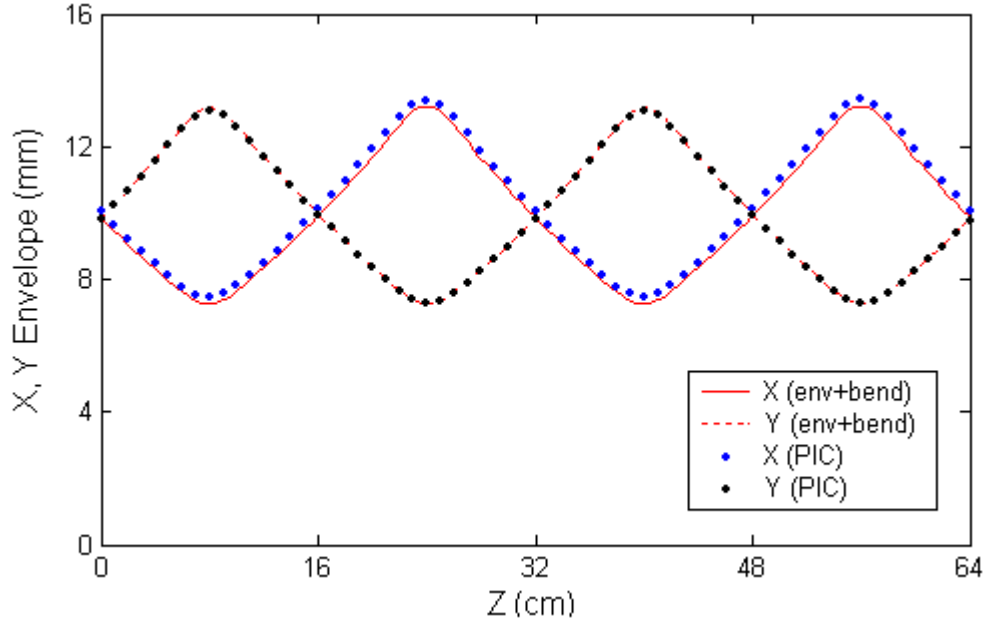
Figure 4.6: *X, Y* envelopes from the envelope equation (new FODO model with dipoles) compared to the WARP PIC simulation (full 3-D fields) for a 100 mA beam. The peak focusing strengths for both cases are $\kappa_{x1} = -221.8$ m$^{-2}$, $\kappa_{x2} = 225.0$ m$^{-2}$.

## 4.3 Matching Section Design

Figure 4.7(a) shows the *present* geometric layout of the UMER matching section/injector and the first ring section, where Sol is a solenoid; Q1 to Q6, PQ, are quadrupoles; QR1 to QR5 are ring quadrupoles; D0, D1 and D2 are ring dipoles. This layout reflects a simple implementation of the UMER injection for the first turn operation before the ring is physically closed. For multi-turn operation, however, PQ and QR1 must be replaced with specially designed quadrupoles due to the geometric requirements (see Chap. 5). Although the matching section design we describe here is intended for the first turn, it does not lose generality for multi-turn operation.

(a)



(b)
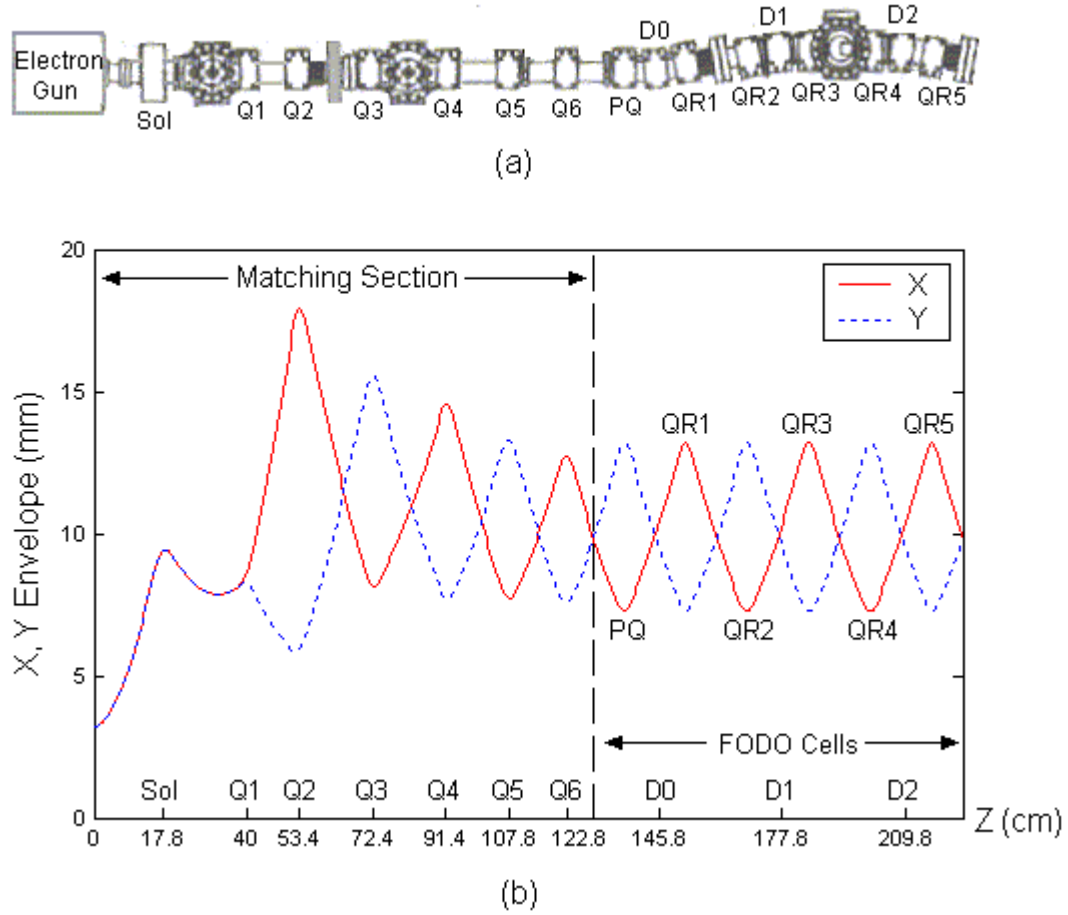
Figure 4.7: Injector layout and a matched solution: (a) Injector layout for the first turn operation; (b) a matched solution.

The UMER matching section consists of a solenoid and six quadrupoles (Sol, Q1 to Q6) distributed over a distance of 1.3 m, approximately. We aim to inject the beam into the ring with the desired beam radii and slopes ($X_R$, $Y_R$, $X_R'$, $Y_R'$), as dictated by the results of periodic FODO matching (previous section). Figure 4.7(b) shows such a matched solution for the 100 mA beam (10 keV and 60 mm·mrad). The dashed line in the figure divides the beam line into two regions: the aperiodic matching

section and the periodic FODO cells. The position of the dashed line is called the matching point. It is the end of the matching section ($z = 129.82$ cm) and also the start of the first FODO cell (PQ, D0, QR1) in the ring. If we employ the FODO model including the bend shown in Fig. 4.4, the beam radii and slopes $(X_m, Y_m, X'_m, Y'_m)$ for the 100 mA beam at the matching point have the values, 9.85mm, 9.82mm, −0.0418, and 0.0416, respectively, as required by $\sigma_{0x} = \sigma_{0y} = 76^o$ or $\kappa_{x1} = $ -221.8 m$^{-2}$ and $\kappa_{x2} = $ 225.0 m$^{-2}$. Mathematically, the matching section has seven adjustable parameters $\overline{\kappa} = (\kappa_0, \kappa_1, \kappa_2, \kappa_3, \kappa_4, \kappa_5, \kappa_6)$ (the strengths of Sol, and Q1 to Q6). While the magnets locations are fixed, their strengths can be individually adjusted.

The initial beam conditions $(X_0, Y_0, X'_0, Y'_0)$ at $z = 0$ are specified at the plane of an aperture plate near the electron gun output. From experiments, we know that this plane is very close to the beam waist, so the initial slopes $(X'_0, Y'_0)$ are close to zeros. The initial beam size for the full beam (100 mA) is determined from the experiment, which is $X_0 = Y_0 = 3.2mm$; the others are identified from their aperture sizes (see Table 1.2). If we integrate the rms envelope equations with magnets strengths $\overline{\kappa} = (\kappa_0, \kappa_1, \kappa_2, \kappa_3, \kappa_4, \kappa_5, \kappa_6)$, the beam radii and slopes $(X_1, Y_1, X'_1, Y'_1)$ at the matching point are functions of $\overline{\kappa}$. The matching error can be expressed as $f(\overline{\kappa}) = (X_1 - X_m, Y_1 - Y_m, X'_1 - X'_m, Y'_1 - Y'_m)$. The matching problem is equivalent to finding a solution set $\{\overline{\kappa}*\}$ such that $\|f(\overline{\kappa}*)\| = 0$. Since there are an infinite number of solutions in $\{\overline{\kappa}*\}$, we may choose the optimal one according to some specific criteria. A local optimization can be done using, for example, an envelope code,

SPOT [41]. SPOT minimizes the "distance" from the envelopes to a properly chosen reference trajectory (normally defined by the average beam radius in the periodic lattice) as well as minimizing $\left\| f(\overline{\kappa}) \right\|$ to zero. However, its optimization criterion using the reference trajectory, as stated above, is not always suitable for our current applications.

In practice, avoiding large envelope excursions is the natural consideration in order to reduce the effects of lens nonlinearities and possible image forces associated with beam offsets. The optimization problem that minimizes large excursions can be stated as $\underset{\{\overline{\kappa}*\}}{Mini}\max(X(\overline{\kappa}*,z)\,\&\,Y(\overline{\kappa}*,z))$. SPOT does not solve this problem. Though the optimization toolbox of MATLAB [42] might do the work, it would take a very significant computing power, which is impractical. To our knowledge, no program exists that can guarantee a global minimum for this problem in a reasonable amount of time.

Alternatively, a sub-optimization can be done in two steps by first finding a subset of discrete solutions $\{\overline{\kappa}^s\}$ from the complete solution set $\{\overline{\kappa}*\}$, i.e. $\{\overline{\kappa}^s\} \subset \{\overline{\kappa}*\}$, and then looking for the optimal one from $\{\overline{\kappa}^s\}$ according to some criteria. We call this a brute-force method. Here, let us denote a single solution $\overline{\kappa}^s$ by the horizontal ($x$) focusing strengths of the magnets (except for the solenoid strength $\kappa_0$, since it has symmetric focusing for both the $x$ and $y$ planes), i.e. $\overline{\kappa}^s = (\kappa_0, \kappa_{x1}, \kappa_{x2}, \kappa_{x3}, \kappa_{x4}, \kappa_{x5}, \kappa_{x6})$. Physically, the values of $\kappa_0$ and $\kappa_{x1}$ to $\kappa_{x6}$ must be bounded within a reasonable range. In the matching of a 100mA beam, we define $\kappa_0$, $\kappa_{x1}$ and $\kappa_{x2}$ by a bounded 3D grid with units m$^{-2}$, i.e. $170 \leq \kappa_0 \leq 310$

(grid-size=1m$^{-2}$, 140 steps), $-366 \leq \kappa_{x1} \leq -104$ (grid-size=2m$^{-2}$, 131 steps), and

$104 \leq \kappa_{x2} \leq 366$ (grid-size=2m$^{-2}$, 131 steps), which correspond to 4.9A to 6.7 A for

the solenoid, and 0.85A to 3.00A for the quadrupoles. For each grid point

$(\kappa_0, \kappa_{x1}, \kappa_{x2})$, the other four quadrupole strengths $(\kappa_{x3}, \kappa_{x4}, \kappa_{x5}, \kappa_{x6})$ can be specified

from the four nonlinear equations $X_1 - X_m = 0$, $Y_1 - Y_m = 0$, $X_1' - X_m' = 0$, and

$Y_1' - Y_m' = 0$. For example, if $(\kappa_0, \kappa_{x1}, \kappa_{x2})$ = (240, -200, 270), we can calculate and

obtain $(\kappa_{x3}, \kappa_{x4}, \kappa_{x5}, \kappa_{x6})$ = (-248.14, 225.49, -233.59, 226.32) by minimizing

$\left\| f(\overline{\kappa}^s) \right\|$ to zero. Thus traversing through the complete 3D grids area as defined

above, we may get a total of 2.46 million (141×132×132) solutions. Solving for

$(\kappa_{x3}, \kappa_{x4}, \kappa_{x5}, \kappa_{x6})$ numerically, e.g. via Newton's method, requires that the initial

guesses do not deviate much from the true solutions. In order to obtain a better initial

guess for each grid point, we travel through the grids in a well-organized sequence, so

a calculation for a grid can inherit a good initial guess from the solution of its nearest

neighbor. We wrote an efficient C program to incorporate all the considerations as

stated above. The calculations first start from a point near the center of the 3D grids,

and then spread out to the neighbors, and gradually to the whole space. During the

process, we also impose a constraint to eliminate the solutions having very large

envelope excursions, i.e. above 2 cm, thus reducing the computing complexity

significantly.

As a result, the calculated $\{\overline{\kappa}^s\}$ for the 100mA beam consists of about 0.23

million solutions, while the other 2.2 million grids are eliminated mostly because the

envelope excursions are too large. With the knowledge of $\{\overline{\kappa}^s\}$, it becomes very straightforward to pick up the "optimal" one according to some specific criteria. Since $\{\overline{\kappa}^s\}$ is comprised of discrete samples from the complete solution set $\{\overline{\kappa}^*\}$, the "optimal" one among the subset is not a true global optimum. However, it will be good enough for practical use.

Let us now examine how to minimize large envelope excursions for $\{\overline{\kappa}^s\}$. We can integrate rms envelope equations over the matching section and find the largest envelope for every solution from $\{\overline{\kappa}^s\}$. The minimal achievable envelope corresponding to the solenoid strength $\kappa_{x0}$ is plotted in Figure 4.8. It indicates the minimum occurring at $\kappa_0 \approx 259$ m$^{-2}$. Increasing the solenoid strength above this value does not help reducing the envelope excursions. The next interesting observation is to look at the "average" quadrupole (Q1 to Q6) strength with respect to $\kappa_0$ in obtaining the minimal envelopes. The relation is plotted in Figure 4.9, where $\overline{\kappa}_{1-6}$ is defined by the square root of the average power consumed by the quadrupoles, i.e. $\overline{\kappa}_{1-6} = \sqrt{(\kappa_{x1}^2 + \kappa_{x2}^2 + \kappa_{x3}^2 + \kappa_{x4}^2 + \kappa_{x5}^2 + \kappa_{x6}^2)/6}$. We see that in order to minimize envelope excursions, the average quadrupole strength needs to be increased with the solenoid as well. This reflects the matching between the magnets. The smallest peak envelope we obtain here equals 14.87 mm (when $\kappa_0 \approx 259$ m$^{-2}$). The corresponding quadrupoles strengths are -232, 286, -251.62, 226.19, -228.45 and 224.45 m$^{-2}$ for $\kappa_{x1}$, $\kappa_{x2}$, $\kappa_{x3}$, $\kappa_{x4}$, $\kappa_{x5}$ and $\kappa_{x6}$, respectively. Figure 4.10 shows such a matched solution. Compared to Fig. 4.7, this solution remarkably reduces the envelope

excursion in the matching section. However, it also creates a small beam at Q1 and, correspondingly, a large envelope split at Q2. For practical use, we may avoid this happening by adding some extra constraints here, e.g. $\kappa_0 < 220$ m$^{-2}$, then the minimal achievable envelope size is about 16.5 mm from Fig. 4.8.
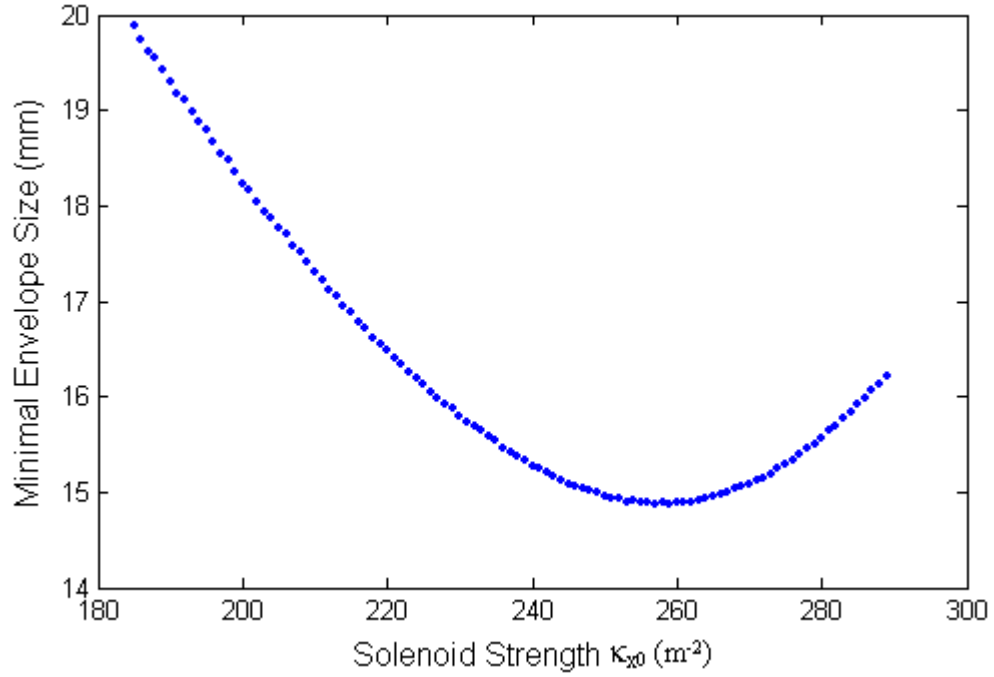


Figure 4.8: The minimal envelope with respect to the solenoid strength for the 100 mA beam.
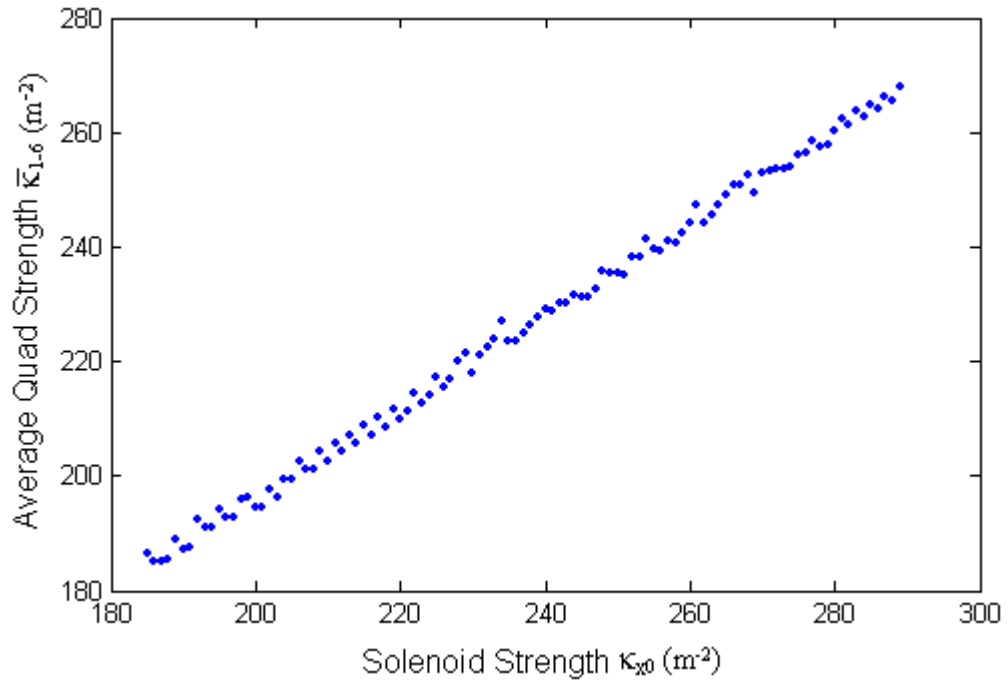
Figure 4.9: Average quadrupole strength with respect to the solenoid strength in obtaining the minimal envelope sizes for the 100 mA beam.
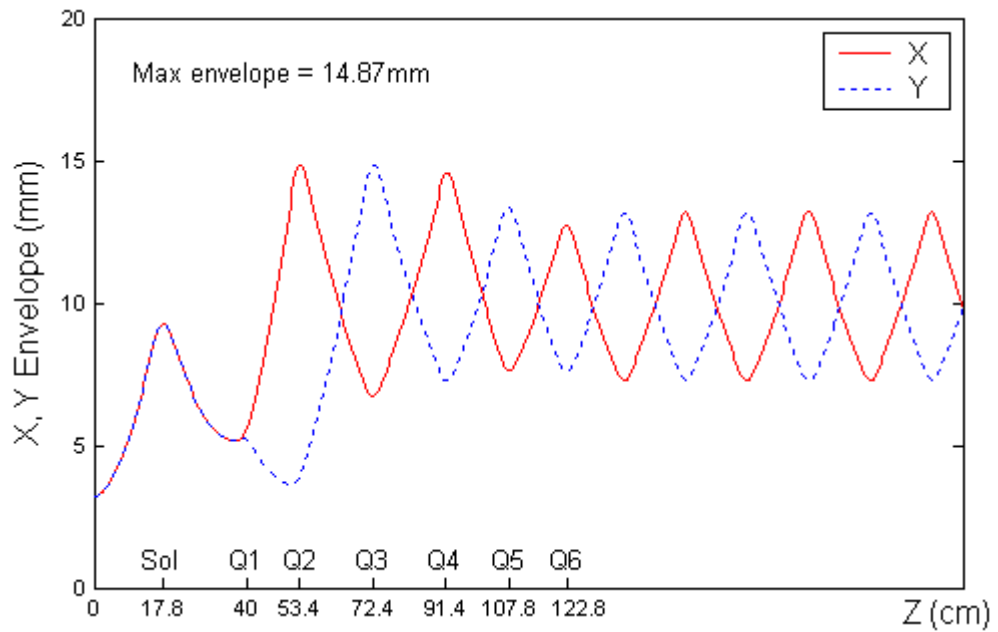


Figure 4.10: A matched solution for the 100 mA with minimal envelope excursion.

## 4.4 Empirical Beam Matching

From the experimental point of view, the accuracy of the matching calculation is always limited by the uncertainties associated with the exact initial beam conditions, beam current, emittances, magnet modeling, magnet locations, etc. Therefore, it is expected that the implementation of the calculated magnet strengths in a real experiment does not yield true matching conditions. Under these circumstances, on-line adjustment of strengths around the calculated values becomes a necessity, an operation that must be guided by the available diagnostics and judicious processing of beam data.

Currently, the UMER ring lattice has 12 diagnostics chambers installed, which cover 24 FODO periods (2/3 of the ring). The periodic feature requires that the matched beam have the same (rms) beam sizes at the plane of phosphor screen in each of the chambers. For example, the evolution of the 24 mA beam, after implementation of the skew correction, was shown in Fig. 3.10(b). Although the beam is not badly mismatched, improvements are possible with the empirical technique that we now describe.

We have seven knobs (Solenoid and Q1 to Q6) in the injector. To obtain a satisfying periodic matching in the ring, we need to adjust at least four of them due to four constraints $(X_m, Y_m, X'_m, Y'_m)$ dictating the matching. We normally do not change the solenoid after it is set in order to avoid hysteresis. In the experiment, we prefer using the last four quadrupoles (Q3 to Q6) for the on-line adjustments, because they are closer to the ring. At the $i$-th diagnostics chamber, empirical matching can be

represented in a matrix form (linear approximation assuming the mismatch is small)
as follows:

$$
\begin{pmatrix} X_i \\ Y_i \end{pmatrix}_{I_1, I_2, I_3, I_4} \approx \begin{pmatrix} X_m \\ Y_m \end{pmatrix} + \begin{pmatrix} R_{xi1} & R_{xi2} & R_{xi3} & R_{xi4} \\ R_{yi1} & R_{yi2} & R_{yi3} & R_{yi4} \end{pmatrix} \cdot \begin{pmatrix} \Delta I_1 \\ \Delta I_2 \\ \Delta I_3 \\ \Delta I_4 \end{pmatrix}, \tag{4.6}
$$

where $X_i$, $Y_i$ are the 2×rms beam sizes in the two transverse directions at the *i-th*
chamber and they are measured when four injector quadrupole currents are set with
$I_1$, $I_2$, $I_3$ and $I_4$; $X_m$, $Y_m$ are the *matched* 2×rms beam sizes at the chamber's location;
$\Delta I_1$, $\Delta I_2$, $\Delta I_3$ and $\Delta I_4$ are the desired current changes to minimize the mismatches for
the four quadrupoles; $R_{xij} = \partial X_i / \partial I_j$, $R_{yij} = \partial Y_i / \partial I_j$ are the changes in $X_i$, $Y_i$ with
respect to the current change of quadrupole $j$, which can be measured by perturbing
the injector quadrupole currents and observing the beam size changes downstream.
For all 12 chambers, the matrix representations can be extended and rewritten as

$$
\begin{pmatrix} X_1 \\ Y_1 \\ X_2 \\ Y_2 \\ \dots \\ X_n \\ Y_n \end{pmatrix} = \begin{pmatrix} R_{x11} & R_{x12} & R_{x13} & R_{x14} & 1 & 0 \\ R_{y11} & R_{y12} & R_{y13} & R_{y14} & 0 & 1 \\ R_{x21} & R_{x22} & R_{x23} & R_{x24} & 1 & 0 \\ R_{y21} & R_{y22} & R_{y23} & R_{y24} & 0 & 1 \\ \dots & \dots & \dots & \dots & \dots & \dots \\ R_{xn1} & R_{xn2} & R_{xn3} & R_{xn4} & 1 & 0 \\ R_{yn1} & R_{yn2} & R_{yn3} & R_{yn4} & 0 & 1 \end{pmatrix} \cdot \begin{pmatrix} \Delta I_1 \\ \Delta I_2 \\ \Delta I_3 \\ \Delta I_4 \\ X_m \\ Y_m \end{pmatrix}, \tag{4.7}
$$

According to our experiment setup, the left hand side vector has 24 elements,
i.e. $n = 12$. The right hand side vector contains six unknown parameters: $\Delta I_1$, $\Delta I_2$, $\Delta I_3$,
$\Delta I_4$, $X_m$, and $Y_m$. Notice that although $X_m$, $Y_m$ can be calculated (using the rms
envelope equations or the PIC code) from the beam current, energy, emittance and the

periodic FODO optics setup, their realistic values will in general deviate from the predictions. Thus treating $X_{\mathrm{m}}$ and $Y_{\mathrm{m}}$ as unknowns is safe in avoiding erroneous results.

If we denote the left hand side of Eq. 4.7 by a column vector $E$, the right hand side matrix by $R$, the solution of the six unknowns can be given in a *least square* sense, i.e. $(R^T R)^{-1} R^T E$. It is physically equivalent to finding an optimal ($\Delta I_1$, $\Delta I_2$, $\Delta I_3$, $\Delta I_4$) that minimizes the variance of $X$, $Y$ beam sizes among all the chambers. After solving Eq. 4.7, the optimal currents of the four quadrupoles are $I_1 - \Delta I_1$, $I_2 - \Delta I_2$, $I_3 - \Delta I_3$, and $I_4 - \Delta I_4$, respectively.

Let us now look at an empirical matching experiment for the 24 mA beam. The beam cross-section pictures before the empirical matching using the scheme just described were shown in Fig. 3.10(b), from which the 2×rms beam sizes are calculated and plotted in Figure 4.11. The standard deviations of $X$, $Y$ beam sizes are 0.45 mm, 0.43 mm, respectively. After empirical matching is implemented, the deviations are reduced to 0.28 mm and 0.21 mm for $X$, $Y$, respectively. The improved beam sizes for all 12 chambers are plotted in Figure 4.12. The beam pictures corresponding to the latter situation are shown in Figure 4.13. They display a significant improvement in the beam quality after implementation of empirical matching as well as steering and skew correction as described earlier.

For future experiments, we can try another successive iteration to reduce the residual mismatch errors, since the linear approximation as expressed in Eqs. 4.6 and 4.7 should be even closer to the true matching condition after the present improvement.
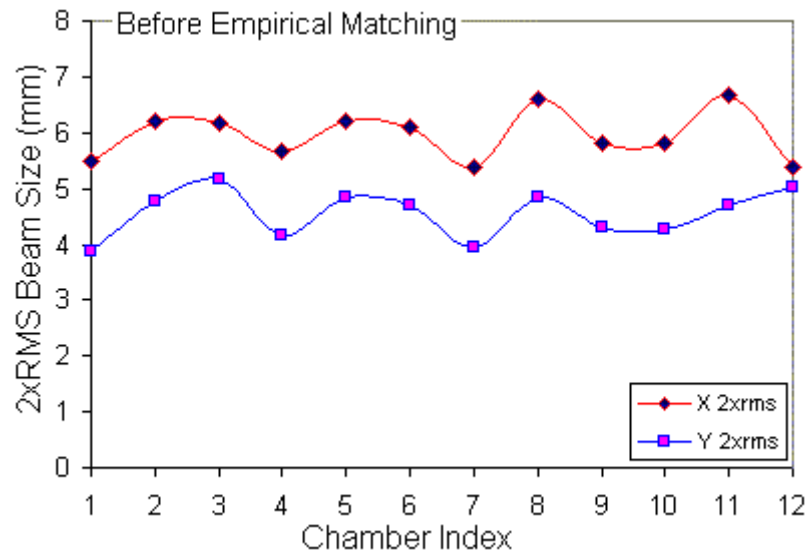
Figure 4.11: Beam at twelve ring chambers (RC1 to RC12) before the empirical matching for the 24 mA beam.
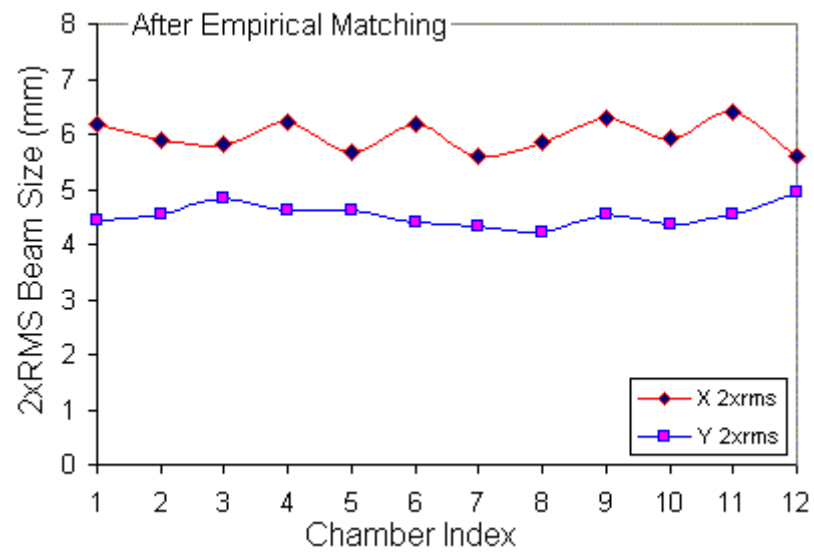


Figure 4.12: Beam sizes at twelve ring chambers (RC1 to RC12) after the empirical matching for the 24 mA beam.
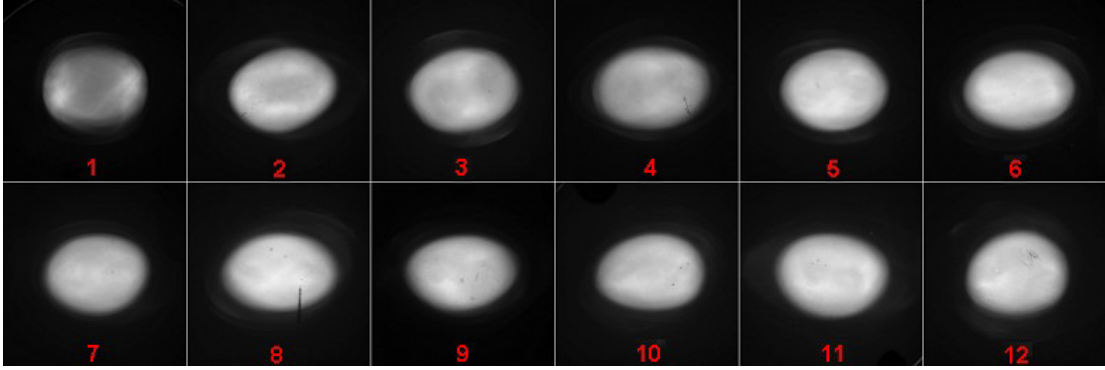
Figure 4.13: Beam cross-section pictures at twelve ring chambers (RC1 to RC12) after the empirical matching for the 24 mA beam.

We also performed similar implementation of this technique to the 7 mA beam. It improved beam matching and beam quality as expected. We have not tested this scheme for the 100 mA beam due to the tight construction schedule and all the difficulties associated with the highest current beams. We believe that this technique is indispensable for the commissioning of UMER.

# Chapter 5 Beam Injection for Multi-turn Operations

The biggest challenge for the completion of UMER is the beam optics design for the injector region. The principal problem here is caused by the fact that the transport of highly space-charge-dominated beams requires short separation between focusing magnets, thus forcing several quadrupoles and dipoles into a very stringent space. The *present* "DC" injector design, as shown in Fig. 4.7(a), is only a temporary solution before the ring is physically closed. Here, "DC" means that all the magnets around the injection region are powered with DC currents. To close the ring, some of the magnets need to be pulsed. For instance (see Fig. 5.1), the normal beam pulse length and the circulation time in UMER are 100 ns and 200 ns, respectively. It implies that the dipole (D0) at the injection point must stay in one polarity at least 100 ns for the injected beam, and switch to another polarity before the beam returns. Since the switching requires high power and a transition time less than 100 ns, the dipole must be specially designed. Not only that several other quadrupoles close by may also need to be pulsed due to the spatial requirement. In this chapter, a new optics design is proposed for solving this problem. We review the previous method where two pulsed and physically overlapping quadrupoles are employed. The new design with only one DC quadrupole reduces both the mechanical and electrical complexities. The single particle motion as well as the space-charge-dominated beam matching is studied to evaluate the new design. Some relevant issues such as stability and experimental considerations (e.g. beam steering) are also discussed for multi-turn operations.
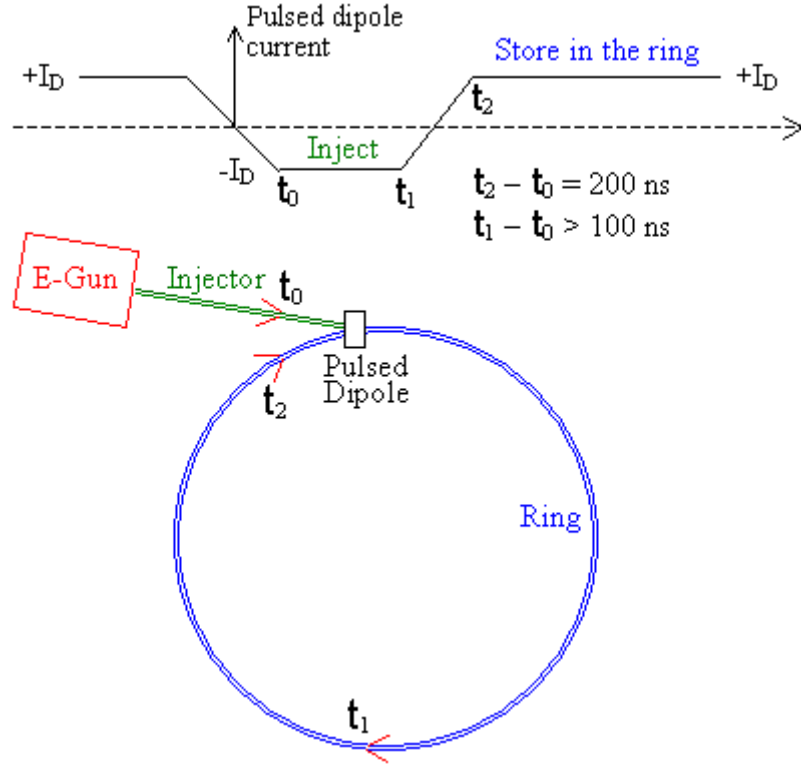
Figure 5.1: UMER multi-turn injection demonstration

## 5.1 Beam Optics Background

We had planned initially to use two pulsed quadrupoles as well as a pulsed dipole. As illustrated in Figure 5.2, the pulsed quad 1 (PQ1) is centered on the injector to provide focusing for the injected beam, while pulsed quad 2 (PQ2), replacing one of the regular ring quadrupoles, is centered on the ring for multi-turn operations. The reason we need PQ1 is that the distance between Q6 and QR1 is too large for good matching. Ideally, we want all distances the same between quadrupoles for this region, hence need PQ1 to fill in. Panofsky quadrupoles [43] with rectangular aperture (as opposed by the regular quadrupoles with circular aperture) are most suitable for this geometry. Figure 5.3 shows a prototype of the Panofsky quad built

for this application. However, by using this method, complex mechanical and electrical issues arise despite the simplicity in the beam optics.
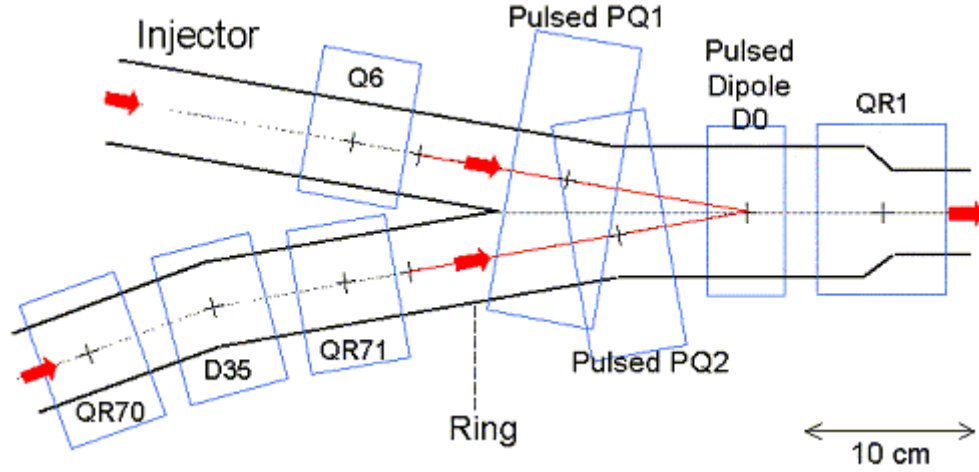


Figure 5.2: UMER injection design scheme 1: PQ1 and PQ2 are two pulsed Panofsky quadrupoles; D0 is the pulsed dipole at the injection point.
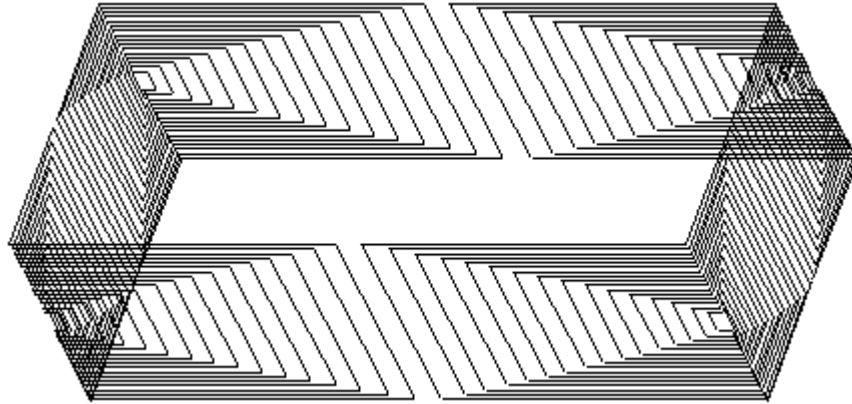


Figure 5.3: Panofsky quadrupole prototype.

First of all, the two quadrupoles must physically overlap. Furthermore, PQ2 has to be squeezed between PQ1 and the pulsed dipole. Thus, we have two quads of

slightly different sizes over a very stringent space. Secondly, one of the PQs must be switched on (off) while the other is off (on) to avoid field overlap. Since we are planning to use wire magnetic quadrupoles, the number of conductors has to be reduced to achieve the desired fast switching, which means that we must make a compromise between field quality and circuit inductance. Also, the mutual inductance between PQ1 and PQ2 must be taken into account in designing the two Panofsky quads. Moreover, a "Y" shape glass pipe is required under those pulsed magnets. It is difficult to manufacture and install.

In order to overcome the disadvantages stated above, we have chosen a simpler scheme [44], which reduces both the mechanical and electrical complexities, but also makes the beam optics more complicated than in the original design. As shown in Figure 5.4, one large DC quadrupole is centered on the bisector of the injector legs and the ring, making $\pm 10^0$ angles with the pipe axes. The large DC quadrupole is called "YQ" because it sits on a region similar to a "Y" shape. When the injected and return beams pass through the large YQ with an angle and an axis-offset, the beams see a dipole field as well as a quadrupole field. The extra dipole term from the offset will be beneficial to assist the bending. In order to adjust the beam centroid exactly into the injection point, two extra short dipoles (SD1 and SD2) are required to steer the beam towards the quadrupole axis. Further, the large YQ must be a defocusing one in the horizontal ($x$) direction so that the beam is bent outward of the injection point.
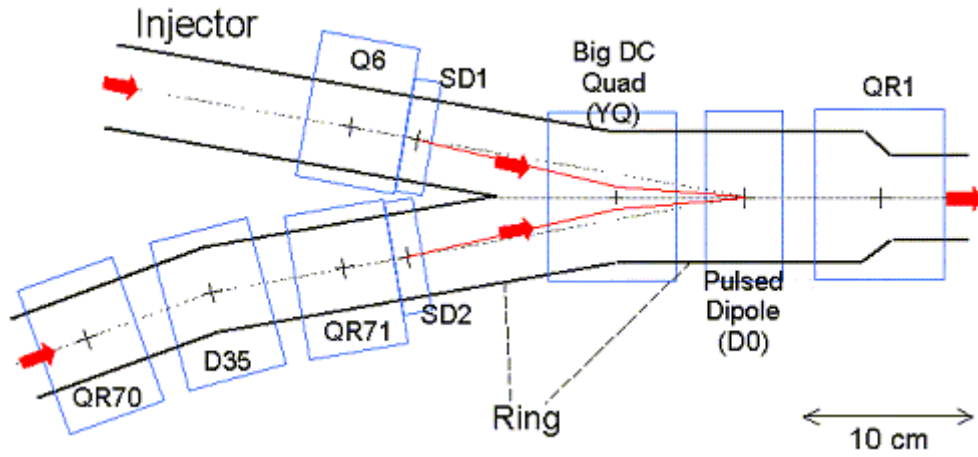
Figure 5.4: UMER injection design, scheme 2: YQ is a big DC quadrupole sitting on a "Y" shape; D0 is the pulsed dipole at the injection point.

The advantage of this new injection scheme resides in its simplicity both mechanically and electrically. (1) Only one pulsed element (D0) is required, hence no mutual influence between pulsed magnets as the former scheme. (2) One large quadrupole is needed instead of two physically overlapping ones. This quadrupole may be either a Panofsky quad with rectangular geometry or a regular one with circular aperture. In practice, we prefer using a circular PC quadrupole because it has been well developed and tested in UMER. (3) The glass cylinder pipe is only under the pulsed dipole instead of a complicated "Y" shape. The mechanical manufacture is much easier. Therefore, we are planning to employ this new injection scheme for the future multi-turn operation. In the following sections, we will describe the relevant optics of beam centroid motion and envelope matching for the injection of space-charge-dominated beams.

## 5.2 Beam Centroid Control

The deflection angle by the short dipole (SD1) must be precisely calculated so the beam centroid can move along the pipe axis after passing through the injection dipole. We have derived a first order solution for the simplified model that is shown in Figure 5.5.
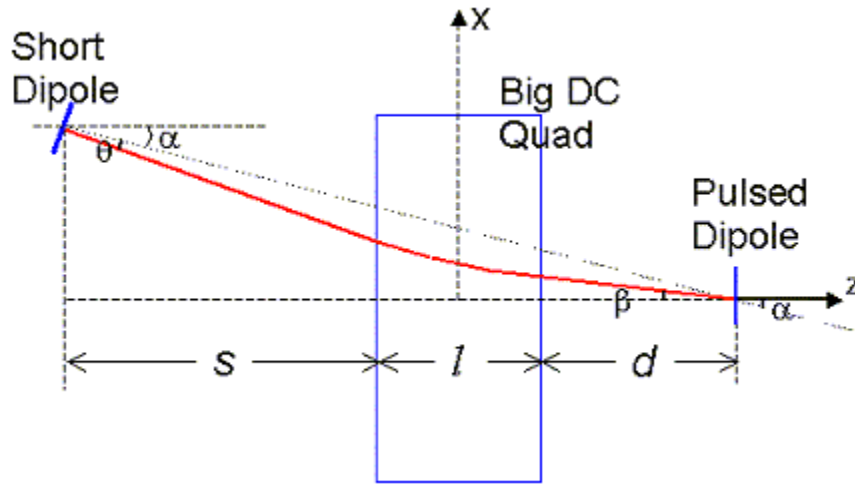


Figure 5.5: Simple injection model: $s$ and $d$ are the lengths of drift region; $l$ is the effective length of the big DC quad.

If we assume that the short dipole (SD1) and the pulsed dipole (D0) are both thin lenses, and the big quad (YQ) is modeled with a "hard-edge" gradient profile and an effective length $l$, the overall transfer matrix can be represented by $M_d \cdot M_l \cdot M_s$, where $M_s$, $M_d$ and $M_l$ are the matrices for the drift regions $s$, $d$ and the quadrupole, respectively. They have the forms:

$$M_s = \begin{pmatrix} 1 & s \\ 0 & 1 \end{pmatrix},$$

(5.1a)

$$M_l = \begin{pmatrix} \cosh kl & \dfrac{1}{k}\sinh kl \\ k\sinh kl & \cosh kl \end{pmatrix}, \tag{5.1b}$$

$$M_d = \begin{pmatrix} 1 & d \\ 0 & 1 \end{pmatrix}, \tag{5.1c}$$

where $k^2 = eG/(m\gamma\beta c)$, and $G$ is the quad field gradient. Hence the transfer matrix of the system after multiplications is:

$$M = \begin{pmatrix} \cosh kl + kd\sinh kl & (s+d)\cosh kl + (1/k + ksd)\sinh kl \\ k\sinh kl & \cosh kl + ks\sinh kl \end{pmatrix}. \tag{5.2}$$

The beam position $x$ and the angle $x'$ at the injection point (D0) can be written in terms of the beam initial conditions $x_0$ and $x_0'$ at SD1, i.e.

$$\begin{pmatrix} x \\ x' \end{pmatrix} = M \cdot \begin{pmatrix} x_0 \\ x_0' \end{pmatrix}, \text{ where } \begin{pmatrix} x_0 \\ x_0' \end{pmatrix} = \begin{pmatrix} (s+d+l)\tan\alpha \\ -\tan(\alpha+\theta) \end{pmatrix}. \text{ Let } a = \cosh kl, \ b = \sinh kl, \text{ then}$$

the final injection error $x$ and injection angle $x'$ can be represented as follows:

$$x = (a + kdb)(s+d+l)\tan\alpha - (a(s+d) + b(1/k + ksd))\tan(\alpha+\theta), \tag{5.3a}$$

$$x' = kb(s+d+l)\tan\alpha - (a+ksb)\tan(\alpha+\theta). \tag{5.3b}$$

The exact deflection angle $\theta$ at SD1 required for the zero injection error can be calculated using $x = 0$. It yields

$$\theta = \tan^{-1}\left(\frac{(a+kdb)(s+d+l)}{a(s+d)+b(1/k+ksd)}\tan\alpha\right) - \alpha. \tag{5.4a}$$

Substituting $\theta$ into equation (5.3b) and using the fact $a^2 - b^2 = 1$, we obtain the injection angle $\beta$ at D0:

$$\beta = \tan^{-1}\left(\frac{(s+d+l)}{a(s+d)+b(1/k+ksd)}\tan\alpha\right). \tag{5.4b}$$

For the UMER injector, given $\alpha = 10^0$, $s = 6.66$ cm, $d = 4.69$ cm, $l = 6.37$ cm and $k = 11.63$ m$^{-1}$, we get the required deflection angle $\theta \approx 2.43^\circ$ and $\beta \approx 7.26^\circ$ from Eqs. (5.4a) and (5.4b).

In reality, there are several factors that may lead to deviations from the above results for $\theta$ and $\beta$. First, the big YQ has a wide fringe field; second, SD1, and especially, D0 are not thin lenses either; third, UMER is often operated in the strong space-charge-dominated regime. In order to reflect all these effects, we performed a more realistic simulation with accurate 3D magnetic fields in the WARP PIC code [31]. In this stage, we chose a typical UMER beam: $I = 24$ mA, $E = 10$ keV, $\varepsilon = 30$ mm·mrad. The simulation yielded the exact solution $\theta \approx 2.58^\circ$ and $\beta \approx 7.23^\circ$, which agrees very well with the approximate solutions from Eqs. (5.4a) and (5.4b).

Another important issue besides the correct $\theta$ and $\beta$ settings is the stability of the scheme. If an initial error $\Delta\theta$ is introduced by SD1, an error at the injection point will occur. The matrix analysis gives the injection errors caused by errors in $\theta$:

$$\Delta x \approx -[a(s+d) + b(1/k + ksd)] \cdot \Delta\theta, \tag{5.5a}$$

$$\Delta\beta \approx -(a + ksb) \cdot \Delta\theta, \tag{5.5b}$$

where $\Delta x$ is the position error and $\Delta\beta$ is the angle error at the injection point. For example, if the short dipole SD1 introduces an error of 1% (0.026$^\circ$), the induced injection errors are about 0.1 mm and 0.05$^\circ$. If the error in $\theta$ is 5% (0.13$^\circ$), the resultant injection errors are about 0.5 mm and 0.23$^\circ$. The big quad therefore amplifies the errors. These injection errors seem small for beam transport over short distances, but it is important to understand the effect for multi-turn operation. Clearly,

the largest potential errors may occur at SD2 and the big YQ (see Fig. 5.4) on the beam return.

Figure 5.6(a) and 5.6(b) show the beam ($x$) centroid motion in 4 turns with 1% and 5% errors ($\Delta\theta/\theta$) in SD1, respectively. The results were obtained from the WARP PIC simulation. The beam parameters we chose for the simulation were still $I = 24$ mA, $E = 10$ keV, $\varepsilon = 30$ mm·mrad. The bending angles by the pulsed dipole and the deflection angle by SD2 are set correctly. The beam ($x$) centroid is measured relative to the reference orbit of the ring lattice. In both Figs. 5.5(a) and 5.5(b), the first negative spike reflects the beam centroid deviation from the injector's pipe center when passing though SD1 and the big YQ. The positive spikes downstream happen exactly when the beam travels back to SD2 and the big YQ in the following turns. From Fig. 5.5(a), the centroid oscillation (ripple) due to the 1% initial error is quite small. From Fig. 5.5(b), the centroid oscillations due to the 5% initial error do not grow in the following turns. The centroid ripples are within 1 mm, which may be corrected with additional steering.

The mechanical design of the new injection scheme has been completed [45]. For the future injector experiments, Eqs. (5.4a) and (5.4b) will be our starting point and guideline for beam steering. Refinements should be possible by changing the strengths of SD1 and D0 iteratively to reduce the injection errors. One may refer to Chap. 2 for a more systematic method about beam steering. It can be summarized as: (1) treat SD1 and D0 as two steering elements; (2) scan two quadrupoles downstream, i.e. QR1 and QR2; (3) measure the relative beam movements in the first diagnostic ring chamber (RC1) either by the BPM or the phosphor screen.
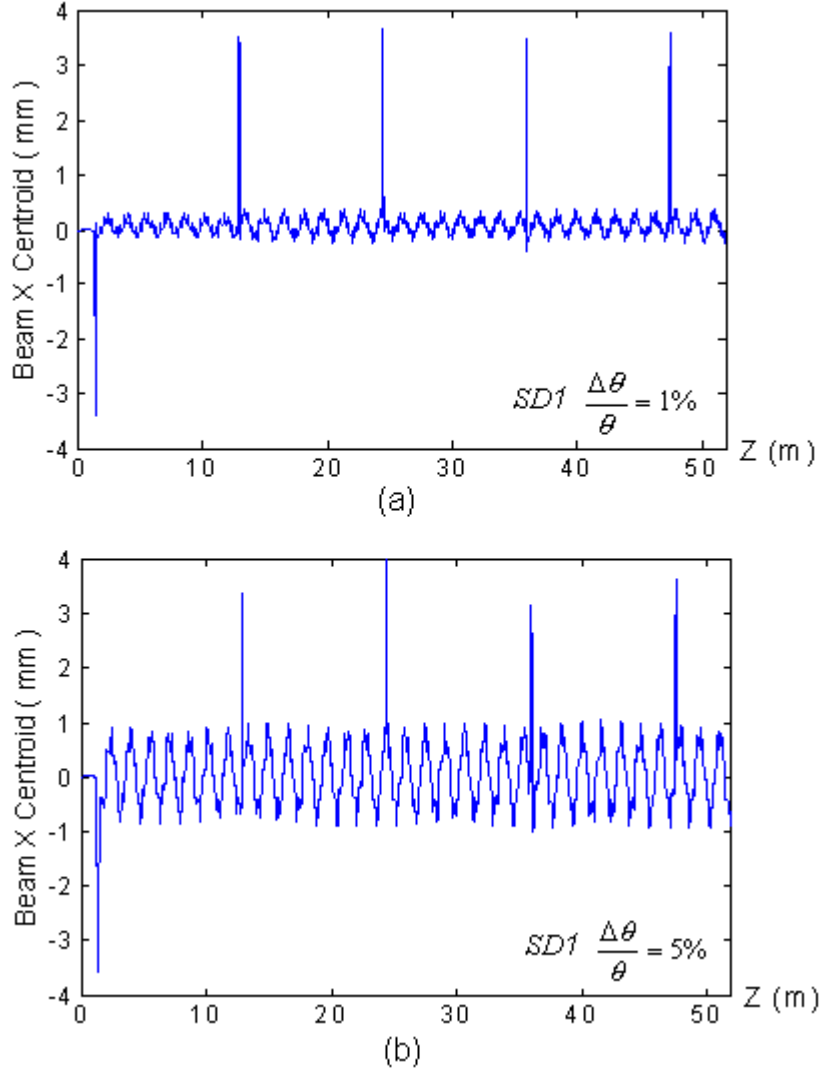
Figure 5.6: (a) Beam centroid motion in 4 turns with an initial angle error 1% by SD1. (b) Beam centroid motion in 4 turns with an initial angle error 5% by SD1.

## 5.3 Quadrupole Field Gradient along the Orbit

For the new injection scheme, the beam centroid travels through the big YQ along a curved trajectory. From the matrix analysis in the previous section, the beam

enters the quad with an angle $\alpha + \theta \approx 10^o + 2.58^o = 12.58^o$ in the horizontal ($x$) plane

and leave the quad with an angle $\beta \approx 7.23^o$. If we use $G(z)$ to represent the

quadrupole field gradient in the $x$-$z$ plane, the gradient $G(s)$ along the centroid orbit

"$s$" can be represented as $G(s) = x \cdot G'(z) \sin \varphi + G(z) \cos \varphi$, where $\tan \varphi = x'(z)$. The

integrated gradient along the orbit can be expressed by

$$\int G(s)ds = \int \left[ xG'(z)\sin\varphi + G(z)\cos\varphi \right] \frac{dz}{\cos\varphi}, \qquad (5.6a)$$

which can be rewritten as

$$\int G(s)ds = \int G'(z) \cdot x \cdot x'(z) \cdot dz + \int G(z)dz. \qquad (5.6b)$$

Equation (5.6b) indicates that the integrated quad gradient along the orbit is

different from the on-axis gradient by an extra nonlinear term, i.e.

$\int G'(z) \cdot x \cdot x'(z) \cdot dz$. It is zero for the normal cases ($x'(z) = 0$). However here, $x'(z)$

is not constant. It changes gradually inside the quadrupole, i.e.

$\tan(-12.58^o) \le x'(z) \le \tan(-7.23^o)$. The average $x'(z)$ is about $\tan(-\alpha)$, where $\alpha$ is

$10^o$ and approximately the middle value of the entry angle and exit angle. Using the

relation $x'(z) \approx \tan(-\alpha)$ and integral by part, we achieve

$$\int G(s)ds \approx (1 - \tan^2 \alpha) \int G(z)dz. \qquad (5.7)$$

Equation (5.7) indicates that the integrated $x$-focusing is slightly different

from the $y$-focusing by a small amount, i.e. $\tan^2 \alpha \approx 3.2\%$. It will introduce a small

asymmetry between the transverse directions when the beam passes through the big

YQ. We believe that it would not be a detrimental effect on the beam quality and

beam matching. In order to be used in the envelope equations for the matching

calculations, this quadrupole may be modeled as an asymmetric "hard-edge" quad with different focusing strengths $\kappa_x = -(1 - \tan^2 \alpha) \cdot \kappa_y$ but the same effective length. In the next section, we will explore the matching problem in details.

## 5.4 Beam Matching

Beam matching is an important topic besides the centroid control. The new injection scheme makes the optics design of the matching section more difficult than before. The reasons can be summarized as follows: (1) the beam will experience a changing quadrupole gradient (though the changes are small) through the big YQ because of the curved trajectory. (2) As discussed in the last section, the integrated field gradients along the beam trajectory for the $x$ and $y$ directions will be slightly different. This introduces a small asymmetry in the focusing. (3) The big YQ has a much larger effective length and longer fringe field than the regular ring quadrupoles, which alters the periodic FODO structure around the injection region. Despite these drawbacks, we can still work on a solution for rms envelope matching. The KV envelope equations combined with the asymmetric "hard-edge" quad model will give us an approximate solution, which can then serve as a starting point for the following PIC simulations. The beam parameters we chose for the PIC code are the same as in section 5.2 about the centroid control.

Figure 5.7 shows a matching solution from the PIC code over a distance of 16 meters. We split the figure into two parts (a and b) in order to display the envelopes' detail. The beam exhibits a slight mismatch (~0.5mm) that does not grow for the following turns (only the second turn is shown here). The mismatch may result from

89

the long fringe field of the large YQ. It is an acceptable result considering the other effects stated above. In the bottom part of Fig. 5.7 (a) and (b), we also plotted the corresponding beam centroid motion. The negative spike occurs when the injected beam passes through the large YQ, while the positive spike occurs when the beam returns to YQ after a turn. The small centroid ripples downstream correspond to effects from the ring bending dipoles. Figure 5.8 shows the evolution of a matched beam cross-section through the injection region, starting from the short dipole SD1. The beam centroid shift is clearly observed.
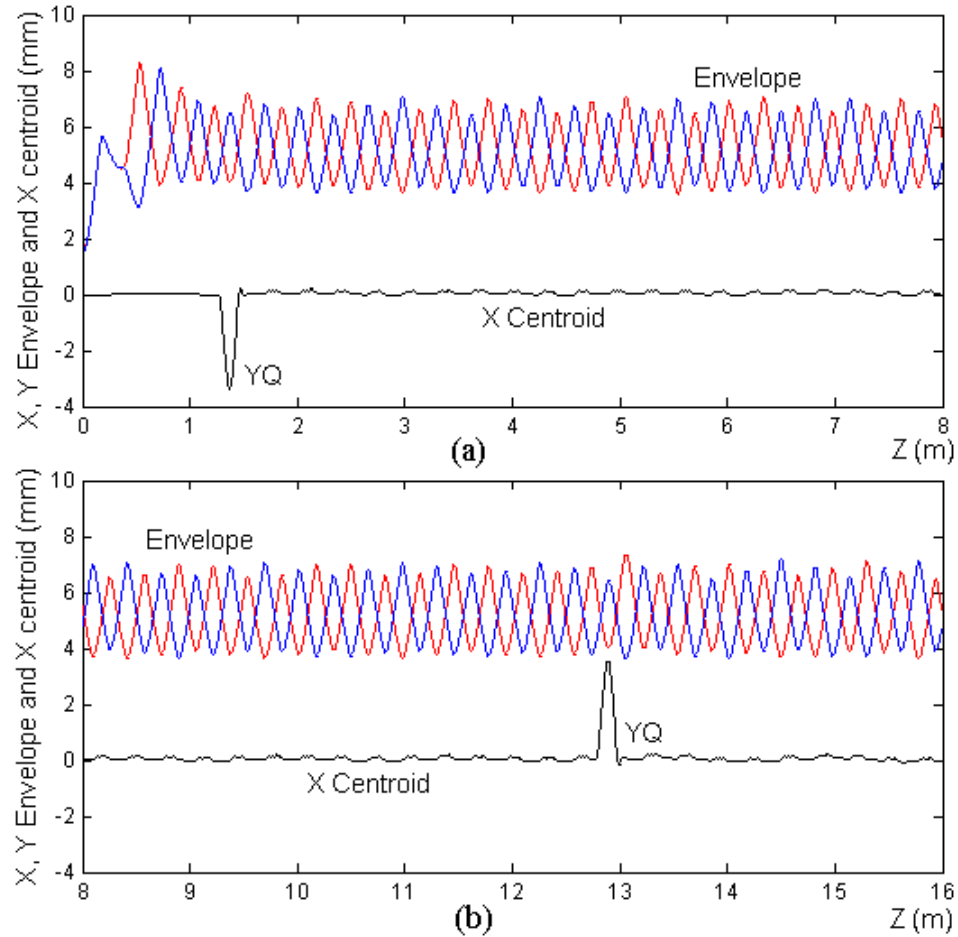


Figure 5.7: Matched envelope solution and *x* centroid over 16 meters for the 24 mA beam: (a) from aperture plate to 8 meter; (b) from 8 to 16 meter.
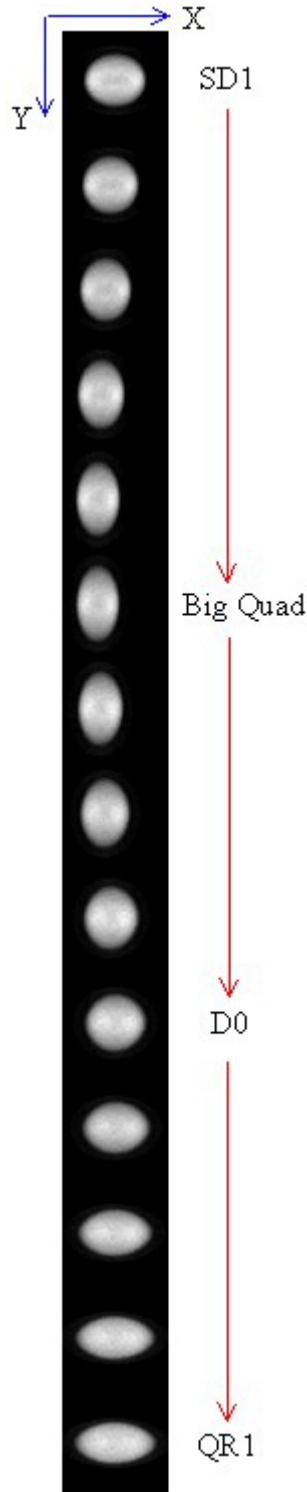
Figure 5.8: Simulated (24 mA) beam cross-section pictures through the injection region: starting form the short dipole SD1 to the first ring quadrupole QR1.

In obtaining the above matching solution for the new injection scheme, an important step is to determine the strengths of the four quadrupoles (YQ, QR1, and two other adjacent quads) around the injection area. This problem can be understood by looking at the ring lattice only. The periodic FODO structure is impaired by the two large quadrupoles (YQ and QR1), not only because they have longer effective length than the regular quads, but also YQ is placed with a $10^\circ$ angle relative to the beam line. Under this circumstance, YQ, QR1, and two other adjacent quads, e.g. QR2, QR3, must be properly adjusted in order to maintain a matched envelope for the other part of the lattice. Two more quadrupoles are needed here because matching to the periodic beam radii and slopes (as dictated by the normal FODO cells) requires four adjustable elements. Figure 5.9 shows such an example where YQ, QR1, QR2, QR3 are tuned with different strengths such that the periodic envelopes (from QR4 to QR71) are recovered after the aperiodic region. We can obtain this matching via either PIC code or envelope code running from a position before YQ (e.g. 8 cm before YQ) with initial beam conditions required from the periodic lattice. The tuning can therefore be done by iteratively adjusting the strengths of the four quadrupoles (e.g. by the Newton method) so as to lead the beam radii and slopes in a position after QR3 (e.g. 8 cm after QR3) equaling the desired values (which are the same as the initial conditions).

From the above analysis, we found three possible ways in choosing the other two quadrupoles besides YQ and QR1: (1) QR2, QR3; (2) QR70, QR71; (3) QR71, QR2. We believe that the combination of QR71, YQ, QR1 and QR2 may bring in a better result in the beam matching, simply because it is a symmetric arrangement: two

large quads (YQ, QR1) in the middle are squeezed between two normal quads (QR71, QR2). This topic will be left for a future simulation or experiments.
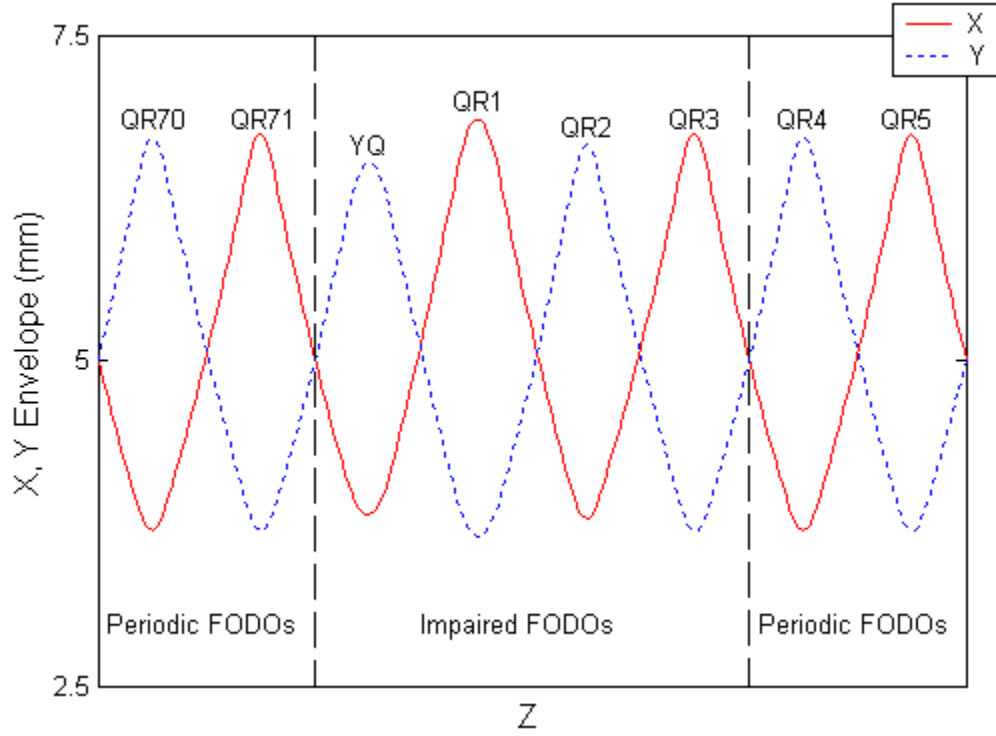


Figure 5.9: Beam matching around the injection area. The beam current for this case is 24 mA.

## 5.5 Summary

The great advantage of the new scheme lies in its simplicity both mechanically and electrically: one large DC quadrupole is used instead of two pulsed quadrupoles of the original design. In studying the beam optics, we have developed a simple model to calculate the deflection angles of the involved magnets, which can be

used as the starting point for the experiments. We have also tested the stability of the

system and developed the matching procedure, and found the results to be acceptable.

# Chapter 6 Beam Phase Space Tomography

We have demonstrated various beam manipulation and control techniques in the previous chapters. These studies include the corrections for the first order and the second order moments of the particle spatial distributions, e.g. the beam centroid $<x>$, $<y>$, and the rms sizes $\sqrt{<x^2>-<x>^2}$, $\sqrt{<y^2>-<y>^2}$. However, in order to understand the particle dynamics, we must have the knowledge of the velocity distributions as well. For example, the (unnormalized) rms emittance, i.e. $\widetilde{\varepsilon}_x = \sqrt{<x^2><x'^2>-<xx'>^2}$, is a widely used measure of the beam quality that includes velocity space information on the beam. In theory, it remains constant if all the forces acting on the particles are linear and there is no acceleration or deceleration, as in UMER. However, any nonlinearities in the focusing channel or from the space-charge self-fields can degrade the beam quality and increase the emittance [46]. This effect is not included in the rms envelope equations, since they were derived under the assumption of constant emittance [6]. Although we could see emittance changes in the self-consistent PIC simulation, the changes depend on the detailed phase space information used to generate an initial particle distribution. A common approach is to assume either a K-V, or a more realistic Semi-Gaussian distribution, which is generally good enough for the lattice design as described in the previous chapters. However, a detailed look into the particle dynamics, e.g. the halo-formation, emittance growth, *x-y* energy transfer and coupling, requires actual phase space knowledge in certain locations. In this chapter, I will describe the phase space

mapping and its applications in UMER using a tomographic technique. Computerized tomography (CT) [47] has been well known in the medical community and was originally developed to process x-ray images. Accelerator scientists have successfully applied this idea for achieving phase space distributions for at least a decade [48, 49]. While the mathematics is relatively straightforward, we describe here its implementation in UMER, including improvements and a simple method for estimating the influence of beam space-charge.

The advantages of tomography techniques reside in the wealth of information about the phase space distributions compared to the standard methods. First, let us examine a conventional quadrupole-scan technique [50]. It measures the phase space Twiss parameters by curve-fitting rms beam sizes as a function of quadrupole strengths. In order to use this method, we must make an a priori assumption of a Gaussian phase space distribution. Tomographic imaging not only avoids this assumption but also yields two-dimensional $(x, x')$ or $(y, y')$ distributions. For low energy electron beams, although another common method, pepper-pot [51], provides a way for two-dimensional phase space mapping, the information obtained is only at discrete points. The accuracy is dominated by its spatial sampling frequency, i.e. the distance between the pepper-pot holes. For beams with larger sizes, this technique can yield acceptable results. For example, the emittance of the 100 mA beam in UMER from the pepper-pot measurement is about 60±20 mm·mrad, which is close to the theoretical predictions based on the gun characteristics [52], but the details of the phase space are not resolved due to the spacing between the beamlets. For beams with smaller sizes, the pepper-pot would intercept fewer beamlets thus limiting its

resolution to a very low level. In practice, we cannot use a pepper-pot method to measure the phase space of the low current beams (0.6 mA, the 7 mA) in UMER because the beam sizes are too small.

In this chapter, we organize the studies in the following order. First, we introduce the tomography algorithms and its relations to the phase space measurement. Then, we describe its implementation in UMER and report the experimental results for the 0.6 mA (pencil) and the 7 mA beam. For the latter beam, a linear space-charge correction is included.

## 6.1 Algorithms

The objective of tomographic imaging is to reconstruct a two-dimensional image of an object from information taken at different angles. The mathematical model can be traced to the Radon transform [53]. The Radon transform of a function $g(u,v)$ is defined as the line integrals for all the directions. That is

$$r(p,\phi) = R \cdot g(u,v) = \int_L g(u,v)ds \,, \tag{6.1a}$$

where the line integral is along the line $p = u\cos\phi + v\sin\phi$ ($0 \le \phi \le \pi$). It also has an alternative form using the Dirac delta function:

$$r(p,\phi) = R \cdot g(u,v) = \iint g(u,v)\delta(u\cos\phi + v\sin\phi - p)dudv \,. \tag{6.1b}$$

It is a linear transform from the spatial space ($u$, $v$) to the projection domain ($p$, $\phi$). Correspondingly, there are several methods to recover the original $g(u,v)$, such as the Algebraic Reconstruction Technique (ART) [54] and the one we discuss

below using the Fourier method [48]. The inverse Radon transforms using the Fourier method can be represented in two equations:

$$\tilde{r}(q,\phi) = \int_{-\infty}^{\infty} |k| \cdot F(k,\phi) e^{i2\pi kq} dk, \tag{6.2a}$$

and

$$g(u,v) = R^{-1} \cdot r(p,\phi) = \int_0^{\pi} \tilde{r}(u\cos\phi + v\sin\phi,\phi) d\phi. \tag{6.2b}$$

Here $\tilde{r}(q,\phi)$ is a modified projection function and is calculated from the one-dimensional inverse Fourier transform of $|k| \cdot F(k,\phi)$, where $F(k,\phi) = \int_{-\infty}^{\infty} r(p,\phi) e^{-i2\pi kp} dp$ is the one-dimensional Fourier transform of the projection function $r(p,\phi)$. Therefore, the tomographic image reconstruction can be done in two steps if a number of projections corresponding to angles from 0 to $\pi$ are known. First, calculate the modified projections according to Eq. (6.2a), then back-project the modified function by integrating Eq. (6.2b) over all the angles. The accuracy of the reconstruction will depend on the number of projections and the corresponding angular spans.

Next, we are going to relate the Radon transform to the phase space mapping. In the experiments, we can easily observe the spatial density distribution $f(x,y)$. The integration of $f(x,y)$ over the $y$-plane yields the $x$ beam profile, which is equivalent to the integration of the phase space distribution function $\mu(x,x')$ along $x'$, i.e.

$$C(x) = \int f(x,y) dy = \int \mu(x,x') dx'. \tag{6.3a}$$

Here $C(x)$ is the beam profile in the $x$ direction. Using the Dirac delta function, it can be written in the form:

$$C(l) = \int \mu(x, x')\delta(x - l)dxdx' . \tag{6.3b}$$

We can easily measure $C(l)$ from the experiments in certain positions ($z$) of the beam line, e.g. the locations of the phosphor screen at the diagnostics chambers. Explicitly, we can write it in terms of $z$:

$$C(l)_z = \int \mu(x, x')_z \, \delta(x - l)dxdx' . \tag{6.3c}$$

Now, it is time to relate this expression to another position $z_0$ in the beam line, where the phase space distribution is $\mu(x_0, x_0')_{z0}$. If we assume that it is a linear system, the particle motion at the two positions obeys

$$\begin{pmatrix} x \\ x' \end{pmatrix} = \begin{pmatrix} M_{11} & M_{12} \\ M_{21} & M_{22} \end{pmatrix} \cdot \begin{pmatrix} x_0 \\ x_0' \end{pmatrix} . \tag{6.4}$$

Also notice two facts: (1) the particle density remains constant in a linear system, i.e. $\mu(x, x')_z = \mu(x_0, x_0')_{z0}$, according to Liouville's theorem [55]; (2) the determinant of the Jacobian matrix $|\partial(x, x')/\partial(x_0, x_0')|$ equals unity. Hence, Equation 6.3(c) can be rewritten in terms of $x_0$, $x_0'$ at $z_0$:

$$C(l)_z = \int \mu(x_0, x_0')_{z0} \delta(M_{11}x_0 + M_{12}x_0' - l)dx_0dx_0' . \tag{6.5}$$

In order to relate Equation 6.5 to the Radon transform represented in Eq. 6.1(b), we define the scaling factor $s$ [48] by

$$s = \sqrt{M_{11}^2 + M_{12}^2} , \tag{6.6a}$$

and the phase space rotation angle $\phi$ [48] by

$$\tan \phi = M_{12} / M_{11} , \tag{6.6b}$$

and $p = l / s$. Now we get the relation:

$$C(l,\phi)_z = \frac{1}{s}\int \mu(x_0,x_0')_{z0}\,\delta(x_0\cos\phi + x_0'\phi - p)dx_0 dx_0' \, . \tag{6.7}$$

Simply, it reads

$$R\cdot\mu(x_0,x_0')_{z0} = r(p,\phi) = s\cdot C(l,\phi)_z \, , \tag{6.8}$$

where $r(p,\phi)$ is the Radon transform of the phase space function $\mu(x_0,x_0')_{z0}$ at $z_0$;

Figure 6.1 demonstrates several scaling examples from a tomography measurement in

UMER. The left column shows directly measured cross-section pictures for the pencil

beam (0.6 mA). The corresponding $x$ beam profiles $C(l,\phi)_z$ integrated over $y$ are in

the middle, and the scaled profiles $r(p,\phi)$ (the Radon transforms) on the right.

In Fig. 6.1, each Radon transform on the right is corresponding to a rotation

angle $\phi$ and a scaling factor $s$, which are calculated from the linear transfer matrix

from $z_0$ to $z$. A successful phase space reconstruction requires the rotation covering a

full $\pi$ range. Scientists normally change the quadrupole strengths (between $z_0$ and $z$)

to reach this goal. A previous tomography experiment [48] in Duke achieved 0.96 $\pi$

rotations using one quadrupole. They had to extrapolate the data for the last 0.04 $\pi$. In

UMER, we have a flexible experimental setup. It allows us to scan more than one

quadrupole, thus making a full $\pi$ rotation possible.
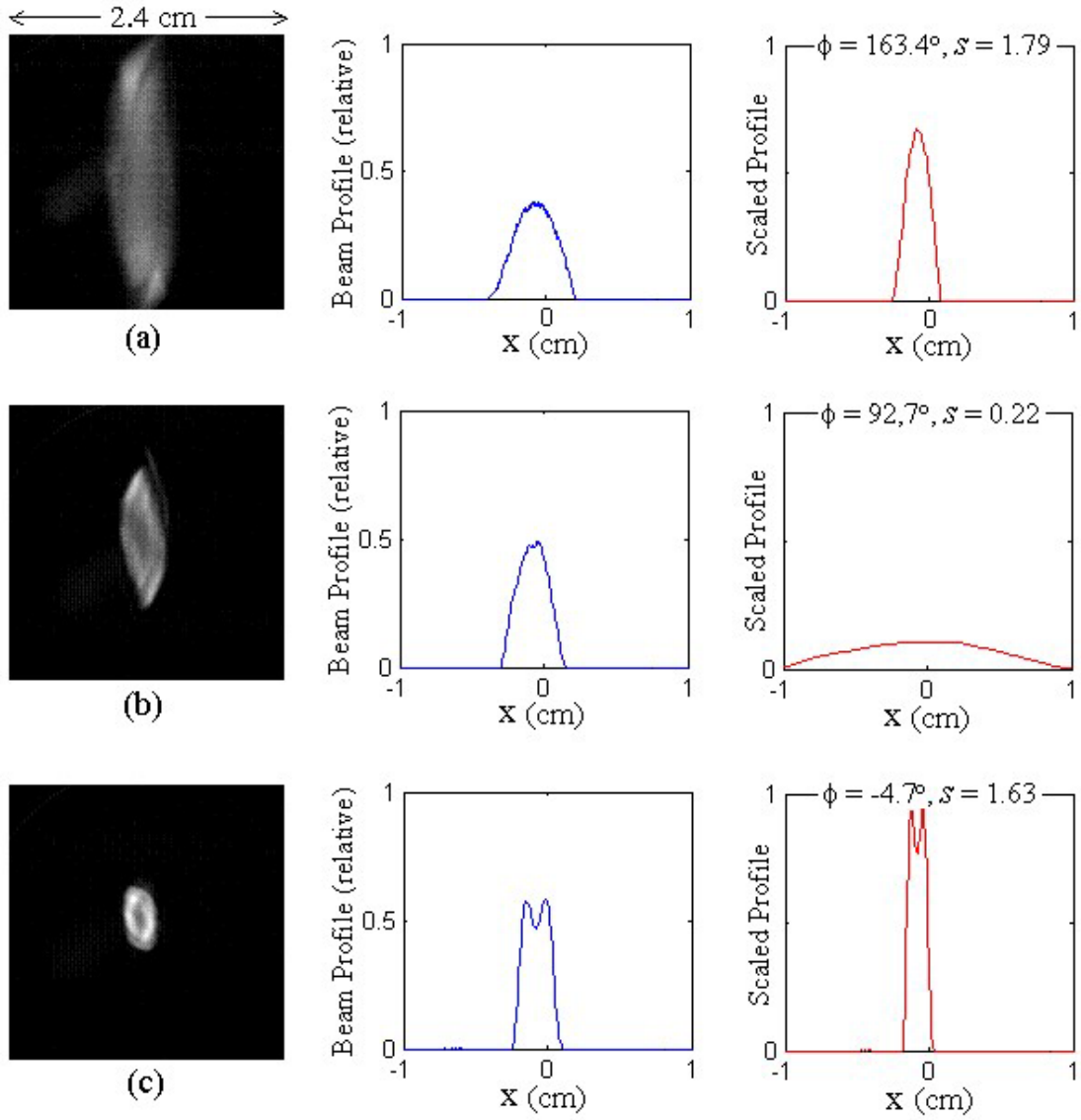
Figure 6.1: Examples of using scaling factor (*s*) to achieve the Radon transform of the reconstructed phase space for a pencil beam at the ring chamber RC1: (a) $\phi = 163.4^o$, $s = 1.79$; (b) $\phi = 92.7^o$, $s = 0.22$; (c) $\phi = -4.7^o$, $s = 1.63$. The left column shows the real spatial (*x*, *y*) beam pictures; the middle shows the integrated *x* profiles; the right one shows the scaled profiles.

## 6.2 Tomography Experiments For Low Intensity Beams

We have assumed linear beam optics in the phase space reconstruction (see Eq. 6.4). It is normally true for many present beam systems, where the space-charge effects are relatively low. In UMER, the lowest intensity beam (the pencil beam), with $I \approx 0.6$ mA, and $\chi \approx 0.3$, is created by using the pencil mask on the aperture plate. This is an ideal test beam for benchmark tomography in UMER.

The experimental setup for tomography in the first ring diagnostics chamber (RC1) is shown in Figure 6.2(a). We employ three quadrupoles, QR1, QR2, and QR3, to achieve a full $\pi$ phase space rotation. The beam profiles are measured downstream of QR3, i.e. at the phosphor screen's location. We also choose the same position for the phase space to be reconstructed, which implies $z_0 = z$ (see the notations in Sec. 6.1). Therefore, we are able to compare the reconstructed phase space distribution $\mu(x_0, x_0')_{z0}$ with the directly measured spatial picture $f(x,y)_{z0}$ in the same plane. In our case, the phase space to be reconstructed is the one when QR1 is operated on the normal current, while QR2, QR3 are turned off. Explicitly, $\mu(x_0, x_0')_{z0}$ is taken at $z_0 = z$, $I_1 = 1.88A$, $I_2 = I_3 = 0$, where $I_1$, $I_2$, $I_3$ are the currents to QR1, QR2, QR3, respectively.
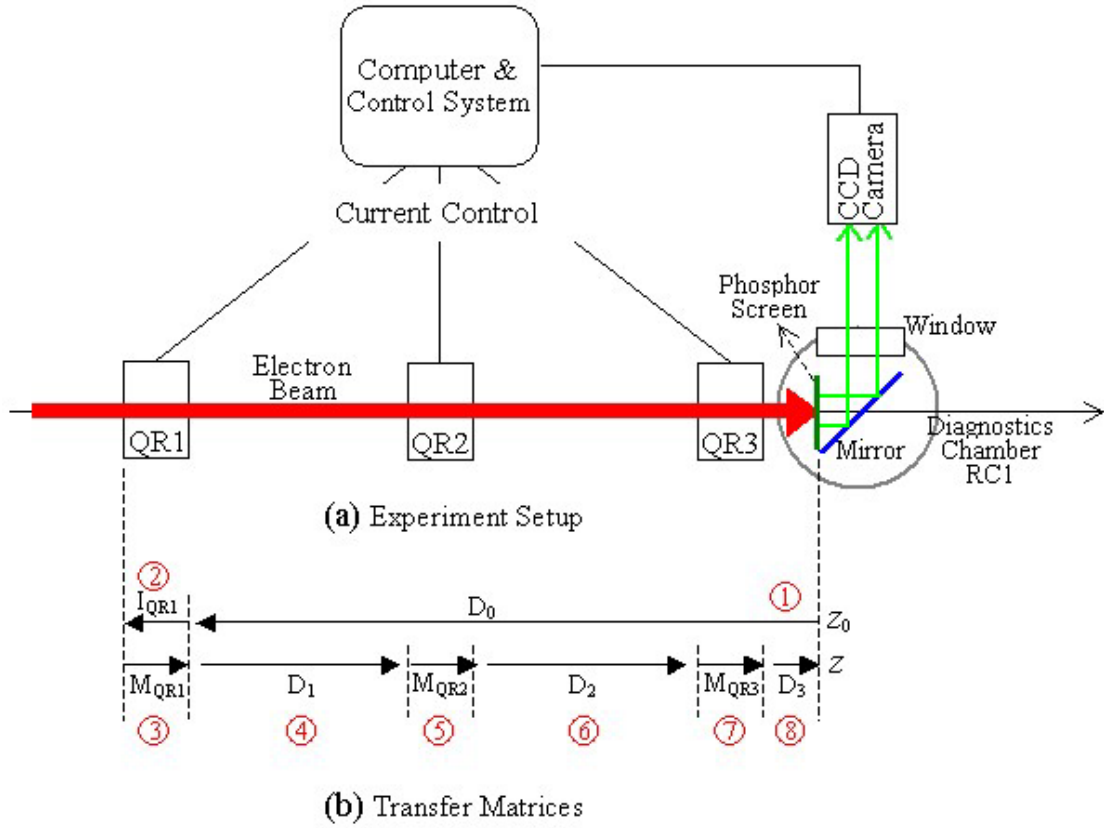
Figure 6.2: Tomography experiment setup and corresponding transfer matrices: (a) Experimental setup for the ring chamber RC1; (b) Transfer matrices from $z_0$ to $z$.

Along with the experimental setup, the relevant matrix representations are illustrated in Figure 6.2(b), where $I_{QR1}$, $M_{QR1}$, $M_{QR2}$, $M_{QR3}$ are the transfer matrices of quadrupoles; $D_0$, $D_1$, $D_2$, $D_3$ are the drift space matrices. Particularly, $I_{QR1}$ and $D_0$ are inverse matrices compared to others, because the electrons need to run backward through them in order to follow a path from $z_0$ to $z$. For example,

$$D_0 = \begin{pmatrix} 1 & l_0 \\ 0 & 1 \end{pmatrix}^{-1} = \begin{pmatrix} 1 & -l_0 \\ 0 & 1 \end{pmatrix},$$

$$I_{QR1} = \begin{pmatrix} \cos(kl_q) & 1/k \cdot \sin(kl_q) \\ -k\sin(kl_q) & \cos(kl_q) \end{pmatrix}^{-1} = \begin{pmatrix} \cos(-kl_q) & 1/k \cdot \sin(-kl_q) \\ -k\sin(-kl_q) & \cos(-kl_q) \end{pmatrix},$$

where $l_0$ is the drift space length from QR1 to $z_0$; $l_q$ is the effective length of QR1; $k$ is the square root of the quadrupole strength *kappa* corresponding to the normal operation current $I_1 = 1.88A$ or $\kappa_1 = 230\,\text{m}^{-2}$. Hence, the overall transfer matrix, $R$, from $z_0$ to $z$ can be represented as

$$M = D_3 \cdot M_{QR3} \cdot D_2 \cdot M_{QR2} \cdot D_1 \cdot M_{QR1} \cdot I_{QR1} \cdot D_0. \tag{6.9}$$

In order to achieve a full $\pi$ phase space rotation, we vary the strengths of QR1, QR2, QR3 such that $M_{QR1}$, $M_{QR2}$, $M_{QR3}$ are changed. However, there are certain restrictions imposed on the changes. First, the maximum allowed current for each quadrupole is ±3.5 A (±427 $\text{m}^{-2}$ for kappa). Second, the beam size at the measurement point must be controlled to remain within the phosphor screen. Third, the beam size must be kept within a reasonable range when it travels through the pipes, in order to avoid the beam hitting the pipe or possible image-charge effects. Considering all these factors, we found some interesting observations. For example, the three quadrupoles play different roles in the phase space reconstruction.

QR3 has little effect on rotating the phase space because it is too close to the phosphor screen. However, it can serve as a focusing element, or in other words, a remedy method, to control the beam to remain within the screen if the beam size grows too much.

QR2 is the one that dominates the phase space rotations. By changing the current of QR2 from −3.5A to +3.5A, keeping QR1 at the normal current and turning

QR3 off, we can achieve a 0.955 $\pi$ rotation. The rotation angle $\phi$ and the scaling

factor $s$ with respect to the current $I_2$ are plotted in Figure 6.3 (a) and (b).
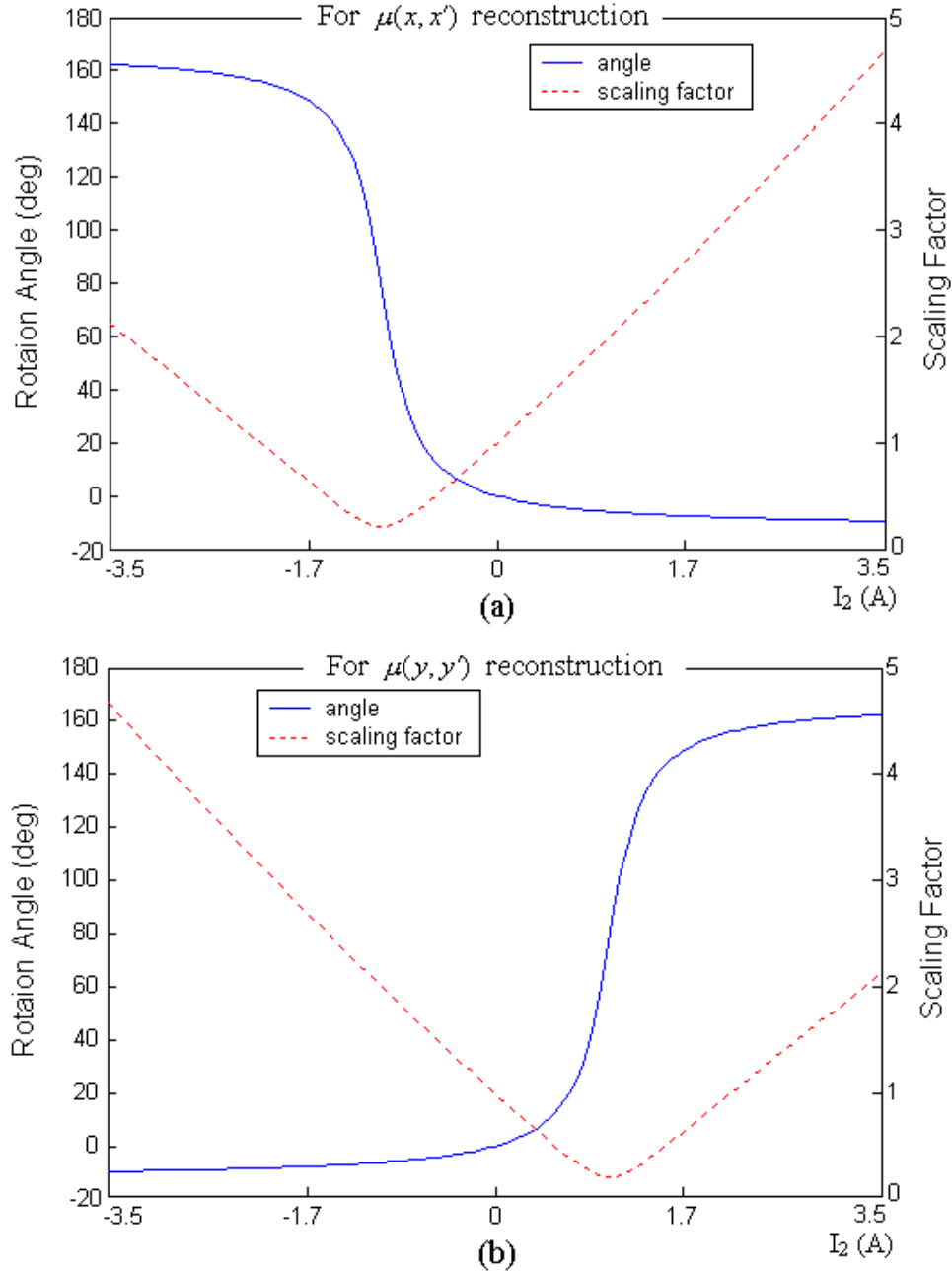


Figure 6.3: Rotation angle ($\phi$) and scaling factor ($s$) v.s. $I_2$ when $I_1 = 1.88$ A and $I_3 = 0$A. (a) rotation angle and scaling factor for $\mu(x,x')$ reconstruction; (b) rotation angle and scaling factor for $\mu(y,y')$ reconstruction.

The last $0.04\,\pi$ rotation angle can be obtained by changing QR1 around its normal strength and properly adjusting QR3 to limit the beam size. It is possible that the beam could hit the pipe before QR3, but it will be observed if it happens, so this sets a limit to the current ranges of QR2 and QR3. In our case, we achieved a full $\pi$ rotation of the reconstructed phase space by properly changing the currents of the three quadrupoles without losing beams.

As a result, we generate a table containing the quad currents, the resulting rotation angles and scaling factors, i.e. $(I_1, I_2, I_3, \phi, s)$. In the experiment, the tomography program reads the table, then performs the reconstruction as follows: (1) change $I_1, I_2, I_3$ via a computer controlled interface; (2) capture the spatial $(x, y)$ beam pictures via a CCD camera; (3) calculate the beam profile by integration; (4) generate the Radon transform using the scaling factor $s$ and Eq. 6.8; (5) calculate the modified projection function using Eq. 6.2(a); (6) integrate the modified projections over $\phi$ using Eq. 6.2(b).

The promising part of our tomography program is that it realizes the control, measurement and reconstruction simultaneously. A complete reconstruction only takes about 10 minutes for the pencil beam. It is very useful for an on-site determination of the experimental results.

We have performed tomography experiments for the pencil beam at the ring chamber RC1 and RC6. The reconstructed phase space distributions and the corresponding spatial pictures are illustrated in Figure 6.4 and 6.5. Carefully analyzing the results, we found several points worth noting:

(1) The phase space distributions in Figs. 6.4 and 6.5 display very high image qualities. The background noises are about 5% of the peak intensity for all the pictures. This is because the reconstructions covered a full $\pi$ rotation and a large number of projections.

(2) We calculated the 4×rms emittances (effective emittances) using the definition $\varepsilon_x = 4 \times \sqrt{< x^2 >< x'^2 > - < xx' >^2}$ from the reconstructed phase space distributions. The results are $\varepsilon_x \approx \varepsilon_y \approx$ 5.4±0.2 mm·mrad at the ring chamber RC1, and $\varepsilon_x \approx \varepsilon_y \approx$ 5.8±0.2 mm·mrad at RC6. We believe that the results are accurate. Besides the excellent image qualities as stated above, there are other reasons to support these results. First, assuming a uniform phase space distribution in the aperture plate, we estimate the emittance of the pencil beam to be 4.7±1.6 mm·mrad, approximately, by scaling it with the full beam (the radius and the emittance are 3.2 mm, 60±20 mm·mrad for the full beam; the radius is 0.25 mm for the pencil beam). Also, we had measured the emittance of the pencil beam using a quadrupole scan technique by measuring the beam sizes and fitting the Twiss parameters. It yielded $\varepsilon_x \approx \varepsilon_y \approx$ 6.5±0.5 mm·mrad, but that method made an a priori assumption of a Gaussian profile. Compared to the results from the prediction (scaling with the full beam) and the quad scans, the emittance calculated from the tomography reconstruction is about the average of the two.

(3) Fig 6.4(a) and 6.5(a) are the real spatial (x, y) beam pictures. They were taken by the CCD camera when $I_1 = 1.88A$, $I_2 = I_3 = 0$, which is required according to the previous discussions. As a verification of the reconstructed phase space

distribution, we calculated the 2×rms $x$ beam size from the $(x, x')$ phase space image, and $y$ beam size from the $(y, y')$ phase space image, and compared them with the results from the spatial $(x, y)$ picture. Table 6.1 shows the comparisons.

Table 6.1: Calculated beam sizes from spatial and phase space images

| Ring Chamber | RC1 | | | RC6 | | |
|---|---|---|---|---|---|---|
| Source Pictures | $(x, y)$ | $(x, x')$ | $(y, y')$ | $(x, y)$ | $(x, x')$ | $(y, y')$ |
| $x$ (2×rms) mm | 1.57 | 1.52 | — | 1.11 | 1.09 | — |
| $y$ (2×rms) mm | 4.05 | — | 4.01 | 3.43 | — | 3.26 |

(4) From the $(x, x')$ phase space picture in RC1 (Fig. 6.4b), we can see a hollow velocity distribution. The spatial $x$ profile also displays a hollow structure (Fig. 6.4a). These phenomena are clearly due to the effects from the cathode grid according to the earlier studies [56, 57]. Examining in RC6 (3.2 meter apart from RC1), though the spatial x profile is blurred (Fig. 6.5a), we can still recognize some hollowness from the $(x, x')$ phase space distribution (Fig. 6.5b). This observation is an example of the wealth of information that can be obtained from the phase space tomography.

Figure 6.4: Pencil beam (0.6 mA) phase space tomography in the ring chamber RC1: (a) spatial $(x, y)$ beam pictures; (b) $(x, x')$ phase space distribution; (c) $(y, y')$ phase space distribution.
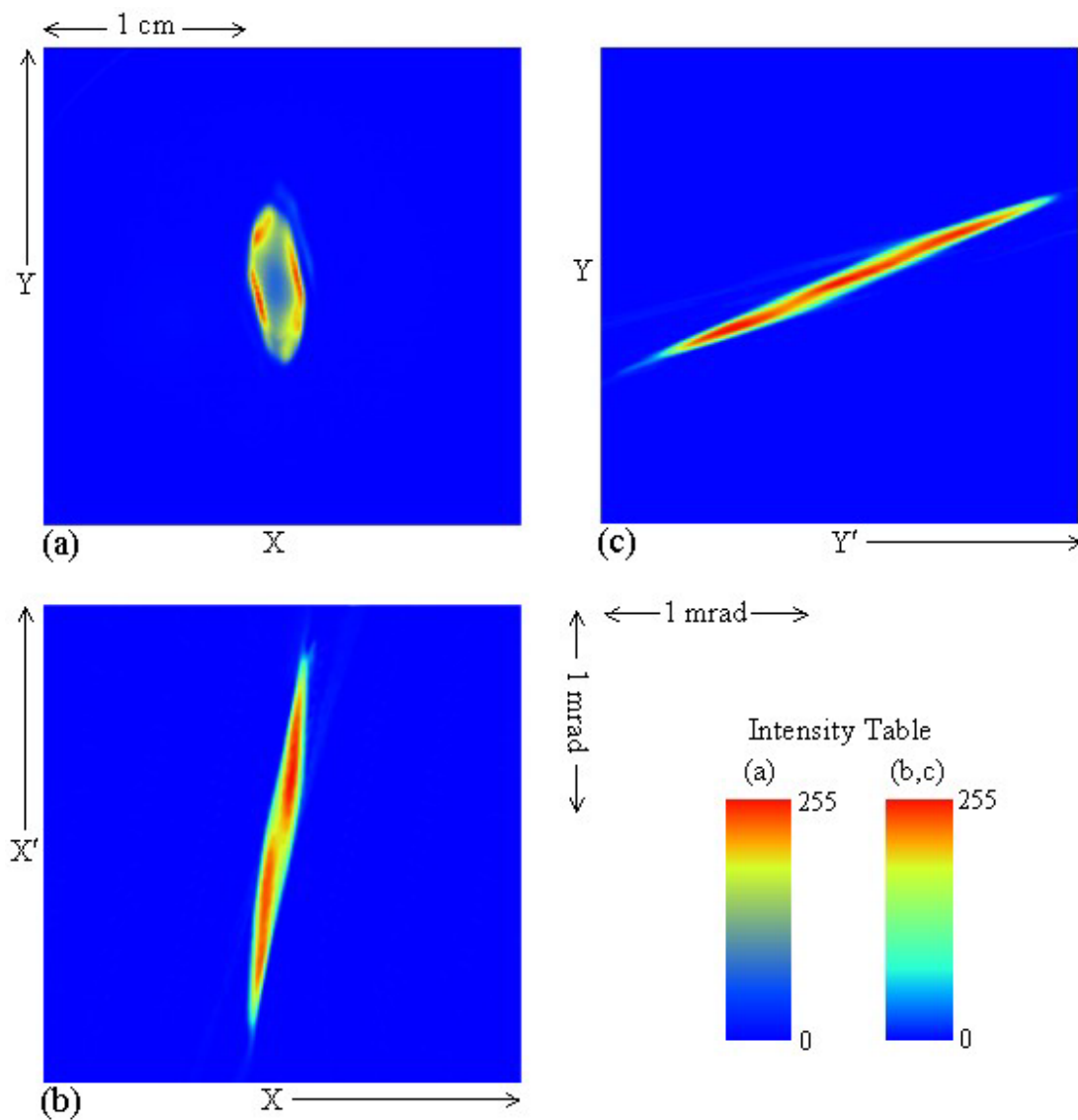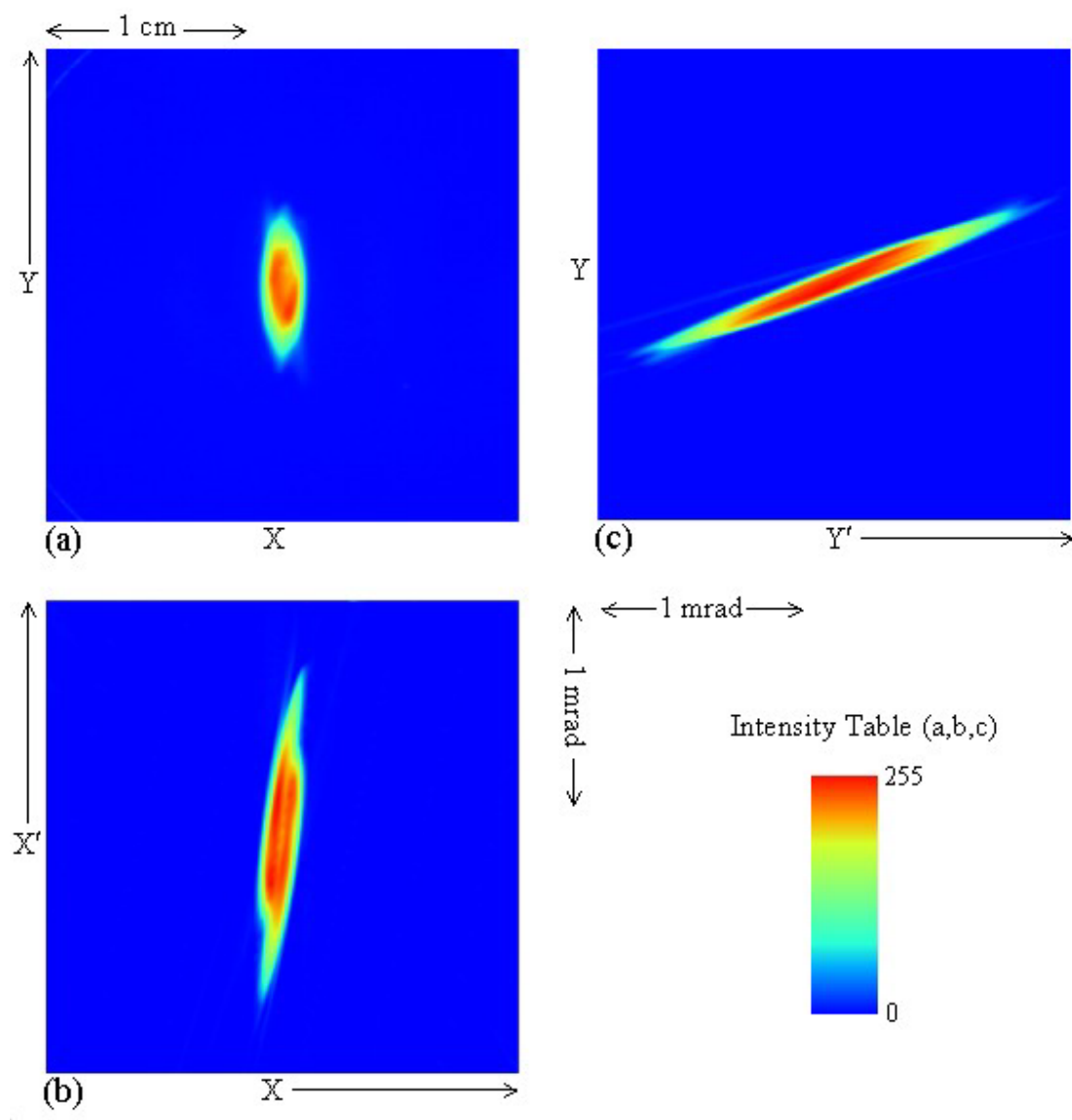
Figure 6.5: Pencil beam (0.6 mA) phase space tomography in the ring chamber RC6: (a) spatial $(x, y)$ beam pictures; (b) $(x, x')$ phase space distribution; (c) $(y, y')$ phase space distribution.

## 6.3 Tomography Experiments for Beams with Space-charge

In this section, we will study the phase space reconstruction using the tomography technique for a space-charge-dominated beam of I $\approx$ 7.0 mA, and an intensity parameter $\chi \approx 0.78$. Since this is an intense electron beam, space-charge effects must be taken into consideration. The simple method we employ here is a linear space-charge correction estimated from the beam envelopes.

From the particle motion equations including the linear space-charge forces (see Eqs. 4.3a and 4.3b), the net focusing strengths acting on a particle are

$$\kappa_x = \kappa_{x0} - \frac{2K}{X(X+Y)}, \tag{6.9a}$$

$$\kappa_y = \kappa_{y0} - \frac{2K}{Y(X+Y)}, \tag{6.9b}$$

where $\kappa_{x0}$, $\kappa_{y0}$ are the external focusing functions; $X$, $Y$ are the beam envelopes for the $x$ and $y$ directions, respectively. For low intensity beams (e.g. the pencil beam), we only use $\kappa_{x0}$, $\kappa_{y0}$ in generating the transfer matrices and calculating the rotation angles and scaling factors. However, for the 7 mA beam, the space-charge terms, i.e. $-2K/X(X+Y)$ and $-2K/Y(X+Y)$, must be included into the matrices.

The calculations including the space-charge terms are very complicated. The main difficulties reside in the determination of the envelope $X$, $Y$. Mathematically, they are not only functions of $z$, but also functional of $\kappa_{x0}$ and $\kappa_{y0}$. This implies that $X(z)$, $Y(z)$ change with the external focusing functions $\kappa_{x0}(z)$ and $\kappa_{y0}(z)$. Examining the experimental setup in Fig. 6.2 (a), we do not have any diagnostics over a distance

crossing three quadrupoles (QR1, QR2, QR3). The envelope evolutions are unknown in this area. Fortunately, we can estimate the beam sizes and slopes ($X$, $Y$, $X'$, $Y'$) with a reasonable accuracy before the first quadrupole (QR1). Using these estimates as the initial conditions, we can calculate the envelopes via the rms envelope equations with respect to all the external focusing functions ($\kappa_{x0}$, $\kappa_{y0}$). We can also verify the calculations by comparing the calculated and measured beam sizes at the phosphor screen location. If they do not agree well, we adjust the initial guesses ($X$, $Y$, $X'$, $Y'$), and redo the calculation until an acceptable agreement is reached. Figure 6.6 shows such an example for the verification of the envelope evolutions of the 7 mA beam. The beam sizes were measured in RC1 with respect to different quadrupole (QR1, QR2, QR3) settings. In the calculation, we used the same ($\kappa_{x0}$, $\kappa_{y0}$) as in the experiments. The calculations and the measurements agree very well according to the figure. In practice, we should not expect a perfect match because the measurement of beam sizes is also subject to errors.

With the knowledge of the envelope evolution with respect to ($\kappa_{x0}$, $\kappa_{y0}$), we can calculate the net focusing strengths including the space-charge forces as functions of $z$, i.e. $\kappa_x = \kappa_{x0} - 2K/X(X+Y)$ and $\kappa_y = \kappa_{y0} - 2K/Y(X+Y)$. The new transfer matrices for ($\kappa_x$, $\kappa_y$) can be modeled by the superposition of many "hard-edge" sub-elements. Hence, the rotation angles ($\phi$) and the scaling factors ($s$) including the space-charge corrections are obtained. Figure 6.7 shows the calculated $\phi$, $s$ for the 7 mA beam when $I_1 = 1.88A$, $-3.5A \leq I_2 \leq 3.5A$, and $I_3$ is changed with $I_2$ from $-2A$

to 0A (limiting the beam size within the screen). Both results with the space-charge and without the space-charge are illustrated.
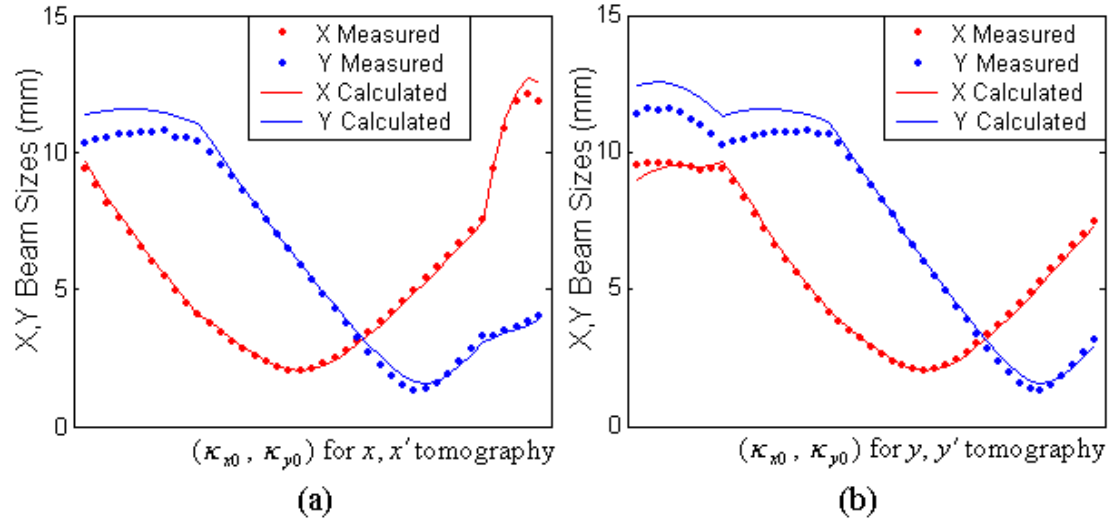


Figure 6.6: Beam size measurements v.s. the calculations at the phosphor screen in RC1 for the 7 mA beam.
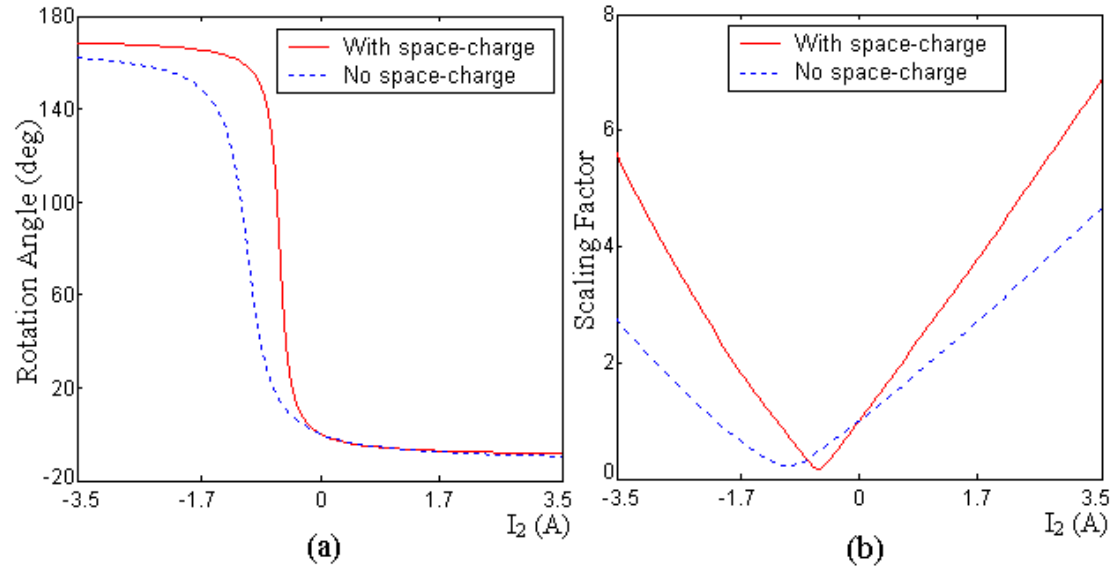


Figure 6.7: Phase space rotation angles and scaling factors for the 7 mA beam in RC1 with respect to $I_2$.

Let us examine the reconstructed phase space including the space charge for the 7 mA beam. The experimental setup and procedures are the same as the case for the pencil beam. Figure 6.8 and 6.9 illustrate the results.

In order to verify the reconstructed distributions, we calculated the 4×rms emittances from the phase space images in Fig. 6.8 and 6.9. The results are $\varepsilon_x \approx$ 15.2±1.0 mm·mrad, $\varepsilon_y \approx$ 14.7±1.0 mm·mrad in the ring chamber RC1; and $\varepsilon_x \approx$ 16.5±1.0 mm·mrad, $\varepsilon_y \approx$ 15.0±1.0 mm·mrad in the ring chamber RC6. Because the initial aperture size of this beam is 0.875 mm, the estimated emittance is about 16.4±5.0 mm·mrad by scaling with the full beam (3.2 mm in size, 60±20 mm·mrad in emittance). Therefore, the results from the reconstructed phase space distributions are reasonable. Besides, we notice that the emittance has increased by about 1.3 mm·mrad for $\varepsilon_x$, but only 0.3 mm·mrad for $\varepsilon_y$, over a distance of 3.2 meter (from RC1 to RC6). This asymmetric increase is possible because ten bending dipoles from RC1 and RC6 may result in larger emittance growth in the horizontal ($x$) plane due to the dispersion effect [58].

Based on the above analysis, we believe that the linear space-charge correction is a practical technique for intense beam tomography. An even more realistic phase space distribution can be resolved using current results as an initial guess, and running the PIC code iteratively in order to fit to the measured ($x$, $y$) density profiles, thus incorporating the *nonlinear* space-charge forces self-consistently. The numerical convergence will depend on a good initial particle distribution, e.g. the distribution from the current tomographic method including the

linear space-charge correction. Combining both the tomographic imaging and the self-consistent PIC code results will be a challenging study in the future.
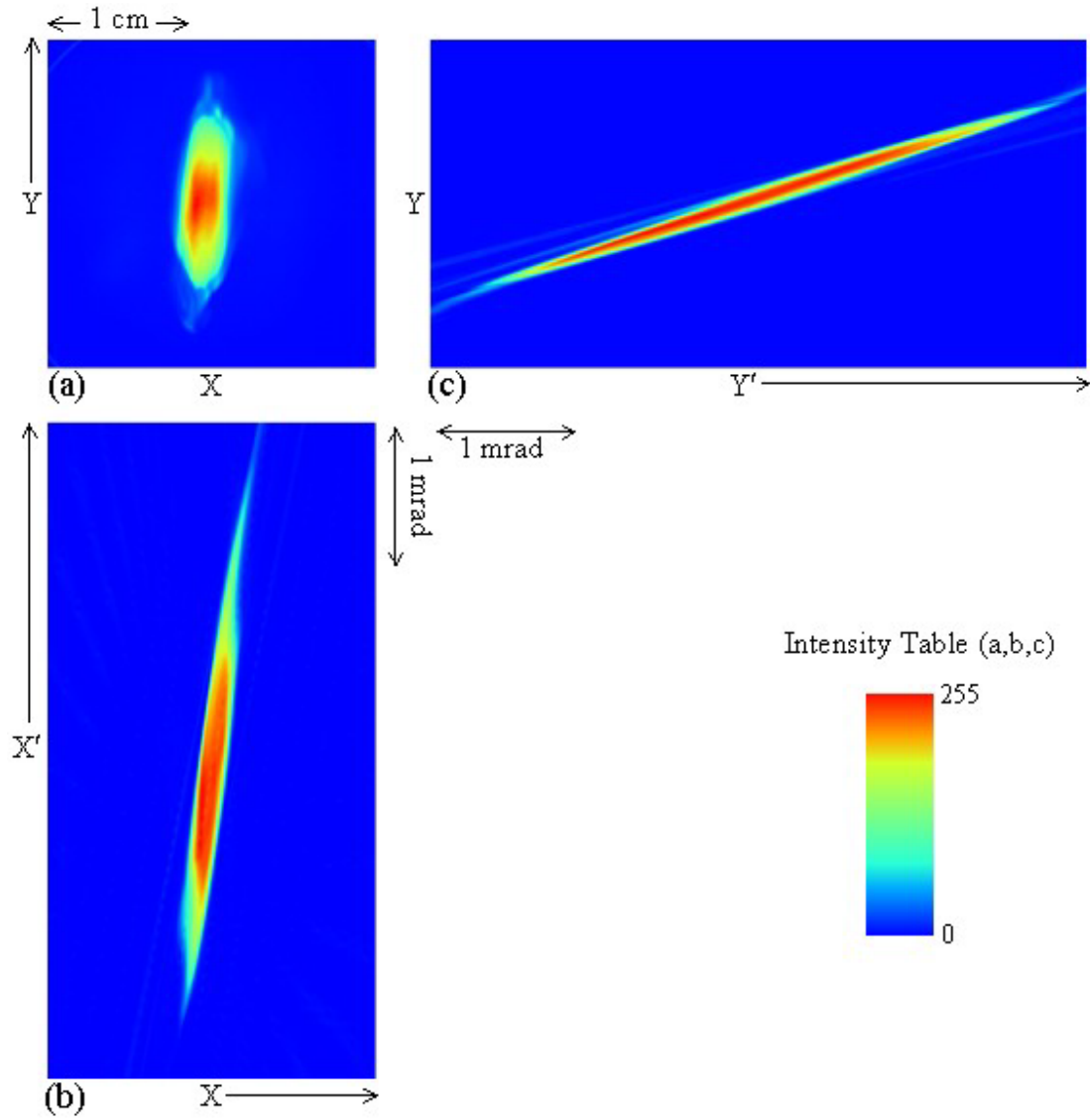
Figure 6.8: Phase space tomography for the 7 mA beam in the ring chamber RC1: (a) spatial $(x, y)$ beam pictures; (b) $(x, x')$ phase space distribution; (c) $(y, y')$ phase space distribution.
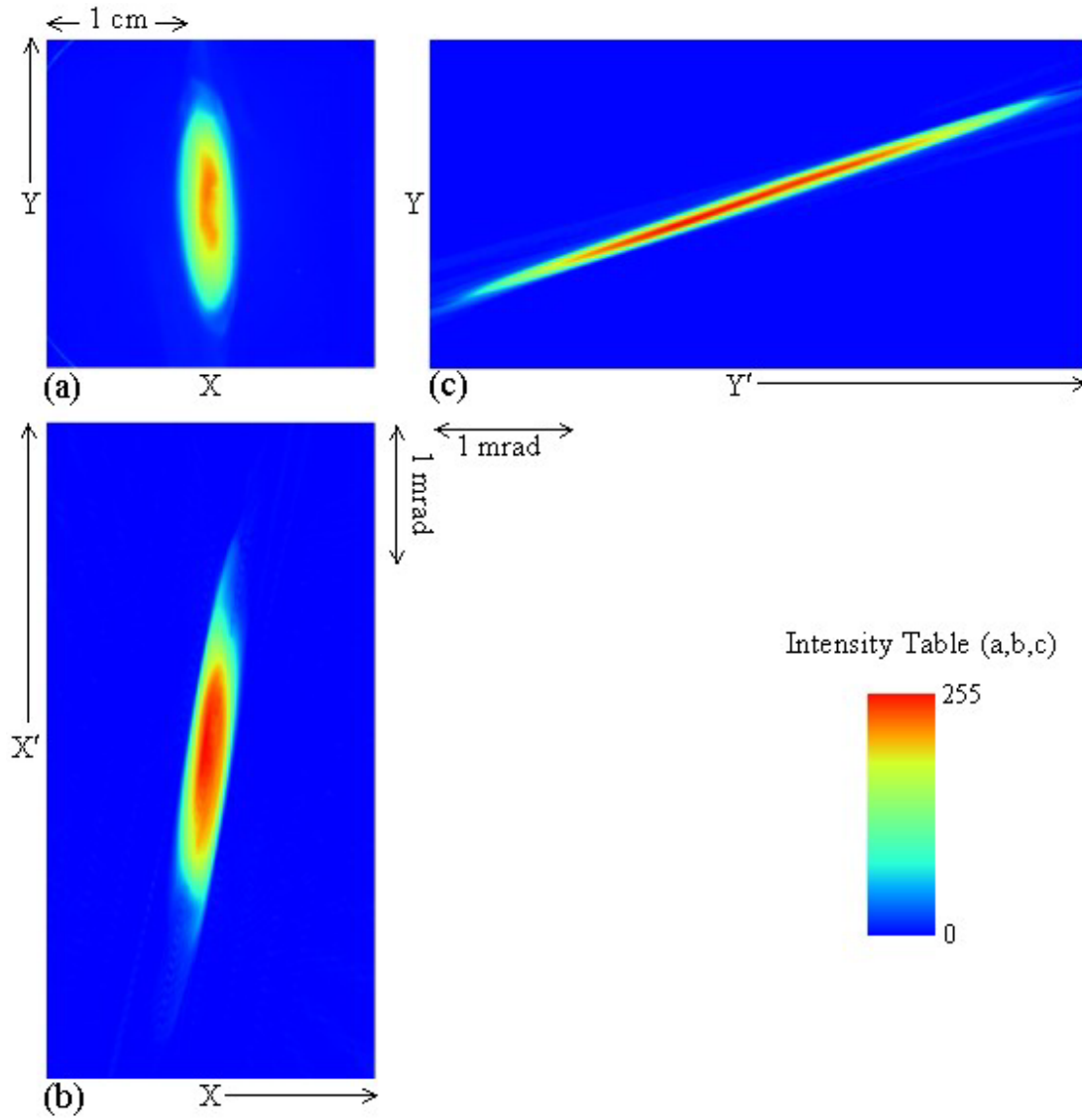
Figure 6.9: Phase space tomography for the 7 mA beam in the ring chamber RC6: (a) spatial (*x*, *y*) beam pictures; (b) (*x*, *x'*) phase space distribution; (c) (*y*, *y'*) phase space distribution.

# Chapter 7 Summary and Conclusion

We reported in this dissertation a number of beam control techniques developed for the intense beam transport experiments in UMER.

The design of UMER demands rigorous control of beam characteristics over long distances. For example, the beam centroid error, beam rotation, and beam mismatch are required within 0.5 mm, 10 deg., and 0.5 mm, respectively. After realizing the beam steering, skew correction, and matching, we are able to achieve the uncertainty in dipole currents corresponding to beam position changes on the screen of only 0.1 mm, and reduce the beam rotation to 4 deg. and mismatch to 0.3 mm, approximately, for a 24 mA beam ($\chi = 0.90$).

In Chap. 2, we presented a technique for optimal beam steering. The optimization criterion consists in finding the right deflection angles for two magnet steerers so as to steer beams through the axes of two quadrupoles, which defines the ideal orbit for the beam transport. The algorithm only depends on the relative beam position motions on the detector (phosphor screen/BPM), thus avoiding the calibration of the detector's centers with respect to adjacent quadrupoles. The steering procedure can be summarized in two steps: (1) determine the dipole current relation between the two steerers corresponding to beams going through the center of the first quadrupole, which can be done by scanning the first quadrupole and observing the relative beam position change on the detector; (2) scan the second quadrupole to determine optimal dipole currents for the two steerers. Mathematically, the steering process only involves two linear regressions, and is therefore very reliable and

suitable for computer automation. For the single-turn beam transport experiment in UMER, we have successfully employed this steering algorithm to find the optimal setting for each ring dipole, which reflects a local optimum based on the local Earth's field and other mechanical inaccuracies. This will establish a baseline for multi-turn operation. In the future, the global optimization of the multi-turn steering must lie in the vicinity of the dipole setting found here.

In Chap. 3, we reported the development of a new quadrupole rotation (skew) corrector. The skew corrector is implemented using a regular PC magnet and mounted over the main PC quadrupole with a 45$^{\mathrm{o}}$ rotation. By powering the main and skew quads with different current supplies, we can independently adjust the normal and skew quadrupole components, so that the quadrupole field is rotated electronically. By using the rotating coil magnetometer, we have characterized the field quality of the new (*main + skew*) quadrupole assembly. Not only does the measured quadrupole field rotation agree very well with the prediction, but also the measured higher order harmonics (sextupole, octupole, decapole, duodecapole) are very small. This result demonstrates that the new skew quadrupole can be used in practice. In order to gain a better understanding of the effects of rotated quadrupoles in UMER, we designed a controlled experiment using the skew quad fitted with the first main quadrupole in the injector line. By varying the skew quad current, we measured skewed beam cross-section densities downstream using a movable fluorescent screen along the beam-line. For comparison, we simulated beam evolution using the WARP PIC code under the same skew condition. Both measurements and simulations show good agreement regarding beam rotations and shapes. To

demonstrate the application of the new design, we developed a general correction scheme to correct severe beam rotations in the UMER ring lattice. For the transport of the 24 mA beam, we see a significant improvement by using only one skew corrector, i.e., the standard deviation of the rotation angles is reduced from $16.2^{\circ}$ to $3.8^{\circ}$ after the correction. A future improvement can be realized by adding a second corrector, which may finally eliminate the residual beam rotations.

In Chap. 4, we presented beam matching studies for space-charge-dominated beams in the UMER facility. We employed both simple rms envelope codes and complex PIC simulations to facilitate the beam optics design. For the ring lattice design, a dipole model with field index 0.72 has been developed to include focusing from the bending dipoles in the envelope codes. The field index is obtained from a dipole field calculation by a new magnetic field solver, MAGLI. The accuracy of this model has been demonstrated by comparing it to the PIC simulations including realistic three-dimensional magnetic fields and bends. In designing the matching section, we intend to inject the beam into the ring with the desired beam radii and slopes (four constraints) as dictated by the results from the ring lattice design. Since the UMER injector has seven adjustable parameters, there are an infinite number of matching solutions. With the use of envelope codes, we found a large number of solutions in a discrete space using a brute-force method. We further chose the optimal one among these solutions according to some specific criteria, e.g., minimizing the largest envelope excursion. Next, we reported an experimental study on empirical beam matching. It is motivated by the fact that the implementation of the calculated magnet strengths in a real experiment normally does not yield true matching

conditions. We developed a systematic method for on-line adjustment of quadrupole strength in the matching section. For the 24 mA beam, the standard deviations of mismatched *X, Y* beam dimensions before the empirical matching are 0.45 mm, 0.43 mm, respectively. After empirical matching is implemented, the deviations are reduced to 0.28 mm and 0.21 mm for *X, Y*, respectively. A possible improvement for further reducing these residual errors can be accomplished by another successive iteration using the same method. Future work should involve a similar procedure for matching the 100 mA beam. The results we obtained in the matching section design will set up a baseline for that work. Even more interestingly, we can develop a similar program for empirical halo reduction. In order to more accurately determine the number of halo particles, a high-resolution camera is necessary.

In Chap. 5, we proposed a new injection scheme for multi-turn operation in UMER. Instead of using two pulsed and physically overlapping quadrupoles, the new scheme requires only one large DC quadrupole centered symmetrically on the bisector of the injector legs and the ring, which serves as both the focusing magnet and the bending magnet for the injected as well as the circulated beams. This new scheme reduces the mechanical and electrical complexities of the original design, but also makes the beam optics more complicated. In order to verify that this is a viable scheme for multi-turn operation, we first studied single particle motion by matrix analysis. It yields the required deflection angles for all the involved dipole magnets. The analytical results agree very well with the WARP-PIC simulation. The WARP simulation also shows that the optics is stable when there are injection errors. After understanding the beam centroid motion, we simulated beam matching for multi-turn

operation. Since the large DC quadrupole has longer fringe fields and induces asymmetric (*x, y*) focusing when particles are injected with an angle, the periodic FODO structure is altered around the injection region. Despite these drawbacks, we can still work on a solution for rms envelope matching. The solution for the 24 mA beam exhibits a slight mismatch (~0.5mm) that does not grow for the following turns. It is an acceptable result considering the effects stated above. From an experimental point of view, though, the true matching condition must be achieved with on-line adjustment of magnet strengths as stated in chapter 4. Another key issue for the future experiments (after closing the ring) is beam steering. The matrix analysis will be a guideline for initial dipole setting. Refinements should be possible by using the optimal steering method we presented in chapter 2.

In Chap. 6, we reported the implementation of phase space tomography for UMER beams. We first used the pencil beam (0.6 mA) as a test beam for benchmarking tomography in UMER. By scanning three quadrupoles, we have achieved full $\pi$ phase space rotation. We performed the tomography experiments at the ring chamber RC1 and RC6, and found the following results worth noting: (1) The reconstructed phase space images exhibit very high picture qualities; (2) The calculated 4×rms emittances (5.4 μm in RC1, 5.8 μm in RC6) from the reconstructed distributions are close to predicted values; (3) The reconstructed phase space distributions are consistent with the directly measured spatial density distributions, in other words, the *X, Y* rms beam sizes calculated from both distributions agree very well; (4) A hollow velocity distribution can be seen from the reconstructed phase space in RC1. This result also agrees with the earlier studies about the effects from

the cathode grid. After testing the pencil beam, we also employed this technique for the 7 mA beam, which has a much higher intensity ($\chi \approx 0.78$). For an accurate reconstruction, we estimated linear space-charge force from the beam envelopes, and included the linear space-charge force in the reconstructions. The results show slight asymmetry between the $x$, $y$ emittances and a small emittance growth from chamber RC1 to RC6, which is reasonable considering the effects from the bending dipoles. For a future study, it should be possible to combine both the tomographic imaging and the self-consistent PIC code including the *nonlinear* space-charge forces.

We have demonstrated several new beam control techniques developed for UMER facilities. Most of the methods are very general and can be easily applied to other machines. Combining various control techniques will be particularly interesting and challenging. For example, the combination of both skew quadrupole and tomography may bring up a breakthrough in four-dimensional $(x, x', y, y')$ phase space reconstruction.

# Bibliography

[1] P.G. O'Shea et al., "The University Maryland Electron Ring (UMER)", Nucl. Instrum. Methods Phys. Res. A 464, 646-652 (2001).

[2] P.G. O'Shea et al., "Experiments with Space Charge Dominated Beams for Heavy Ion Fusion Applications", Laser and Particle Beams 20, 559-602 (2002).

[3] R.O. Rangerter, "The induction approach to heavy-ion inertial fusion: accelerator and target considerations", Nuovo Cimento A106, 1445-1456 (1993).

[4] J. Wei, Y.Y. Lee, D. Raparia, J. Sandberg, J. Tuozzolo, and W.T. Weng, "Spallation Neutron Source Ring - Status, Challenges, Issues, and Perspectives", Proc. IEEE 2003 PAC Conf., Portland, OR, p. 571 (2003).

[5] P.G. O'Shea and H.P. Freund, "Free-Electron Lasers: Status and Applications", Science, 292, 1853 (2001).

[6] F.J. Sacherer, "RMS Envelope Equations with Space Charge", IEEE Trans. Nucl. Sci. NS-18, 1105 (1971).

[7] I.M. Kapchinsky, "Theory of Resonance Linear Accelerators", Harford Academic Press, New York (1985).

[8] M. Reiser, "Theory and Design of Charged Particle Beams", John Wiley & Sons, Inc., Chap. 4 (1994).

[9] M. Reiser, "Theory and Design of Charged Particle Beams", John Wiley & Sons, Inc., p. 195 (1994).

[10] M. Reiser et al. "The Maryland Electron Ring for Investigating Space-Charge Dominated Beams in a Circular FODO System", Proc. IEEE 1999 PAC Conf., New York City, NY, p. 234 (1999).

[11] M. Reiser, "Theory and Design of Charged Particle Beams", John Wiley & Sons, Inc., p. 215 (1994).

[12] S. Bernal et al. "Intense Beam Transport Experiments in a Multi-Bend System at the University of Maryland Electron Ring (UMER)", Nucl. Instrum. Methods Phys. Res. A 519, 380-387 (2004).

[13] R.A. Kishek, S. Bernal, I. Haber, H. Li, P.G. O'Shea, B. Quinn, M. Reiser, and M. Walter, "Beam Halo from Quadrupole Rotation Errors", 29th ICFA

Advanced Beam Dynamics Workshop on Beam Halo Dynamics, Diagnostics, and Collimation, Montauk, New York, AIP Press 693, p. 89 (2003).

[14] H. Li, S. Bernal, R.A. Kishek, T. Godlove, P.G. O'Shea, and M. Reiser, "Printed-Circuit Magnets for the University of Maryland Election Ring (UMER)-New Developments", Proc. IEEE 2001 PAC Conf., Chicago, IL, IEEE Cat. No. 01CH37268, 1802 (2001).

[15] W.W. Zhang, S. Bernal, H. Li, T. Godlove, R.A. Kishek, P.G. O'Shea, M. Reiser, V. Yun, and M. Venturini, "Design and Field measurement of Printed-Circuit Quadrupoles and Dipoles", Phys. Rev. ST. Accel. Beams 3, 122401 (2000).

[16] H. Li, Master thesis, "Printed-Circuit Magnets System for University of Maryland Electron Ring", Univ. of Maryland, College Park (2001).

[17] R.T. Avery, G.R. Lambertson, C.D. and Pike, Proc. IEEE 1971 PAC Conf., Chicago, IL, p. 885 (1971).

[18] M. Venturini, Ph.D. dissertation, Univ. of Maryland, College Park (1998).

[19] Rawson-Lush Instrument Co. Inc., Acton, MA.

[20] R. Shafer, "Beam Position Monitoring", Proc. AIP Conf., 249, vol. 1 (1992).

[21] B. Quinn et al., "Design and Calibration of a Fast Beam Position Monitor", Proc. IEEE 2003 PAC Conf., Portland, OR, IEEE Cat. No. 03CH37423C, 2571 (2003).

[22] H. Li, "UMER Beam Control System SDK", Technical Note UMER-UmerCtrlSDKV1.0, IREAP, Univ. of Maryland, unpublished (2004).

[23] P. Tenenbaum and T.O. Raubenheimer, "Resolution and systematic limitation in beam-based alignment", Phys. Rev. ST. Accel. Beams 3, 052801 (2000).

[24] M. Walter et al., "Alignment of Components at the University of Maryland Electron Ring", Proc. IEEE 2003 PAC Conf., Portland, OR, IEEE Cat. No. 03CH37423C, 2577 (2003).

[25] E.D. Courant and H.D. Snyder, Ann. Phys. 3, 1 (1958).

[26] M. Reiser, "Theory and Design of Charged Particle Beams", John Wiley & Sons, Inc., p. 152 (1994).

[27] John J. Barnard, "Emittance Growth from Rotated Quadrupoles in Heavy Ion Accelerators", Proc. IEEE 1995 PAC Conf. Dallas, TX, p. 3241, (1996).

[28] J. J. Barnard and Bojan Losic, "Envelope Modes of Beams with Angular Momentum", International Linac Conf., Monterey, CA (2000).

[29] R. A. Kishek, J. J. Barnard, and D. P. Grote, "Effects of Quadrupole Rotations on the Transport of Space-Charge-Dominated Beams: Theory and Simulations comparing Linacs with Circular Machines", Proc. IEEE 1999 PAC Conf., New York City, NY, p. 1761 (1999).

[30] W.G. Davis, Nucl. Instrum. Methods Phys. Res. A 311, 399 (1992).

[31] D.P. Grote, A. Friedman, I. Haber, and S. Yu, "Three-dimensional simulations of high current beams in induction accelerators with WARP3D", Fus. Eng. & Des. 32-33, 193-200 (1996).

[32] M. Reiser, "Theory and Design of Charged Particle Beams", John Wiley & Sons, Inc., p. 470 (1994).

[33] A. Cucchetti, M. Reiser, and T.P. Wangler, "Studies of Emittance Growth in RMS Mismatched Beams", Proc. IEEE 1991 PAC Conf., San Francisco, CA, p. 251 (1991).

[34] M. Reiser, "Theory and Design of Charged Particle Beams", John Wiley & Sons, Inc., p. 240 (1994).

[35] T.P. Wangler, K.R. Crandall, R. Ryne, and T.S. Wang, "Particle-core model for transverse dynamics of beam halo", Phys. Rev. ST. Accel. Beams. 1, 084201 (1998).

[36] M. Reiser, "Theory and Design of Charged Particle Beams", John Wiley & Sons, Inc., p. 154, (1994).

[37] H. Li, MAGLI Manual for Windows and Linux, unpublished (2002).

[38] E. Asseo, CERN PS/85-3, LEA (1985).

[39] H. Li, S. Bernal, R.A. Kishek, I. Haber, Y. Zou, P.G. O'Shea, and M. Reiser, "Simulation studies on matching of space-charge-dominated beams for the University of Maryland Electron Ring (UMER)", Nucl. Instrum. Methods Phys. Res. A 519, 405-411 (2004).

[40] M. Reiser, "Theory and Design of Charged Particle Beams", John Wiley & Sons, Inc., p. 118 (1994).

[41] C.K. Allen, S. K. Guharay, and M. Reiser, "Optimal Transport of Low Energy Particle Beams", Proc. IEEE 1995 PAC Conf., Dallas, TX, p. 2324 (1996).

[42] The Mathworks, Inc.

[43] Y. Li, T. Godlove, R. Kishek, M. Venturini, P. Chin, Y. Zou, J.G. Wang, and M. Reiser, "Design, simulation and test of Panofsky quadrupoles", Proc IEEE 1999 PAC Conf., New York City, NY, p. 3369 (1999).

[44] H. Li, R.A. Kishek, S. Bernal, T. Godlove, M. Walter, P.G. O'Shea, and M. Reiser, "Beam optics design on a new injection scheme for the University of Maryland Electron Ring (UMER)", Proc. IEEE 2003 PAC Conf., Portland, OR, IEEE Cat. No. 03CH37423C, 1676 (2003).

[45] M. Walter et al., "Electro-mechanical Design for Injection in the University of Maryland Electron Ring", Proc. IEEE 2003 PAC Conf., Portland, OR, IEEE Cat. No. 03CH37423C, 1673 (2003).

[46] M. Reiser, "Theory and Design of Charged Particle Beams", John Wiley & Sons, Inc., Chap. 6 (1994).

[47] W.R. Hendee, "Physics and Applications of Medical Imaging", Rev. Mod. Phys., Vol. 71, No. 2, Centenary (1999).

[48] McKee, PhD dissertation, "Creation, Transport and Measurement of Bright Relativistic Electron Beams", Duke University (1994).

[49] McKee, P.G. O'Shea, and J.M.J. Madey, Nucl. Instrum. Methods Phys. Res. A 358, 264 (1995).

[50] M.G. Minty and F. Zimmermann, "Beam Techniques – Beam Control and Manipulation", Sec. 3.2, US Particle Accelerator School, Univ. of Chicago and Argonne National Lab (1999).

[51] S. Bernal, and H. Li, "Summery of pepper pot measurements", UMER Technical Note UMER-052802-SBHL, IREAP, Univ. of Maryland, unpublished (2002).

[52] Y. Zou, H. Li, M. Reiser, and P.G. O'Shea, "Theoretical Study of Transverse Emittance Growth in a Gridded Electron Gun", Nucl. Instrum. Methods Phys. Res. A 519, 432-441 (2004).

[53] J. Radon, "On the determination of functions from their integral values along certain manifolds", Math. Phys. Klasse, 69, 262-277 (1917).

[54] R. Gordon and G.T. Herman, "Three Dimensional Reconstruction from Projections: a Review of Algorithms", Int. Rev. Cytol. 38, p. 111 (1974).

[55] M. Reiser, "Theory and Design of Charged Particle Beams", John Wiley & Sons, Inc., p. 62 (1994).

[56] R.A. Kishek, S. Bernal, C.L. Bohn, D. Grote, I. Haber, H. Li, P.G. O'Shea, M. Reiser, and M. Walter, "Simulations and experiments with space-charge-dominated beams", Physics of Plasmas 10 (5), 2016 (2003).

[57] I. Haber, S. Bernal, C. M. Celata, A. Friedman, D. P. Grote, R.A. Kishek, B. Quinn, P.G. O'Shea, M. Reiser, and J.L. Vay, "Collective Space-Charge Phenomena in the Source Region", Nucl. Instrum. Methods Phys. Res. A 519, 396-404 (2004).

[58] M. Venturini, R.A. Kishek, and M. Reiser, "Dispersion and space-charge", Proceedings of Workshop on Space-Charge Physics in High Intensity Hadron Ring at Shelter Island, New York, AIP Press, no. 448, p. 278 (1998).